Université de Montréal

Electrochemical synthesis of organic compounds using CO_2 and biomass as feedstock

Par

Junnan Li

Département de chimie, Faculté des arts et des sciences

Thèse présentée à la Faculté des études supérieures et postdoctorales en vue de l'obtention du grade de Philosophiae Doctor (Ph. D)

Mai, 2023

Université de Montréal

Département de chimie, Faculté des arts et des sciences

Cette thèse intitulée

Electrochemical synthesis of organic compounds using CO_2 and biomass as feedstock

Présente par

Junnan Li

A été évaluée par un jury composé des personnes suivantes

Dominic Rochefort
Président-rapporteur

Nikolay Kornienko
Directeur de recherche

Frank Hein Schaper
Membre du jury

Ana C. Tavares (INRS EMT**)**
Examinateur externe

Résumé

Le CO_2 et la biomasse sont abondants dans la nature. La conversion de ces deux éléments constitutifs en carburants ou en produits chimiques à valeur ajoutée par des méthodes électrochimiques est essentielle pour atténuer la crise énergétique et réduire la pollution de l'environnement, ainsi que pour atteindre la carbone neutralité. Au cours des dernières décennies, de nombreux efforts ont été consacrés à ce domaine, mais la plupart d'entre eux se concentrent sur la conception de catalyseurs et l'amélioration des performances, et seules quelques recherches se concentrent sur de nouvelles réactions ou sur le mécanisme de ces réactions. Ici, nous développons une série de nouvelles réactions et étudions les mécanismes de ces réactions en utilisant la spectroscopie in situ, les principaux résultats sont les suivants :

1) Les réactions de réduction du furfural ont été menées en utilisant une feuille de Cu électrochimique comme catalyseur, et l'alcool furfural (FA, efficacité faradique, FE : 43,0%) et le 2-méthylfurane (MF, FE : 57,5%) ont été obtenus après électrolyse sous -0,43V (par rapport à l'électrode à hydrogène réversible, RHE). Les effets des différentes facettes du catalyseur sur la sélectivité ont été étudiés, et le Cu (110) produit préférentiellement de l'AF, tandis que les défauts sont les sites actifs pour la formation de MF. La spectroscopie Raman operando a montré que la production de FA et de MF partage le même intermédiaire à l'étape initiale, avec différents sites actifs conduisant aux différentes voies entre les étapes intermédiaires et suivantes et générant différents produits.

2) Des produits de liaison C-N (acétamide et formamide) ont été obtenus par la réaction de réduction du CO_2 (CO_2RR) avec la combinaison du substrat NH_3 et des électrocatalyseurs commerciaux à base de nanoparticules de Cu ou de CuO. Avec l'optimisation, la FE maximale de ces deux produits est de ~10% au total, et la meilleure condition de réaction est 50mg Cu NPs, 1M KOH, avec 0.3M NH_3, à -0.78V (vs. RHE) pendant 30 mins. L'IR in situ a montré que la formation de formamide et de formate partage le même intermédiaire, et que la production d'acétamide et d'acétate subit une voie de réaction similaire.

3) L'hydroxyméthanesulfonate (HMS), le sulfoacétate (SA) et le méthanesulfonate (produits de liaison C-S, FE représente 6% au total) ont été obtenus par le couplage CO_2RR avec l'ajout de sulfite (SO_3^{2-}), et des NPs de Cu_2O synthétisées par la méthode de chimie humide ont été utilisées comme électrocatalyseurs. Parmi ces trois composés à liaison C-S, le HMS est le principal produit, la FE pouvant atteindre un maximum de 6 %. Le XRD in situ a montré que Cu^0 est l'espèce active pour le processus de couplage C-S. Les calculs operando Raman et DFT ont montré que *CHOH est l'intermédiaire clé dans la formation de la liaison C-S, et que le couplage entre *CHOH et SO_3^{2-} est l'étape qui détermine le taux.

Mots-clés : Réduction du furfural, réaction de réduction du CO_2, spectroscopie operando Raman, spectroscopieinfrarouge in situ, mécanisme.

Abstract

CO_2 and biomass are abundant in nature. Conversion of these two building blocks into fuels or value-added chemicals by electrochemical methods is essential for alleviating the energy crisis and reducing environmental pollution, and achieving carbon neutrality. In the past few decades, much effort has been devoted to this field, but most of this focuses on the design of catalysts and improvement of the performances, and only few research thrusts focus on new reactions or the mechanism of these reactions. Herein, we develop a series of new reactions and investigate the mechanisms of these reactions by using in-situ spectroscopy, the main results are shown as follows:

1) Furfural reduction reactions were conducted by using an electrochemical roughed Cu foil as the catalyst, and furfural alcohol (FA, Faradaic efficiency, FE: 43.0%) and 2-methylfuran (MF, FE: 57.5%) were obtained after electrolysis under -0.43V (vs. reversible hydrogen electrode, RHE). The effects of different facets on the selectivity were investigated, and Cu (110) is preferential to produce FA, while defects are the active sites for the formation of MF. Operando Raman spectrum showed that the production of FA and MF share the same intermediate at the initial stage, with different active sites leading to the pathway differential on the intermediate of the following steps and generating different products.

2) C-N bond products (acetamide and formamide) were obtained by CO_2 reduction reaction (CO_2RR) with the combination of NH_3 reactants and commercial Cu or CuO nanoparticle (NPs) electrocatalysts. The maximum FE of these two products is ~ 10% in total. With optimization, we found a higher pH, thicker catalyst layer, and larger size of cations are beneficial to the production of acetamide. This can be attributed to the higher production of C_2 intermediate and further leads to a higher FE of acetamide. In-situ IR showed that the formation of formamide and formate share the same intermediate, and the production of acetamide and acetate undergoes a similar reaction pathway. The mechanism can help to design the new next generation catalyst with a higher efficiency, which is beneficial to the future application of this reaction in chemical industry. Nitrate and nitrite are used instead of ammonia as nitrogen sources to produce C-N bond

compounds, which suggests that this reaction provides a new possibility for organic synthesis. In all, this reaction expands the scope of the CO_2RR application, and is also good for the development of organic synthesis.

3) Hydroxymethanesulfonate (HMS), sulfoacetate (SA) and methanesulfonate (C-S bond products, FE is 6% in total) were obtained by coupling CO_2RR with the addition of sulfite (SO_3^{2-}), and Cu_2O NPs which synthesized by the wet chemistry method were used as electrocatalysts. Among these three C-S bond compounds, HMS is the main product, FE can reach 6% maximum. In-situ XRD showed that Cu^0 is the active species for C-S coupling process. Operando Raman and DFT calculation further showed that *CHOH is the key intermediate in the C-S bond formation, and the coupling between *CHOH and SO_3^{2-} is the rate-determining step. The discovery of reaction intermediates opens up the possibility of designing highly efficient catalysts, which can promote the application of this reaction in real industries. Also, this reaction provides a new possibility to synthesize C-S bond products, which have the potential to partially replace traditional organic synthetic routes with greener and more sustainable procedures.

Keywords: Furfural reduction, CO_2 reduction reaction, Operando Raman, in-situ infrared spectroscopy, mechanism.

Table des matières

Liste des tableaux

Liste des figures

Liste des sigles et abréviations

AEM : Anion-exchange membrane

ATR: Attenuated total reflection

BPM: Bipolar membrane

C_1: Single carbon products

C_{2+}: Multicarbon products

CDC: Cross-dehydrogenative coupling

CE: Counter electrode

CEM: Cation-exchange membrane

CODHs: Carbon monoxide dehydrogenases

CO_2RR: CO_2 reduction reaction

DFT: Density-functional theory

DMF: Dimethylformamide

DMSO: Dimethyl sulfoxide

ECH: Electrochemical hydrogenation and hydrolysis

ECSA: Electrochemically active surface area

[EMEM]BF_6: 1-ethyl-3-methylimidazolium tetrafluoroborate

ESR: Electron spin resonance

EXAFS: Extended X-ray absorption fine structure

FA: Furfural alcohol

FE: Faradaic efficiency

FF: Furfural

GC: Gas chromatography

GDE: Gas diffusion electrode

HER: Hydrogen evolution reaction

HMS: Hydroxymethanesulfonate

IR: infrared

MF: 2-methylfuran

MPL: Microporous layer

MPS: Microporous substrate

MS: Mass spectrometry

NMR: Nuclear magnetic resonance

NPs: Nanoparticles

OD-Cu: Oxide-derived Cu

OER: Oxygen evolution reaction

PCET: Proton coupled electron transfer

PPh_2bipy: 6-diphenylphosphineo-2, 20-bipyridyl

PTFE: Polytetrafluoroethylene

RDS: Rate-determining step

RE: Reference electrode

RHE : Reversible hydrogen electrode

SA : Sulfoacetate

SECCM: Scanning electrochemical microscopy

STM: Scanning tunnelling microscopy

TEM: Transmission electron microscopy

THF: Tetrahydrofuran

TOF: Turn-over frequency

WE: Working electrode

XAFS: X-ray absorption fine structure

XANES: X-ray absorption near-edge structure

XAS: X-ray Absorption spectroscopy

XPS: X-ray Photoelectron spectroscopy

XRD : X-ray Diffraction

Remerciements

I am honored to have spent the best four years of my life at Université de Montréal. Here, I would like to thank my advisor, colleagues, family members and friends for the company, because of your support, I can persist in completing my studies.

First of all, I would like to express my gratitude to my advisor, Professor Dr. Nikolay Kornienko, thank you for giving me the opportunity to join your group, and I'm very appreciative to become your student. In 2019, I came here with a dream of scientific research, but in the past four years, when I encountered difficulties, I often doubted whether I was suitable for scientific research. Thank you for your continuous support, for solving problems with me, for leading me to write reviews and publish articles, and thank you for your help in my present and future scientific research. He has excellent scientific research ability, rich professional knowledge, high professional quality, excellent coordination ability, good at cooperation, and can perfectly handle various projects. He is the best supervisor I have met before. His excellent ability infected me, and I will work hard, hoping to become as good as him. I apologize for the trouble I have caused you over the past four years. Now I am proud to be your student and hope that one day you will be proud of me.

Thanks to the following funding agencies, Natural Sciences and Engineering Research Council of Canada (NSERC), Études supérieures et postdoctorales (ESP), Mitacs, and Département de Chimie, Charron-Lam and Marguerite-Jacques-Lemay family. Thanks to the financial support from these agencies, which makes me concentrate on scientific research without spending time on my livelihood.

Thanks for the help from my lab members Morgan McKee, Hossein Bemana, Alexandre Terry, Dr. Kiran Kuruvinashetti and Yuxuan Zhang, and all the professors and colleagues from inorganic groups, Prof. Dr. Christian Reber, Frank Hein Schaper, Dominic Rochefort, Garry S. Hanan, Davit Zargarian, and my colleagues Loic Mangin, Olivier Schott, Rajib Kumar Sarker, and Matteo Cardoso, and my friend Xiaozheng Wei from the organic group, thanks for helping me when I encountered experimental difficulties.

Thanks for the help from NMR lab and X-ray diffraction lab, Dr. Pedro M. Aguiar, Cédric Malveau, and Daniel Chartrand. Thanks for helping me to test samples and analyze the data.

Thanks my friend Dr. Xian Yue, Yi Liu, Yue Hu, Xuwen Da and Chang Chen, thanks for listening to my complaints and enlightening me.

Thanks to my parents for always supporting me, and at last, thanks to my grandparents for companying in my childhood. It's a pity that due to COVID-19, I couldn't go back to China to see you the last time, but I believe you would be proud to know I'll obtain my Ph.D. diploma. I'll always love you and you will always be alive in my heart.

Junnan Li

2023, In Montreal

Chapitre 1 – Introduction

1.1 Background

Since the 19th century industrial revolution, the demand for energy has increased to meet the development of society[1]. Currently, 85% of primary energy sources rely on fossil fuels (34% petroleum, 27% coal, and 24% natural gas)[2,3]. However, fossil fuels are not sustainable, and the consumption rate is much higher than the formation speed, which will lead to energy crisis[2-4]. Moreover, the combustion of fossil fuels also causes environmental problems such as air pollution, or greenhouse effect, which threaten the existence live on earth[2,5]. Thus, developing the next generation of sustainable and clean energy to substitute fossil sources is urgent[6]. In the past few decades, several renewable energy sources have been investigated and applied in industrial production and life, for example, solar, wind, geothermal, ocean, and nuclear energy, even though their percentage in total energy consumption is still low (<5%)[2,4]. In addition, these energy sources have some limitations: most of them are geographical, seasonal, and intermittent, and thus for future applications, they should be converted or stored in another form[2]. Electricity, when generated from renewable sources, may be environmentally friendly but must be stored if not immediately used. In addition to storage in the form of batteries, electricity can be also used for synthesizing clean fuels such as ethanol, ethylene, or biofuels, which are capable of storing energy in chemical bonds[5,7].

Electrochemical biomass reduction is a promising method that can be used to store electrical energy in biofuels (Figure 1.1). Biomass feedstocks involve edible biomass (e.g., sugar, grains, seeds) nonedible biomass, (lignocellulose, e.g., cereal straw, sugar cane bagasse, and organic waste), and microorganisms (e.g., algae), that are abundant in nature[2,8]. Among these biomass building blocks, lignocellulose is more attractive because it can be recycled from agricultural waste, a system which may reduce environmental pollution and avoid using food to produce fuels[2]. For example, the acid-catalyzed hydrolysis of agroindustrial waste (e.g., corncob and oat hull) can produce xylose, which can be further dehydrated to fabricate furfural[9], which is a typically platform molecule. Furfural (FF) derivatives such as furfural alcohol (FA) or 2-

methylfuran (MF) can be obtained by electrochemical hydrogenation of furfural, which can be used as clean biofuels, or used as useful chemical substrates in polymer and pharmaceutical industries[10]. Both of these applications can alleviate reliance on fossil fuels because right now the production of chemicals also depends on the separation of fossil fuels. In summary, Biomass reduction can be used to produce valuable chemicals and energy carriers in a green way, it's beneficial to the circular economy model[2].

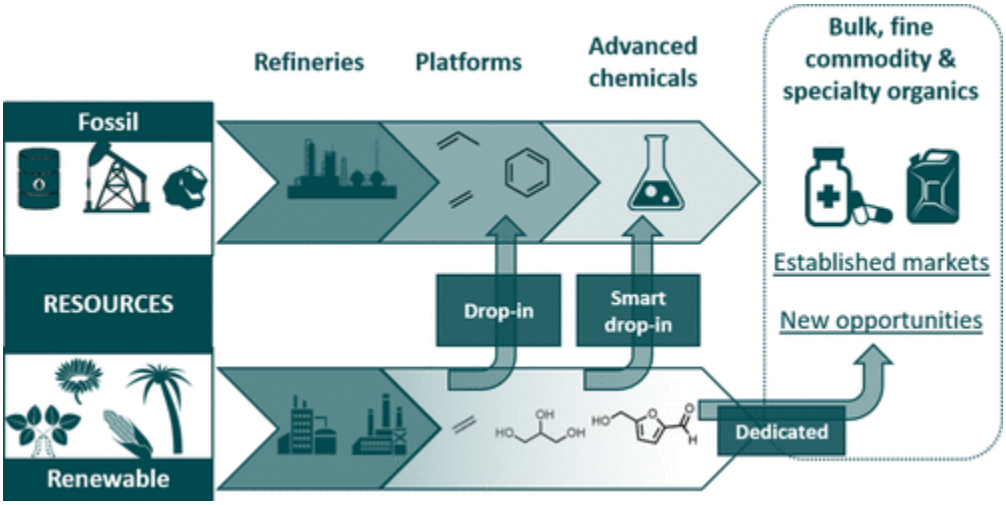

Figure 1.1 - Using biomass as intermedium to store electricity[1]. Reprinted (adapted) with permission from {Chem. Rev. 2020, 120, 15, 7219–7347}. Copyright {2020} American Chemical Society.

In addition to furfural reduction reaction, electrical carbon dioxide (CO_2) reduction reaction (CO_2RR) is another successful strategy for utilizing and storing renewable electricity[5,7] (Figure 1.2). CO_2 is a greenhouse gas that is produced from the combustion of fossil fuels, that causes global warming, ocean acidification, desertification, and some other environmental problems[4,5]. Reducing the excessive CO_2 in the atmosphere is also important for a sustainable economy. In nature, CO_2 can be reduced by the photosynthesis process, and transformed into sugar and provide energy for plants[11]. Electrocatalytic carbon dioxide reduction reaction offers a similar avenue to close the carbon cycle. A variety of products can be obtained by using CO_2 as a C_1-building block, such as CO, ethylene (C_2H_4), synthesis gas (syngas), which can be used clean fuels directly to achieve a zero-carbon energy cycle and as a route to the conversion of electricity[5,6,12].

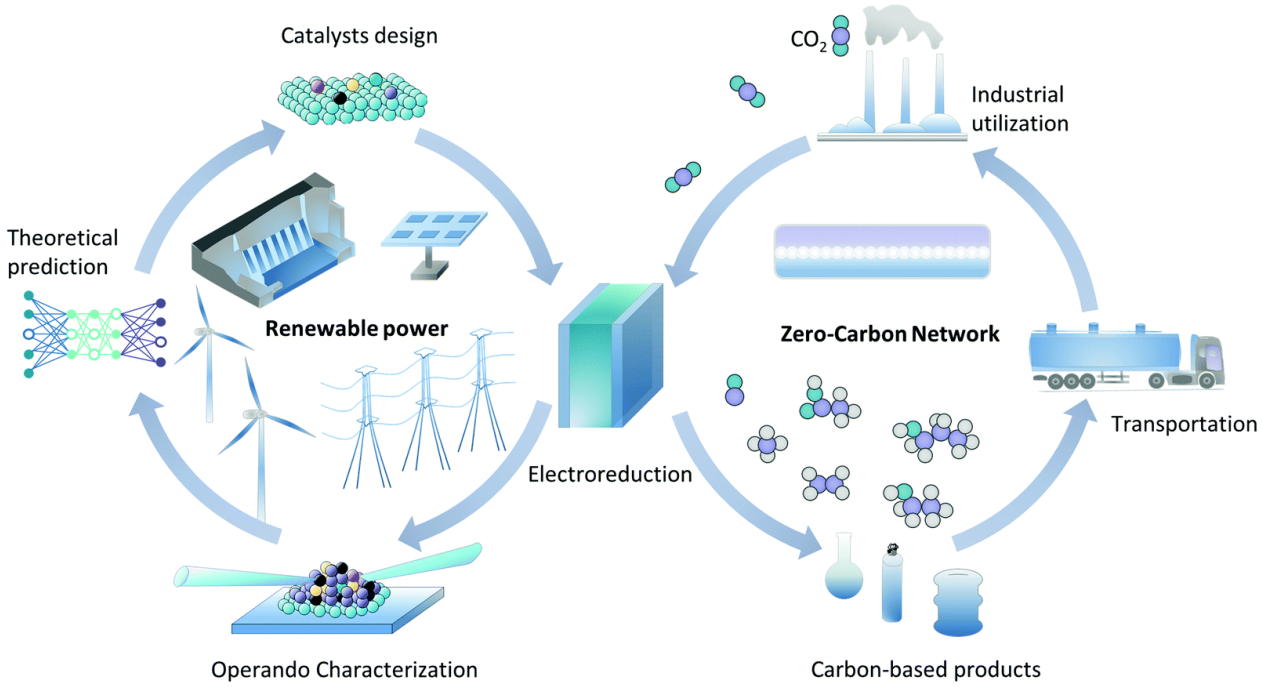

Figure 1.2 – Illustration of CO_2 Reduction reactions[5]. Reproduced from Chem. Soc. Rev., 2022, 51, 1234–1252 with permission from the Royal Society of Chemistry.

1.2 Furfural Reduction

Furfural (FF) is an abundant building block (production 250000 tons/year) that can be produced by acid-catalyzed dehydrogenation of xylose from the hydrolysis of xylan-rich agricultural waste (corncob or oat hull)[8-10]. Valorization of furfural can produce furfural alcohol and 2-methylfuran, which can be used for producing binders or biofuels respectively[1,8]. At present, the hydrogenation and hydrogenolysis of FF undergo thermocatalytic processes, which need a high temperature and pressure, also a supply of hydrogen. Electrochemical methods are promising routes to replace thermocatalysis method because the reaction can be carried out under ambient temperature and pressures. Hydrogen can be produced in-situ from the electrolyte, and no external H_2 is needed, which can reduce energy and cost, as well as avoid the emission of CO_2 from H_2 production by steam reforming. Thus, electrochemical hydrogenation and hydrolysis (ECH) of furfural becomes an attractive research direction. The reaction pathway of FF to FA and 2-MF is shown in Figure 1.3. Different electrocatalysts, pH of the electrolyte, initial concentration of FF, applied potential and reaction times can be chosen to synthesize different end products[8].

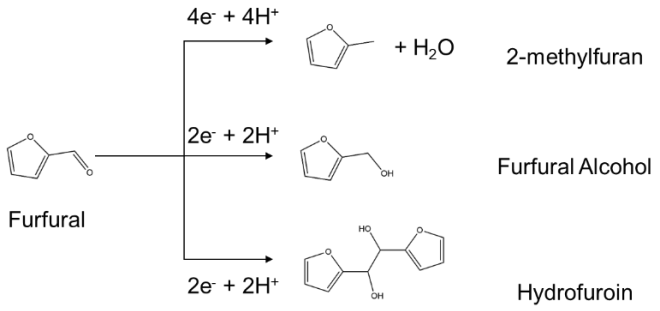

Figure 1.3 – Furfural reduction reaction pathways[8].

1.2.1 Catalysts

A large variety of electrocatalysts have been developed for ECH of FF, including metals (Cu, Ni, Pt, Pd, Rh, Ru, Pb, Fe, Al, Zn, Cd, Hg, Co, and Ti), alloys (stainless steel, Zn amalgam), oxides (TiO_2), phosphides (Cu or Ni-based nanophosphides), and carbon materials (such as graphite)[8]. The main product of Al, Pb, Fe, and C is dimer product, pinacol (electrolyte: 0.5M H_2SO_4 in water/acetonitrile mixture, -10 mA cm^{-2}, Figure 4). For Pt, the prominent product is FA, the production is similar for FA and MF on Ni. Cu is the only metal that shows a primary production of MF. In addition to Pt, Pd, Rh, Ru, and Co are also preferential to produce FA as major products (5% acetic acid in the mixture of 2-propanol and water (1:1))[13]. Further, TiO_2 can be used as ECH catalyst for producing FA, which show a 61.7% conversion efficiency in 1-ethyl-3-methylimidazolium tetrafluoroborate ([EMIM]BF_4)[14]. Besides the intrinsic properties of these materials, the product distribution can also be affected by morphology. For example, compared with Cu foil, Cu NPs show a higher FE of MF, but a lower FE of FA. Cu NPs also have higher stability than Cu foil because they can suppress the formation of furanic polymers. Rational choice and design of the catalyst are beneficial to the enhancement of FF ECH[15].

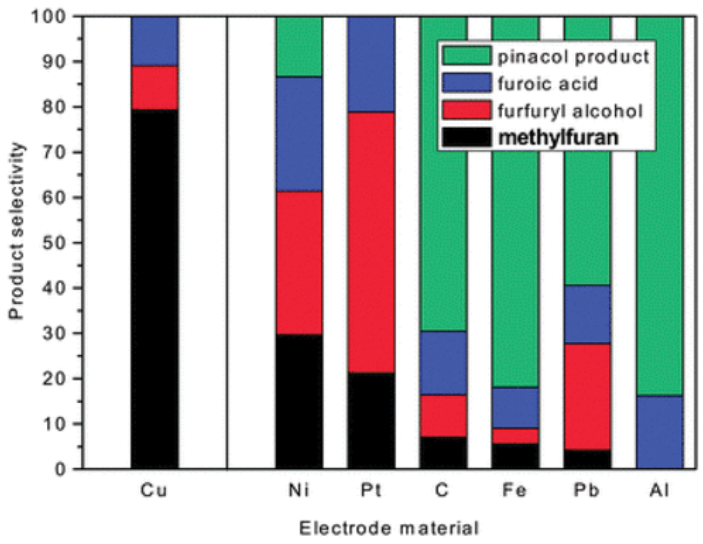

Figure 1.4 – Products distribution of furfural reduction with different catalsyts[13]. Reprinted (adapted) with permission from {ACS Catal. 2020, 10, 5, 3212–3221}. Copyright {2020} American Chemical Society.

1.2.2 pH value

Lopez-Ruiz et al. found that the major product over Cu is FA, which is different from previous works with similar catalysts[16]. This is because of different reaction conditions. When the electrolyte is near neutral, FA will be produced instead of MF. This result shows that choosing a different pH can modify the product distribution of ECH of FF. On Cu electrode, when the pH increases, the production of FA increases linearly, and the selectivity of MF decrease. When the pH is lower than 3.4, the major furanic product is MF. From pH 3.4 to 10, FA is the main product[17]. A similar trend is observed over Ni electrodes[18]. Different electrolytes (using HCl instead of H_2SO_4) were used to confirm the function of pH and exclude the effect of anions[17]. At the region above pH 10, FA is still the main furanic product[19], but the selectivity of furanic product is low because of its low stability in high alkaline conditions[18]. The relationship between pH and the selectivity of different furanic products is shown as Figure 1.5[8].

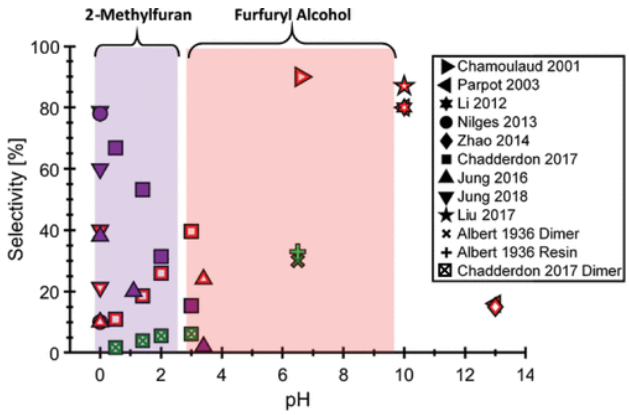

Figure 1.5 – Effect of different pH on the selectivity of FF reduction[8]. Reprinted (adapted) with permission from {ACS Catal. 2020, 10, 5, 3212–3221}. Copyright {2020} American Chemical Society.

1.2.3 Applied potential, initial concentration of FF, and reaction time

The effect of potential, initial concentration of FF, and reaction time on selectivity is shown in Figure 1.6. The recommended applied potential of FF is from -0.5 V to -0.65 V vs. RHE. When the potential becomes more negative, HER side reaction becomes dominant, consuming the electrons and lowering the selectivity of furanic products[20]. Except for the applied potential, controlling the reaction time is also important because MF and FA will degrade (especially in strong acid conditions, pH 0-1) or undergo self-polymerization or self-condensation reactions if the reaction time is too long (over 5 h). The degree of decomposition and polymerization depends on the initial concentration of FF[8].

The best concentration of FF for producing FA and MF is 20 - 200 mM[8]. If the concentration of FF is lower than 20 mM, H_2 is the dominant product. When FF concentration is higher than 200 mM, dimerized hydrofuroin such as resins are the major products, and the selectivity of MF and FA decrease[20]. This phenomenon is observed for different materials and reaction conditions, thus optimizing the initial concentration of FF is key to tuning the product distribution of FF reduction reaction.

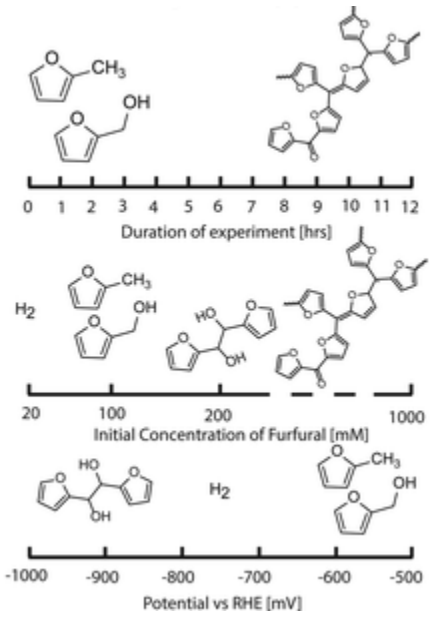

Figure 1.6 – Effects of different reaction time, initial concentration of furfural, and applied potential on the selectivity of FF reduction reaction[8]. Reprinted (adapted) with permission from {ACS Catal. 2020, 10, 5, 3212–3221}. Copyright {2020} American Chemical Society.

1.3 CO_2 Reduction Reaction

In 2018, 195 countries and regions co-signed the Paris Agreement. With this, they reached a consensus to achieve net zero carbon emission in the second half of this century. To accomplish this goal, numerous studies have focused on CO_2 conversion to prevent releasing excessive CO_2 into the atmosphere. Among these different CO_2 fixation methods, electrocatalytic CO_2RR is a viable avenue for closing the carbon cycle[21], which can use CO_2 captured from the atmosphere or industrial waste gas as feedstock, and renewable electricity to provide the driving force to produce fuels or value-added chemicals. In general, the products of CO_2RR are the mixture of carbon species, which include C_1 products such as carbon monoxide (CO), methane (CH_4), formate ($HCOOH^-$), methanol (CH_3OH) and C_{2+} products, ethylene (C_2H_4), ethane (C_2H_6), acetate (CH_3COO^-), ethanol (C_2H_5OH), propanol (C_3H_7OH), and etc[7]. The equations and standard potentials of these reactions are listed in Table 1.1[22].

Table 1.1 - Equations of CO_2RR[22].

Half-electrochemical thermodynamic reactions	Standard reduction potentials (V vs. SHE)
$CO_2(g) + 4\ H^+ + 4\ e^- \rightarrow C(s) + 2\ H_2O\ (l)$	0.210
$CO_2(g) + 2\ H_2O(l) + 4e^- \rightarrow C(s) + 4\ OH^-$	-0.627
$CO_2(g) + 2\ H^+ + 2\ e^- \rightarrow HCOOH(l)$	-0.250
$CO_2(g) + 2\ H_2O(l) + 2\ e^- \rightarrow HCOO^-\ (aq) + OH^-$	-1.078
$CO_2(g) + 2\ H^+ + 2\ e^- \rightarrow CO(g) + H_2O(l)$	-0.106
$CO_2(g) + 2\ H_2O(l) + 2\ e^- \rightarrow CO(g) + 2\ OH^-$	-0.934
$CO_2(g) + 4\ H^+ + 4\ e^- \rightarrow CH_2O(l) + H_2O(l)$	-0.070
$CO_2(g) + 3\ H_2O(l) + 4\ e^- \rightarrow CH_2O(l) + 4\ OH^-$	-0.898
$CO_2(g) + 6\ H^+ + 6\ e^- \rightarrow CH_3OH(l) + H_2O(l)$	0.016
$CO_2(g) + 5\ H_2O(l) + 6\ e^- \rightarrow CH_3OH(l) + 6\ OH^-$	-0.812
$CO_2(g) + 8\ H^+ + 8\ e^- \rightarrow CH_4(g) + 2\ H_2O(l)$	0.169
$CO_2(g) + 6\ H_2O(l) + 8\ e^- \rightarrow CH_4(g) + 8\ OH^-$	-0.659
$2\ CO_2(g) + 2\ H^+ + 2\ e^- \rightarrow H_2C_2O_4(aq)$	-0.500
$2\ CO_2(g) + 2\ e^- \rightarrow C_2O_4^{2-}\ (aq)$	-0.590
$2\ CO_2(g) + 12\ H^+ + 12\ e^- \rightarrow CH_2CH_2(g) + 4\ H_2O(l)$	0.064
$2\ CO_2(g) + 8\ H_2O(l) + 12\ e^- \rightarrow CH_2CH_2(g) + 12\ OH^-$	-0.764
$2\ CO_2(g) + 12\ H^+ + 12\ e^- \rightarrow CH_3CH_2OH(l) + 3\ H_2O(l)$	0.084
$2\ CO_2(g) + 9\ H_2O(l) + 12\ e^- \rightarrow CH_3CH_2OH(l) + 12\ OH^-$	-0.744

A typical CO_2RR system includes a cathode, an anode, an electrolyte, and a membrane (Figure 1.7)[6]. The cathode is the electrocatalyst for CO_2RR, on which different products are generated, and it depends on the properties of the materials. The function of the electrolyte is to transport charged species and to facilitate the migration of CO_2 to the cathode surface. On the anode, an oxidation reaction occurs, such as the oxygen evolution reaction (OER). The cathode and anode are separated by a membrane, which can prevent the CO_2RR products diffusion to the other

compartment, and maintain the charge balance of the two compartments. By changing different electrocatalysts, electrolytes, and applied voltage, the selectivity of CO_2RR can be tuned[6].

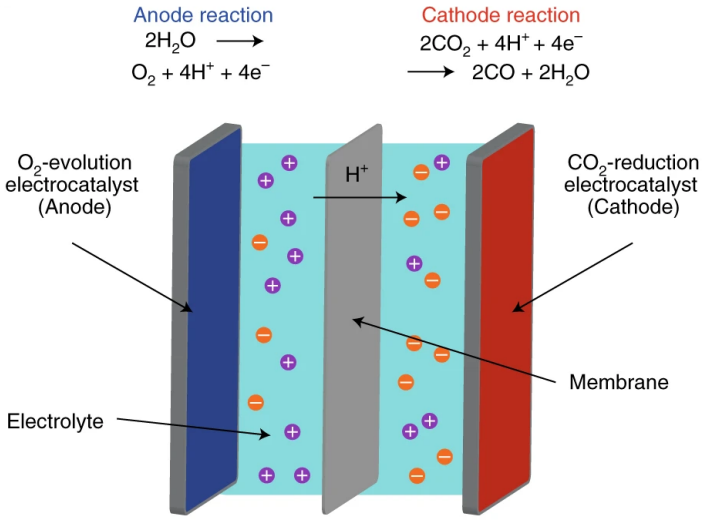

Figure 1.7 – Illustration of CO_2RR reaction system[6]. Reproduced from Nature Catalysis volume 2, pages648–658 (2019) with permission from the Springer Nature.

According to the potentials of these reactions (Table 1), different products can be obtained by changing the applied voltages. But in practice, the existence of overpotential (the difference between the applied potential and equilibrium potential) leads to a requirement of higher energy input than the thermodynamic ideal to drive the CO_2RR. This is because CO_2 molecules are stable, dissociation energy of C=O bonds is high (750 kJ mol^{-1}), and further leads to a high energy barrier[5,6]. CO_2RR suffers a low reaction rate because of this high activation barrier. In addition, when CO_2RR is conducted in an aqueous solution, the reaction involves multiple proton coupled electron transfer (PCET) processes, which leads to the variety of the reaction pathways, and this further results in limited selectivity and difficulty of the investigation of the mechanism. Finally, as the required thermodynamic energy of CO_2RR is comparable with hydrogen evolution reaction (HER, equation 1), strategies to suppress the HER side reaction should be considered, because it also consumes electrons and lower the performance of CO_2RR[4,5].

$2H^+ + 2e^- = H_2$ (1)

1.3.1 Influencing factors on performance of the reaction

To make carbon dioxide reduction meet the conditions of industrial application, a high reaction rate, high selectivity, and long duration should be achieved. We can optimize the reaction condition via rational designing electrocatalysts, changing the constituents of the electrolyte, and using different electrolysers to accomplish this goal.

1.3.1.1 Electrocatalysts

1.3.1.1.1 Homogenous Catalysts

During the past few decades, various electrocatalysts were developed for CO_2RR. These electrocatalysts can be classified into two categories: heterogeneous catalysts, and homogenous catalysts (Figure 1.8). The performance of a homogenous catalyst can be easily tuned by changing the metal center or organic ligands, and its reaction mechanism is also easy to characterize[23], which makes it become an attractive fundamental research direction. In nature, carbon monoxide dehydrogenases (CODHs) can catalyze the reaction of CO and H_2O into CO_2, protons, and electrons reversibly by equation 2[24]:

$$CO + H_2O \rightleftharpoons CO_2 + 2H^+ + 2e^- \quad (2)$$

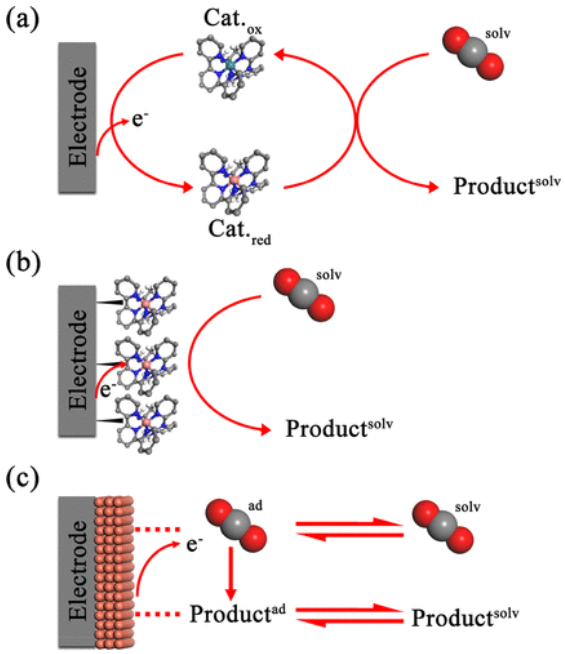

Figure 1.8 – CO_2RR mechanism of (a) homogeneous, (b) immobilized, and (c) heterogeneous catalyst system[25]. Reprinted (adapted) with permission from {Acc. Chem. Res. 2020, 53, 1, 255–264}. Copyright {2020} American Chemical Society.

CODHs have two basic categories: One has Ni_4Fe_4S as active sites from the anaerobic bacteria *Carbonxydothermus hydrogenoformans*, and another is Mo-S-Cu active sites which separated from *Oligotropha carboxidovorans* aerobic bacteria[26,27]. The reaction pathway is shown as followed (Figure 1.9a). Inspired by this, a series of homogenous catalysts were designed to mimic the active sites of CODHs and to be used for CO_2RR. For example, a copper complex, $[Cu_2(m\text{-}PPh_2bipy)_2\text{-}(MeCN)_2][PF_6]_2$, 22, ($PPh_2bipy$ = 6-diphenylphosphino-2, 20 -bipyridyl), and its pyridine analog, [Cu2(m-PPh2bipy)2-(py)2][PF6]$_2$, 2 (Fig. 1.9b), were synthesized for CO_2RR. CO was the only gas product. The catalyst was stable for 24h, and the turn-over frequency (TOF) is higher than 2 h^{-1}. Chronoamperometry showed that the rate constant k_{CO2} of 1 (0.6 M^{-1} s^{-1}) is higher than 2 (0.1 M^{-1} s^{-1}). These results showed that the changes in the ligands can change the electron transfer kinetics of CO_2RR and affect the activity[28].

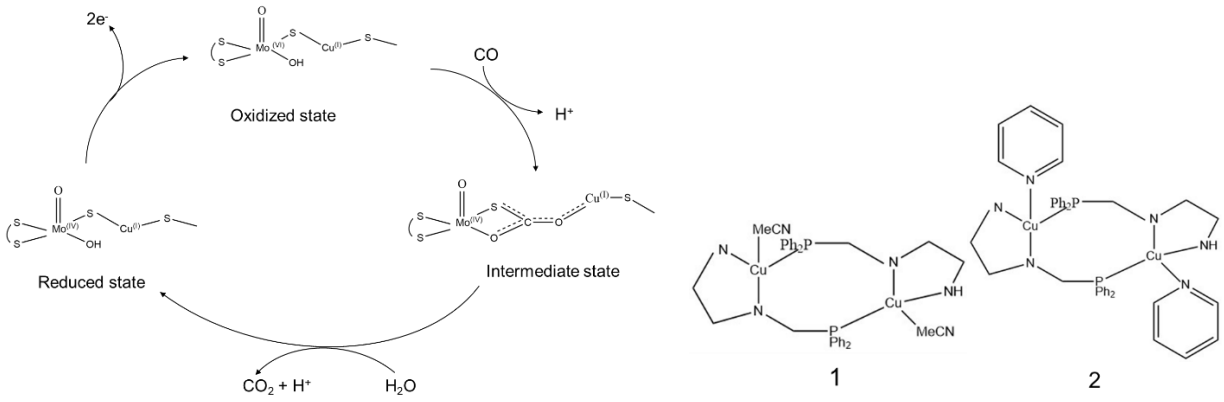

Figure 1.9 – Reaction mechanism of anaerobic CO dehydrogenases[28].

1.3.1.1.2 Heterogenous Catalysts

Although homogenous catalysts have many advantages, they still suffer a low conductivity (sluggish electron transfer) and stability, which limits their application in industry. Heterogenous catalysts can overcome these issues[23]. Heterogenous catalysts include metal electrocatalysts, transition metal oxides, transition metal chalcogenides, and carbon-based materials. According

to the final products and tendency to bind different intermediates, metal electrodes can be divided into three groups. Group 1 includes Sn, Hg, Pd, and In, which are capable to produce formate as the predominant product. Au, Ag, Zn, and Pd belong to group 2. Because their binding strength with the *CO intermediate is weak, CO can desorb from the surface of these electrodes and become the main product. Cu is the only metal in group 3, which has a moderate interaction with *CO (based on the principle of Sabatier, Figure 1.10), and it can promote C-C coupling and produce more valuable multicarbon (C_{2+}) products. However, using bulk Cu (such as Cu foil) requires a large overpotential (nearly 1 V), the selectivity of the product is low, and the deactivation of the catalyst is fast. Thus, we need to modify the Cu electrode (by changing the morphology or composition) to achieve higher performance[4,29].

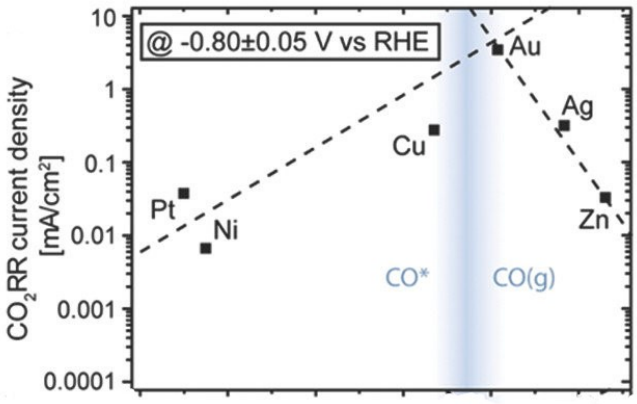

Figure 1.10 – Volcano plot of the current density for ECR at −0.8 V vs CO binding strength[29]. Reprinted (adapted) with permission from {J. Am. Chem. Soc. 2014, 136, 40, 14107–14113}. Copyright {2014} American Chemical Society.

Cu nanoparticles (NPs)

Cu NPs, usually exhibit higher activity than bulk Cu because of their distinct electronic and chemical surface properties (higher surface area). The performance of Cu NPs can be tuned by changing the size or shape[21]. When the size of Cu NPs becomes smaller, CO_2-to-CO selectivity can be enhanced because of the increase of low-coordinated atoms. The low-coordinated atoms can affect the binding strength of the reaction intermediates and leads to a change in selectivity. But HER was also enhanced, and the C-H products selectivity decreased. This is because low coordinated sites have a strong binding with both *CO and *H, which can promote the formation

of CO and H_2. Meanwhile, the hydrogenation of *CO is suppressed because the mobility of *CO and *H are reduced, which leads to a decrease in the FE of C-H products[30].

The shape of the catalyst is also capable of influencing CO_2RR activity and selectivity because it can change the exposure to different facets. For example, in a face-centered cubic (FCC) Cu with a cubic structure, Cu(100) is the dominant facets[11]. It resulted in higher selectivity of C_2H_4 and suppressed the formation of CH_4. Authors found that when the shape of Cu cubes was changed with the increase of the reaction time, Cu(100) gradually disappeared and led to a lower selectivity of C_2H_4, which proves (100) facets are beneficial for C-C coupling process[31]. Compared with Cu(100), (211) facets are preferential for CH_4 production, which proved by DFT calculation[32].

Oxide-derived Cu (OD-Cu) catalysts

OD-Cu, which is normally produced by the in-situ reduction of copper oxide, shows a lower overpotential and higher C_{2+} selectivity. But the reason for the performance enhancement of OD-Cu is still debated[21,33]. Experiments confirmed that the residual oxygen was negligible after CO_2RR reaction, while theoretical simulations revealed that (sub)surface oxygen, Cu^+ (the existence is proved by operando XAFS), and Cu^0 are beneficial to the activation of CO_2 and dimerization of CO, which might be a factor for improving the efficiency and selectivity[34]. Another possibility is (sub)surface oxygen and grain boundaries improve the stability of $*CO_2^{\cdot-}$, which results in higher activity and selectivity[35]. Electrochemically active surface area (ECSA) should also be considered as one of the factors on the performance of the catalyst, but it's difficult to confirm because of the complexity of the heterogeneous active sites[33]. Although there still exists doubt about the exact active sites, OD-Cu still deserves to be investigated because of its high performance.

Cu-based bimetallic catalysts

Incorporating secondary metal into Cu to form metal alloys is an alternative way to tune the activity and selectivity of CO_2RR[21]. Compared with bare Cu, bimetallics show a different CO_2RR performance because electronic effects (electronic structure changes), geometrical effects (different atomic arrangement of actives sites), and strain effect, which alters the binding strength and adsorption way of the intermediates by changing the d-band center. According to the different intrinsic properties, content and distribution of the secondary metal, the performance

of bimetallic catalysts are different. For instance, CuPd catalysts showed higher activity and selectivity of CO_2RR, the main products are CO or C_2H_4, which depends on the distribution of Pd. The authors proposed that geometric effect instead of electronic effects is the key point for the enhancement of C_2H_4 production. They used surface valence band photoemission spectra confirms that phase separated CuPd has a lower d-band center, and Cu shows a higher d-band position than CuPd, but they have similar activity and selectivity, which excludes the electronic effect on the performance. Ordered and disordered CuPd show a higher CO production, which is due to the desorption of CO being promoted by the changes in the electronic structure of Cu neighboring the Pd (Confirmed by DFT results)[36].

1.3.1.2 Electrolyte

In addition to electrocatalysts, the electrolyte is another factor that can impact the CO_2RR performance[21]. The intrinsic properties of the solvent (aqueous or non-aqueous), the concentration, pH value, species, and buffer capacity affect the local reaction condition and further influence the activity and product distribution of CO_2RR[33]. Understanding these effects is beneficial to the design of a highly efficient CO_2RR reaction system[37].

1.3.1.2.1 Organic solvents

CO_2 shows a higher solubility in organic solvents than water, and it can also avoid competitive HER reaction, and improve the selectivity of carbon species. Moreover, organic solvents can produce higher valuable C_{2+} species, such as oxalate, glycolic acid, glyoxylic acid, and tartaric acid[38]. Common organic solvents include acetonitrile, dimethylformamide (DMF), dimethyl sulfoxide (DMSO), hexamethylphosphoramide, methanol, propylene carbonate, and tetrahydrofuran (THF). Although organic solvents have lots of advantages, the price, toxicity, and safety hazard should also be considered for the applications. In addition, compared with water, organic solvents require a large overpotential for the formation of $CO_2^{\cdot-}$, which also limits their application[37].

1.3.1.2.2 Aqueous electrolyte

For sustainability, it's better to use water instead of organic solvents. Common aqueous electrolytes include alkali and ammonium salts of borates, (bi-)carbonates, halides, hydroxides,

(dihydrogen-, hydrogen-)phosphate, and (hydrogen-)sulfates[37,39-41]. Different concentrations, pH, cations, and anions can change the current density, overpotential, and FE of CO_2RR reaction system[37]. In the following part, we'll discuss this in detail.

Concentration and pH

Increasing the centration of the electrolyte can improve the conductivity of the electrolyte, it can also change the CO_2 solubility and pH. Higher solubility improves the CO_2RR efficiency because of the increase in the reactant. pH value can change the product distribution when using Cu as an electrocatalyst. Methane is preferably formed at low pH values, C_{2+} products (C_2H_4, C_2H_5OH, C_3H_7OH) predominate under higher pH values. The formation of CH_4 undergoes hydrogenation of *CO, which is the rate-determining step, it depends on the concentration of protons. This is why CH_4 needs a low pH environment, and this process is pH dependent. However, for C_{2+} formation, the rate determining step (RDS) is C-C coupling, which is achieved by the dimerization of *CO. Under alkaline conditions, hydrogenation of *CO is prohibited because of the low proton concentration, more *CO accumulates which favors C-C coupling. Thus, a higher pH is beneficial to produce C_{2+} products.

Cations and anions

Different ions in the electrolyte are also able to affect CO_2RR selectivity. Some studies show that on Cu electrodes, larger cations (e.g. Cs^+) result in higher CO_2RR rates, lower overpotential, and C_{2+} selectivity because the hydrolysis effect result in an increased buffering (lower local pH) and local concentration of CO_2 near the electrode surface. This result is evidenced by operando surface enhancement Raman and infrared absorption spectroscopy. Also, DFT calculation confirms that *OCCO and *OCCOH are more stable than *CO because of the cation effect, which also has a significant effect on C_{2+} production[39]. Anion (especially halide) effects have also been investigated on Cu, and the enhancement of CO_2RR with the addition of halide is because of the changing of electronic structure and the suppression of the proton adsorption. The product distribution can be changed by the size and concentration of anions. The enhancement of CO_2RR is followed by the order of $F^-<Cl^-<Br^-<I^-$. Anions increase the coverage of CO_{ads} on the catalyst

surface, which further promotes the protonation of CO_{ads}, and increases the FE of hydrocarbons as well as C_{2+} products[42].

1.3.1.3 Reaction cell

1.3.1.3.1 H cell

At present, most of the CO_2RR are conducted in an H cell. An H cell contains two chambers: an anode and a cathode chamber, which are separated by ion exchange membrane. The electrolyte is liquid, only cations or anions can pass through the membrane. Normally, a three electrode system is chosen, the counter electrode (CE) is set in the anodic part, the working electrode (WE) and reference electrode (RE) are set in cathode side. By this configuration, carbon species produced on WE cannot be reoxidized on CE, which can achieve a higher CO_2RR efficiency than the unseparated electrolyzer. Although this reaction system is simple and stable, it also suffers from low current density, because the reactant relies on the solubility of CO_2 in the solvent, which limits its application. Thus, an alternative reactor is needed for the industrial application of CO_2RR[43].

1.3.1.3.2 Flow cell

Flow cells can be divided into liquid-phase, gas-phase, and solid oxide flow cells (Figure 1.11). Like H cells, flow cells also contain anodic and cathodic two compartments. The main difference between these electrolyzers is electrolytes. Liquid-phase electrolyzers utilize a flow of liquid electrolyte (e.g., KHCO3, KOH, ionic liquids, etc.), in both cathode and anode chambers. Two chambers are also separated by a membrane, such as cation-exchange membrane (CEM), anion-exchange membrane (AEM), or bipolar membrane (BPM). CO_2 gas flow and catholyte are separated by cathode, and the reaction occurs on a gas-liquid-solid triple-phase interface of cathode catalyst layer because of the cathode contacts with both electrolyte and CO_2 gas flow, then carbon products form and come out. By this method, the limitation of the low solubility of CO_2 is overcome, which can improve CO_2RR efficiency. In a gas-phase electrolyzer, the configuration is similar to the liquid flow cell, the only difference is that the electrolyte of the cathode side is the water from humid CO_2 or the liquid from the diffusion of the anode chamber, and no extra electrolyte is added in the cathode chamber. It also contains CEM, AEM, or BPM.

The limitation of this cell is the accumulation of liquid products in the gas diffusion electrode, which can inhibit CO_2 diffusion to the catalytic layer of the cathode. For solid oxide reactor, there is no liquid electrolyte or membrane, the cathodic and anodic compartments are separated by metal oxide, and a high temperature is needed for this cell, which will consume more energy and may further increase the cost[43].

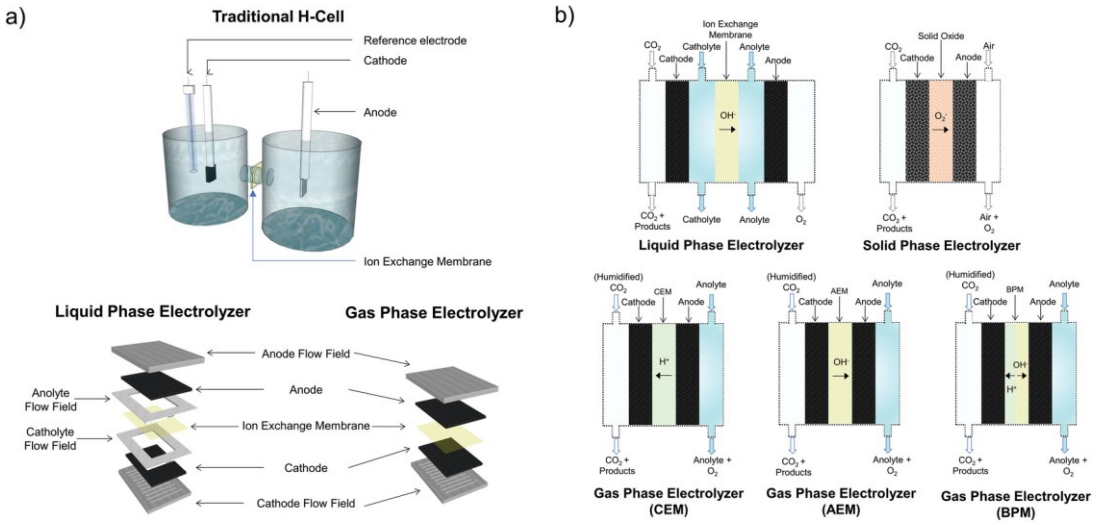

Figure 1.11 – Schematics of traditional H cell, liquid-phase electrolyzer, and gas-phase electrolyzer[43]. The figure of Adv Mater 31, e1807166. Copyright (2019) Wiley-VCH Verlag GmbH & Co. KGaA. Reproduced with permission.

1.3.1.3.3 GDE cells

Although flow cells show higher current density and selectivity than H cells, they still have some disadvantages: solid oxide reactors need high temperatures, the gas-phase flow cell will be filled by liquid products, and liquid-phase flow cell architecture is complex, pumps are needed to add electrolyte into the chambers and make a cycle. The gas diffusion electrode (GDE) is the heart of flow cells because it eliminates the limitation of the low solubility of CO_2 and enhances CO_2RR. Thus, we design a GDE cell instead of flow cell to conduct CO2RR to simplify the configuration of flow cell. The illustration of a GDE cell is shown as follows (Figure 1.12). GDE contains three parts: microporous substrate (MPS, bottom), microporous layer (MPL, middle), and catalyst layer (top). The function of MPS is to support the catalyst, transport electrons, and allows the diffusion of CO_2 to the surface of the catalyst. Common MPS materials are conductive carbon fibers or

titanium foam coated with hydrophobic materials, like polytetrafluoroethylene (PTFE), which can prevent the electrolyte penetrate the MPS and obstruct the diffusion of CO_2. MPL is used to improve the interfacial electrical connection and to avoid flooding in the GDE. MPL is a mixture of PTFE and carbon black. CO_2RR will occur on the catalyst layer. It can be obtained by a physical deposition method, growing the catalyst directly on the electrode, or drop-casting the mixture of ionomer binder and catalyst powder[43].

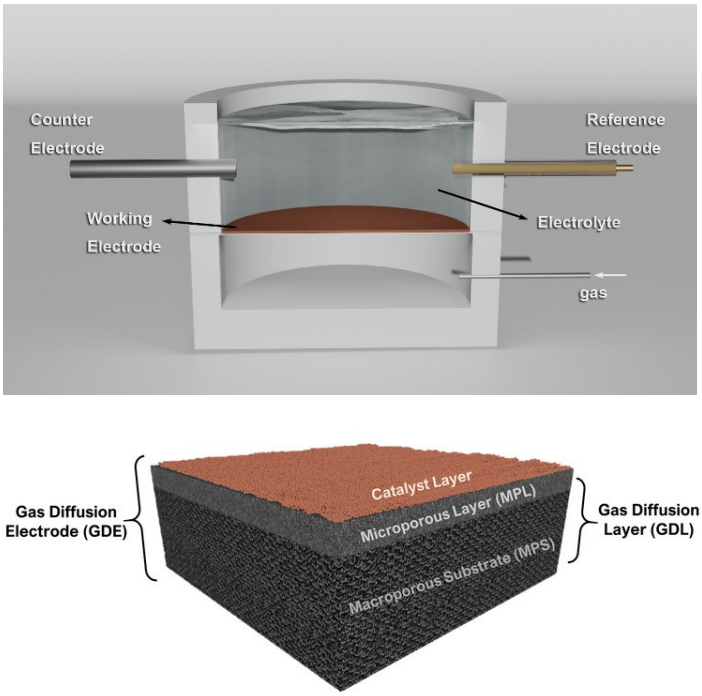

Figure 1.12 – Configuration of GDE cell[43,44]. The figure of Adv Mater 31, e1807166. Copyright (2019) Wiley-VCH Verlag GmbH & Co. KGaA. Reproduced with permission. Material from: 'J. Li et. al., ELECTROCHEMICAL FORMATION OF C–S BONDS FROM CO2 AND SMALL-MOLECULE SULFUR SPECIES, NATURE SYNTHESIS, published [2023], [Springer Nature]'. Reproduced with permission.

1.3.2 Reaction pathways

For a better understanding of the effects of the reaction condition on selectivity and activity, and designing the next generated highly efficient catalyst, understanding the reaction pathways is essential for the development of CO_2RR. Combining calculation and experiments, the mechanisms of the formation of C_1 and C_{2+} products are proposed. Detailed mechanisms of the reaction

depend on the intrinsic properties of the catalysts and reaction conditions, thus we only discuss the general reaction pathways in this section.

1.3.2.1 C_1 pathway

Formation mechanism of CO: The first step of CO_2RR is the activation of CO_2 molecular through proton-coupled electron transfer (CPET) to form *COOH intermediate (equation 3)[33].

$$* + CO_2 + H^+ + e^- \rightarrow *COOH \quad (3)$$

For the formation of CO by CO_2RR, the *COOH intermediate reacts with a proton and an electron to form *CO. If the interaction between the catalyst and *CO is weak, CO will desorb from the surface of the catalyst and form the final product of CO[6].

The mechanism of the formation of formate or formic acid includes two pathways: one is that the CO_2 molecule undergoes the CPET process to generate *OCHO intermediates (equation 4), and then *OCHO reacts with protons or electrons to generate formic acid or formate. The other is to generate HCOO- through the hydride transfer mechanism, then desorb to form formate or react with protons to form formic acid[45].

$$* + CO_2 + H^+ + e^- \rightarrow *OCHO \quad (4)$$

The initial process of the generation mechanism of methane, methanol, and formaldehyde is similar to the CO generation step. The difference is that the interaction strength between *CO and the catalyst is different, so the subsequent reactions are different, resulting in different products. Firstly, CO_2 will be activated to generate *COOH, then *COOH will be dehydrated to form *CO. If the interaction between *CO and catalyst is strong, CO molecules will not desorb, and *CO will further react with proton and electron to form *CHO or *COH. Finally, *CHO or *COH will interact with many protons or electrons through different pathways to form methane, methanol and formaldehyde, respectively[33].

1.3.2.2 C_2 pathway

The formation mechanism of ethylene, ethanol, and acetaldehyde: It is generally considered that the path through which the C_2 product is generated has the same intermediate, that is *CH_2CHO.

The formation process of the intermediates is as follows: When the interaction between *CO and the catalyst is strong, *CO will undergo carbon-carbon coupling reaction, to form *OCCHO. Subsequently, this intermediate will react with protons or electrons to form *CH_2CHO. *CH_2CHO can further undergoes hydrogeneration reaction to form ethanol or acetaldehyde, and ethylene will be produced by hydrogenolysis reaction[33,46].

The formation mechanism of acetate: Acetic acid is considered to be a by-product in the path to ethylene. It is formed by the isomerization of the three-membered ring species (*OCH_2COH) adsorbed on the surface of the catalyst and the coupling of different adsorption intermediates[47].

The formation mechanism of propanol and propionaldehyde: There are few studies on the formation mechanism of C_3 and C_{3+} compounds[33]. Propanol and propionaldehyde are formed by carbon-carbon coupling between CO and C_2H_4 precursors. In addition, the polymerization of carbon-active intermediate species adsorbed on the surface of the catalyst is also considered to be another mechanism for the formation of multiple-hydrocarbon products. There is still a lack of mechanistic work on the formation of C_{3+} compounds so far. The scheme of the reaction pathway is shown in Figure 13[5].

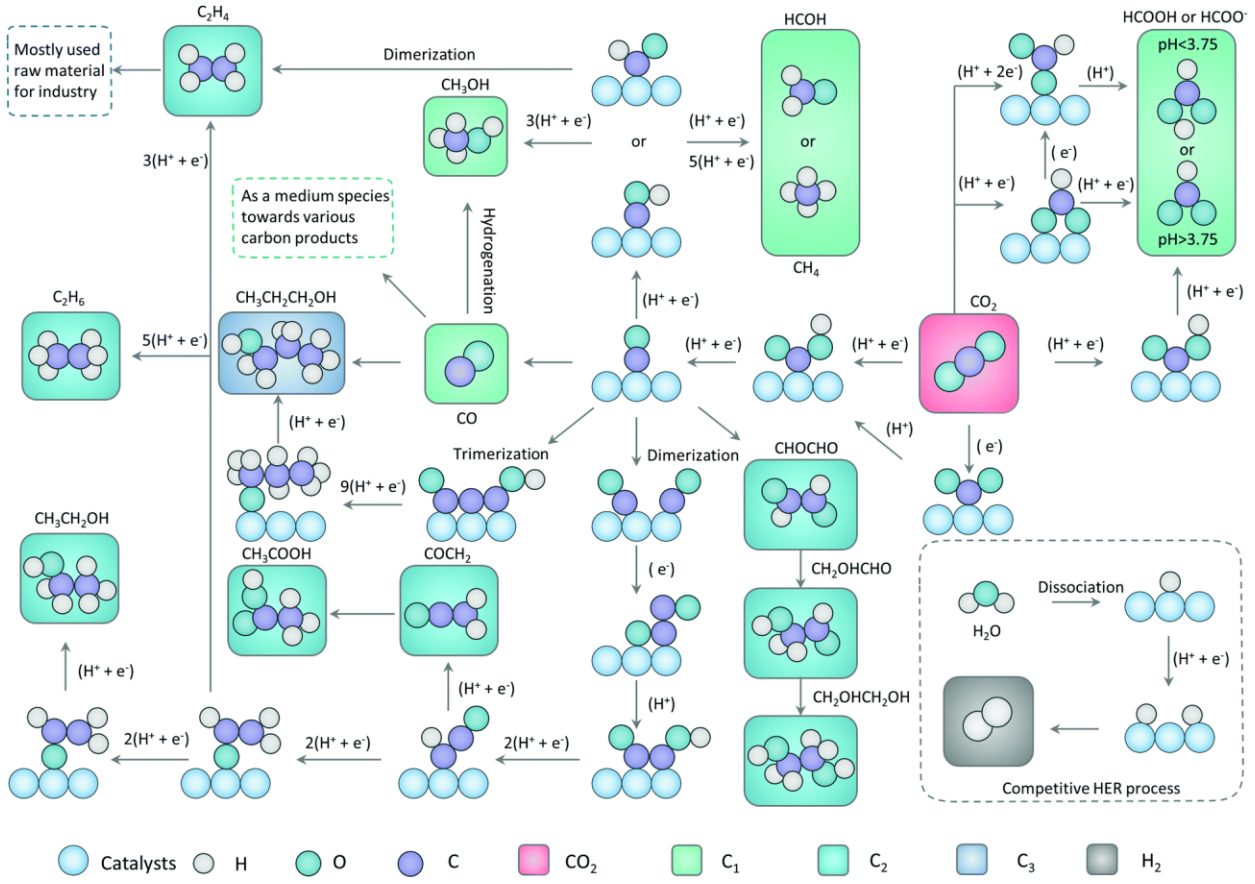

Figure 1.13 – CO_2RR roadmaps for different products[5]. Reproduced from Chem. Soc. Rev., 2022, 51, 1234–1252 with permission from the Royal Society of Chemistry.

1.3.3 Techniques for investigating mechanism of CO_2RR

As we mentioned above, understanding the mechanism and the effect of CO2RR is essential for designing next-generation highly efficient catalysts[5]. In-situ techniques can be used for investigating the evolution of the catalysts (active sites) during electrolysis process (such as in-situ X-ray Diffraction (XRD), X-ray Photoelectron Spectroscopy (XPS), X-ray Absorption Spectroscopy (XAS), Transmission Electron Microscopy (TEM)), the surface-bound reaction intermediates during the reaction (e.g., in-situ Raman, infrared (IR) or UV-vis), and the dynamics of the reaction (in-situ mass (MS) spectrometry to analyze the products in real-time)[3,34]. In this section, we will discuss the commonly used in-situ techniques in detail, operando Raman and IR, and briefly introduce some other useful in-situ techniques.

1.3.3.1 Optical spectroscopy

1.3.3.1.1 Operando Raman

Raman is one of the optical spectroscopies which can provide information about the structure of the molecules based on the rotation and vibration states of different molecules, by detecting the frequency of inelastically scattered light. Thus, it can be used for analyzing the reaction intermediates, the valence state changes of the catalysts and the potential active species during the reaction. Raman has a high sensitivity, especially suitable for aqueous systems because of the weak Raman scattering of water[3]. A water-immersion objective can also be used for obtaining a better signal. The Raman configuration is shown in Figure 1.14[48].

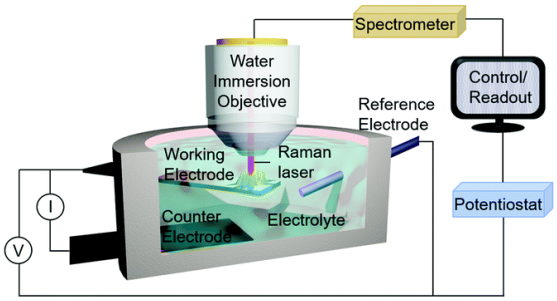

Figure 1.14 – Scheme diagram of operando Raman technique[48]. Reproduced from Chem. Sci., 2020,11, 1798-1806 with permission from the Royal Society of Chemistry.

Duan et al. used in-situ Raman to show that in the Cu^0-Cu^I tandem catalyst, Cu_2O was reduced to Cu^0 during CO_2RR, and there exists a Cu-CO bond, which confirms that Cu^0 species have a strong interaction with CO[49]. Yang et al. also used operando Raman to reveal the high activity of the Cu_2O catalyst with nanocavies, which is due to the retaining of Cu^+ active species[50]. Zhao et al. investigated the Raman spectrum of different Cu-based catalysts, Cu foil, Cu micro/nanoparticles, and OD-Cu, and prove that $CuO_x/(OH)_y$ is not the active species for C_{2+} oxygenates[51].

1.3.3.1.2 In-situ IR

IR is another powerful optical characterization technique that can be used to monitor the adsorbed species (intermediates) on the catalyst surfaces[3,5]. It is based on the specific adsorption of molecular vibrations. IR includes four configurations: transmission, diffuse reflectance,

attenuated total reflection (ATR), and reflection-absorption. In order to minimize the interference of the electrolyte layer and obtain better signals, ATR-IR is frequently used for investigating the intermediates during CO_2RR. The peak position of ATR-IR reflects the information of the chemical groups, and the intensity can be used to quantify the content of the corresponding species[34]. Similar to Raman, IR also shows a high sensitivity and fast detection speed. The in-situ IR cell is shown as Figure 1.15[52].

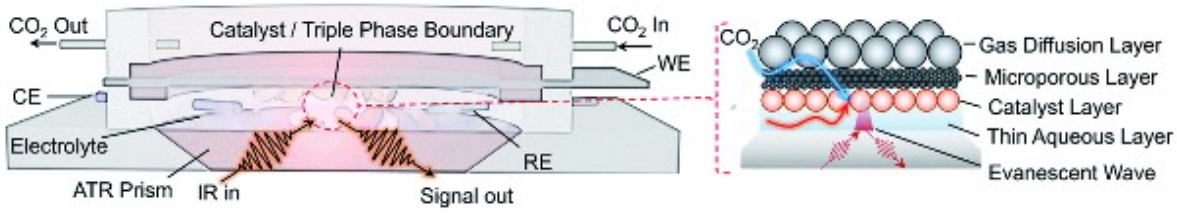

Figure 1.15 – Scheme of in-situ ATR-IR[52]. Reproduced from Chem. Sci., 2022,13, 3957-3964 with permission from the Royal Society of Chemistry.

Ma and his colleague used in-situ IR and DFT calculations to prove that the key intermediate for the formation of ethylene on the surface of fluorine-modified Cu catalyst is *CHO[53]. Ge et al. used in-situ IR to reveal the function of surfactant in the CO_2RR reaction. They found that the surfactant distribution transferred from random to a near-ordered assembly. These ordered surfactants change the interfacial microenvironment, and further enhance the co-electrolysis of CO_2 and H_2O[54].

1.3.3.1.3 In-situ UV-vis

Except for Raman and IR, UV-vis can also be used for detecting the organic species or reactive radicals according to the absorbed peak position. However, the accuracy of the UV-vis is low, and the test process is long (a few minutes), which limits its application[3].

1.3.3.2 X-ray characterization techniques

In-situ XRD is based on Bragg diffraction. It can reveal the evolution of the composition, crystal structure, and particle size of the catalyst during CO_2RR reactions by analyzing real-time diffraction patterns. The stability, phase transition, and active sites can be inferred based on the

information. But in-situ XRD can be only used for analyzing crystalline samples, and it is a bulk technique which means it is difficult to show the surface changes of the catalysts[3,55].

In-situ XPS can detect the photoelectrons, which are the electrons excited by photons. The element types, valence states, and coordination environment can be identified from XPS spectrum because the photoelectron energy is only related to atomic orbitals. Similar to in-situ XRD, in-situ XPS can also reveal the evolution of the catalyst and the information about active sites during CO_2RR. But it is a surface technique, which is hard to show the inner changes of the catalysts[3,34].

In-situ XAS is another surface detection technique that includes X-ray absorption near-edge structure (XANES) and the extended X-ray absorption fine structure (EXAFS). XANES focuses on the absorption edge (within ±1%), which displays the electron transition from occupied to unoccupied states, giving the information of valence states of the catalysts. EXAFS reflects the interference effect between ejected and backscattered photoelectrons and shows the bonding and coordination environment of the atoms. Thus, it can demonstrate both the catalyst changes and the information of intermediates during the reaction. It's the most widely used in-situ X-ray technique for CO_2RR[3,5,34,55].

1.3.3.3 Electron-based characterization and other techniques

Electron-based techniques include electron microscopy (TEM) and detection of electronic signals by scanning (scanning tunnelling microscopy, STM) or static probes. These techniques can be used to uncover the catalyst stability, catalytically active sites and help to infer the possible reaction pathways. For example, in-situ TEM is used to show the morphology changes of the catalyst during CO_2RR[56]. Scanning electrochemical microscopy (SECCM) can be used to characterize the liquid–solid–gas triple interfaces of the working electrode (electrocatalyst) in real time, providing the evolution of crystal facet and grain boundary. The configuration of the in situ SECCM is using scanning tip as a miniaturized electrode (reference electrode and the counter electrode), the working electrode is investigated by moving the probe across the surface of the electrocatalyst, the relationship between structural changes and the reaction performance can be recorded, which can be used for investigating the effect of the reaction environment[3,55].

Beyond these techniques, in-situ electron spin resonance (ESR) also plays a significant role in detecting the radicals formed on the surface of the catalysts. ESR can detect the unpaired electrons in the molecules because these electrons have magnetic resonance effect under an applied magnetic field. Thus, it's a useful technique for studying the mechanism of CO_2RR. In-situ MS shows the catalytic products in real time, which provides the dynamics information of the reaction. By analyzing the relationship between product distribution and reaction time, a possible reaction pathway can be proposed[3].

1.4 CO_2RR for synthesizing organic species with heteroatoms (nitrogen, sulfur)

In addition to C-H and C-O species, products with heteroatoms such as nitrogen (N) or sulfur (S) can also be synthesized by CO_2RR. Compared with traditional industrial organic synthesis methods, using CO_2RR to synthesize C-N or C-S bond compounds shows these advantages: 1. The reaction can be conducted at ambient temperature and pressure, which can save energy and cost; 2. The precursors CO_2 and N or S sources can be recycled from industrial waste gas or water, which can reduce the pollutants and avoid using fossil fuels as substrate, it's an environmentally friendly way; 3. The reaction can be easily tuned by altering the applied potential. As we mentioned above, product distribution relies on the range of applied voltage, we can synthesize different aim products by changing the potential. In all, using electrocatalytic CO_2RR to synthesize useful chemicals with heteroatoms is a green and sustainable way that is beneficial to the development of organic synthesis[57].

1.4.1 C-N bond formation

Constructing C-N bonds is important for organic and medical synthesis because C-N bonds compounds are prevalent in pharmaceutical reagents, natural products, synthetic intermediates, and organic materials. Right now, in traditional industrial synthesis method, the formation of C-N bonds includes C-H/N-X coupling (X = halide, pseudo-halide, including the transition-metal catalyzed Buchwald–Hartwig amination and Ullman aminations), cross-dehydrogenative coupling (CDC, C-H/N-H cross-coupling) and radical chemistry method. Among these methods, CDC was

the most attractive technique, because it can avoid the introduction of a function group before amination, achieve a high atom efficiency, can be conducted by electrochemical method, which makes it becomes the most straightforward and green approach for C-N bonds coupling[58]. Some works reported that using organic molecules with unsaturated C-C bonds as substrates (such as alkene, arenes) to produce C-N bond products[59,60], but for these reactions, organic solvents are needed which may pollute the environment. Also, the organic substrates are separated from fossil fuels, which is not good for a sustainable economy. Thus, we need to find a reaction that can be carried out in aqueous and an alternative carbon source that is not produced from fossil fuels.

1.4.1.1 Using CO and NH_3 as substrates

In 2019, Jouny et al. reported a C-N bond formation reaction by electrolysis of CO under ambient temperature and pressure with the addition of NH_3 in KOH electrolyte[61]. Acetamide was obtained as the C-N bond product, and the FE can reach around 40%. This reaction avoids using organic solvents, and CO can be produced from waste CO_2 gas, which makes C-N coupling by CO_2RR or CORR become attractive. Ketene from CORR is the key intermediate of this reaction, which undergoes an NH_3 nucleophilic attaction to form *C=C(OH)NH_2, and then through a keto-enol tautomerism form acetamide as the final C-N bond product (Figure 1.16). This reaction can also be extended by using different N sources, such as methylamine (CH_3NH_2) and ethylamine ($CH_3CH_2NH_2$), and N-methylacetamide and N-ethylacetamide are obtained as C-N bond products. But CO is a toxic gas for future applications, it's better to use CO_2 instead of CO as the precursor to synthesize C-N bond products[61].

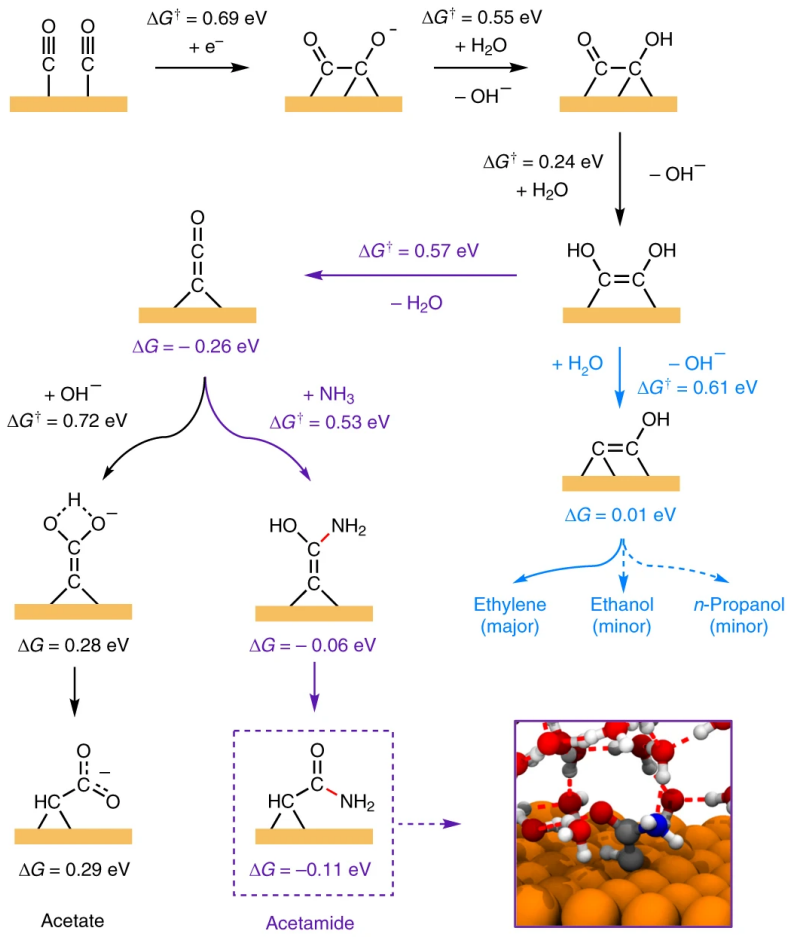

Figure 1.16 – Reaction mechanism of the production of acetamide by using CO_2 and NH_3 as precursors[61]. Material from: 'Matthew Jouny et. al., FORMATION OF CARBON–NITROGEN BONDS IN CARBON MONOXIDE ELECTROLYSIS, NATURE CHEMSITRY, published [2019], [Springer Nature]'. Reproduced with permission.

1.4.1.2 Coupling CO_2 with nitrite (or nitrate)

After the above work, the Shao group reported an electrochemical coupling of CO_2 and nitrite (NO_2^-) to synthesize urea in aqueous electrolyte[62]. They proposed the possible mechanism of the formation of urea, CO_2 is reduced to form *CO on the catalyst surface, and NO_2^- was reduced to $*NH_2$, the coupling between *CO and $*NH_2$ produces urea as the C-N bond product. But the FE of urea is low, it's 12.2%. This is because of the following side reactions: *CO can desorb from the surface to form CO, and $*NH_2$ can be protonated to form NH_3, also $*NO_2$ can form *ONNOH instead of $*NH_2$, which is the reaction pathway for N_2 formation. Inspired by this work, a series of

works has been reported with different catalysts to suppress the above competitive reactions, and the FE_{urea} can reach 55%[63]. In-situ spectroscopy techniques like Raman and FTIR are used for revealing the direct information of intermediates, and different mechanisms were proposed based on the spectrum result and DFT calculations. Nitrate (NO_3^-) can also be used as N source to replace NO_2^-, the first step is from HNO_3 to form $*NO_2$, and then $*NO_2$ react with H^+ and e^- to form $*NH_2$, followed by coupling with *CO or *COOH to form urea, or couple $*CO_2$ directly to form $*CO_2NO_2$ intermediate, and then react with protons and electrons to form urea[64].

Apart from urea, methylamine, and ethylamine are also obtained by co-electrolysis of CO_2 and nitrate[65,66]. The reaction pathway for the formation of methylamine and ethylamine are similar. NO_3^- adsorbed on the surface of the catalyst and forms *NO, then reacts with H^+ and e^- to form NH_2OH*. It will condense with HCHO* or CH_3CHO* from CO_2RR by nuclear attaction, and form $H_2C=NOH*$ or $CH_3CHNOH*$. These intermediates with C-N bonds further react with protons and electrons to form methylamine and ethylamine. But the FE of amine formation is lower than urea production, which is only 13% for methylamine and 0.3% for ethylamine[65,66].

1.4.1.3 Coupling CO_2 with N_2

N_2 can also be used as feedstock for C-N bond formation. The Wang group reported using CO_2 and N_2 as building blocks to synthesize urea[67]. In-situ SR-FTIR and DFT calculations show the reaction pathway of urea. N_2 and CO_2 molecules adsorb on the surface of the electrocatalyst, and form *N=N* and *CO as intermediates. The coupling between *N=N* and *CO to form *NCON* is the key step for urea formation, because *N=N* can form *NNH, which is the key intermediate for NH_3 production. In this article, the formation of *NCON* is an exothermic step (-0.89 eV), while *NNH is an endothermic step (+0.90 eV), thus the formation of urea is preferential, and the production of NH_3 is inhibited. Then *NCON* reacts with electrons and protons to form urea as the final C-N bond compound. The rate-determining step is the proton-coupled electron transfer process from $*NCONH_2$ (or *NHCONH) to $*NHCONH_2$. Although the formation of urea is thermodynamically and kinetically feasible, the FE_{urea} is still low (8.92%) because of the difficulty of the activation of N_2 and CO_2 molecules. In the following works, FE_{urea} can reach 20.97%, which provides a possibility to be applied in industrial production[68].

1.4.2 C-S bond formation

Similar with C-N bond products, C-S bond products are also essential in many fields, such as biology (nonribosomal peptides, enzymes), pharmaceutical industry (antibacterials, anticonvulsants, and hypoglycemics), agricultural and chemical industries. At the initial stage of the development of C-S bond coupling, people mainly use organic halides and thiol as precursors to synthesize C-S bond compounds under free-radicals or metal-catalyzed conditions, while this kind of reaction suffers a low atom economy[69]. C-H bond functionalization and decarboxylative reactions are potential methods to achieve a higher atom economy[70]. However, this reaction still has some limitations, such as forming a lot of waste, high cost of separation and the catalysts (most of the publications use noble metals), and the excessive addition of precursors or other reagents (nonstoichiometric)[69,71]. Thus, we need to find a new, cheap, and sustainable way for C-S bond formation reactions. Wang et al. reported an electrocatalytic dehydrogenative C−H/S−H cross-coupling method to synthesize organic sulfide at catalyst- and oxidant-free conditions (Figure 1.17)[72]. N-Methylindole (**3**) and 4-chlorothiophenol (**4**) were chosen as model substrates. **5** obtained an 85% yield. Various thiols and indoles with different substitutes (or other electron-rich arenes) are used to produce C-S bond products, and achieve a high yield (99%). While for this reaction, the substrates (N-Methylindole (1 a) and 4-chlorothiophenol (**4**)) still need to use fossil fuels as raw materials, and the organic solvent CH_3CN is also needed. In the periodic table of the elements, S has a diagonal relationship with N, which means that S has similar properties to N. According to the C-N bond formation from co-electrolysis of CO_2 with N sources, organic sulfides may also be obtained by coupling CO_2 with S species such as sulfide. Although there are few reports about this field, it's an attractive research direction because it can extend the scope of CO_2RR, and it is a green and sustainable method to synthesize C-S bond compounds without using organic solvents and substrates.

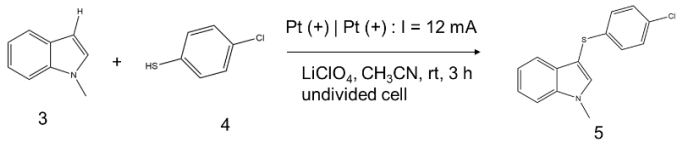

Figure 1.17 – Electrocatalytic oxidant-free dehydrogenative C−H/S−H cross-coupling with thiols[72]. The figure of Angew Chem Int Ed Engl 56, 3009-3013. Copyright (2017) Wiley-VCH Verlag GmbH & Co. KGaA. Reproduced with permission.

1.5 Research objectives

Based on sections 1.2 and 1.4, furfural reduction and CO_2RR are promising methods to solve the energy crisis and environmental problems, and also benefit the development of organic synthesis, but there still exist some unsolved problems. For the furfural reduction, although different catalysts are developed for the reaction, and the reaction conditions are investigated in detail, the reaction mechanism information is still lacking. As we mentioned in 1.3.3, in-situ techniques can give us direct information about the evolution of the active species and the reaction intermediates, thus we aim to use in-situ Raman to reveal the mechanism of FF reduction reaction. For using CO_2RR to synthesize C-N bond, we aim to use CO_2 instead of CO to conduct the experiment and use in-situ IR to show the reaction pathways of the formation of C-N products. Coupling CO_2RR with sulfur species to synthesize C-S bond compounds, it is still an unstudied field, thus we aim to use CO_2 and sulfide as feedstock to synthesize some organic sulfide molecules, and use in-situ techniques with DFT calculations to explain the formation of C-S bond products, and propose the possible key factors for improving the efficiency of the reaction.

Chapter 2: Using electrochemically roughed Cu foil as a model catalyst for the furfural reduction reaction, we used operando Raman to show the direct information about the reaction intermediates and the possible reaction pathways. The effects of different facets (single crystal) will also be investigated to confirm the active sites of the reaction. These experiments can help us to achieve the accurate tuning of the aim products.

Chapter 3: Coupling CO_2 and NH_3 to synthesize C-N bond products on Cu or CuO nanoparticles. The effect of different amounts of catalyst, concentration of NH_3, pH, cations, and potential are investigated to optimize the reaction conditions. Using operando IR we identify reaction intermediates and propose the reaction pathways of the formation of C-N bond compounds, providing useful information for designing next generated electrocatalysts with high performance.

Chapter 4: Co-electrolysis of CO_2 and sulfite in an aqueous solution produces organic sulfonates. Combining operando Raman and DFT calculation to uncover the key intermediate and the rate-determining step. Based on the mechanism we can develop a catalyst for synthesizing C-S bond products in a high yield in future. It will be the first time to report combining CO_2RR with the addition of sulfur species for C-S bond formation.

1.6 References

1 Gerardy, R., Debecker, D. P., Estager, J., Luis, P. & Monbaliu, J. M. Continuous Flow Upgrading of Selected C(2)-C(6) Platform Chemicals Derived from Biomass. *Chem Rev* **120**, 7219-7347, doi:10.1021/acs.chemrev.9b00846 (2020).

2 Kumar, A., Daw, P. & Milstein, D. Homogeneous Catalysis for Sustainable Energy: Hydrogen and Methanol Economies, Fuels from Biomass, and Related Topics. *Chem Rev* **122**, 385-441, doi:10.1021/acs.chemrev.1c00412 (2022).

3 Li, X., Wang, S., Li, L., Sun, Y. & Xie, Y. Progress and Perspective for In Situ Studies of CO2 Reduction. *J Am Chem Soc* **142**, 9567-9581, doi:10.1021/jacs.0c02973 (2020).

4 Zhu, D. D., Liu, J. L. & Qiao, S. Z. Recent Advances in Inorganic Heterogeneous Electrocatalysts for Reduction of Carbon Dioxide. *Adv Mater* **28**, 3423-3452, doi:10.1002/adma.201504766 (2016).

5 Li, L., Li, X., Sun, Y. & Xie, Y. Rational design of electrocatalytic carbon dioxide reduction for a zero-carbon network. *Chem Soc Rev* **51**, 1234-1252, doi:10.1039/d1cs00893e (2022).

6 Ross, M. B., *Luna P. D., Li Y., Dinh C., Kim D., Yang P. & Sargent E. H.* Designing materials for electrochemical carbon dioxide recycling. *Nat Catal* **2**, 648-658, doi:10.1038/s41929-019-0306-7 (2019).

7 Zheng, Y*., Vasileff A., Zhou X., Jiao Y., Jaroniec M, & Qiao S.*. Understanding the Roadmap for Electrochemical Reduction of CO2 to Multi-Carbon Oxygenates and Hydrocarbons on Copper-Based Catalysts. *J Am Chem Soc* **141**, 7646-7659, doi:10.1021/jacs.9b02124 (2019).

8 May, A. S. & Biddinger, E. J. Strategies to Control Electrochemical Hydrogenation and Hydrogenolysis of Furfural and Minimize Undesired Side Reactions. *ACS Catal* **10**, 3212-3221, doi:10.1021/acscatal.9b05531 (2020).

9 Li, N. & Zong, M.-H. (Chemo)biocatalytic Upgrading of Biobased Furanic Platforms to Chemicals, Fuels, and Materials: A Comprehensive Review. *ACS Catal* **12**, 10080-10114, doi:10.1021/acscatal.2c02912 (2022).

10 Kwon, Y., Schouten, K. J. P., van der Waal, J. C., de Jong, E. & Koper, M. T. M. Electrocatalytic Conversion of Furanic Compounds. *ACS Catal* **6**, 6704-6717, doi:10.1021/acscatal.6b01861 (2016).

11 Nitopi, S., Bertheussen E., Scott S. B., Liu X., Engstfeld A. K., Horch S., Seger B., Stephens I. E. L., Chan K., Hahn C., Nørskov J. K., Jaramillo T. F., & Chorkendorff I. Progress and Perspectives of Electrochemical CO2 Reduction on Copper in Aqueous Electrolyte. *Chem Rev* **119**, 7610-7672, doi:10.1021/acs.chemrev.8b00705 (2019).

12 De Luna P., Hahn C., Higgins D., Jaffer S. A., Jaramillo T. F., & Sargent E. H. What would it take for renewably powered electrosynthesis to displace petrochemical processes? *Science* **364**, doi:10.1126/science.aav3506 (2019).

13 Nilges, P. & Schröder, U. Electrochemistry for biofuel generation: production of furans by electrocatalytic hydrogenation of furfurals. *Energy & Environmental Science* **6**, 2925-2931, doi:10.1039/C3EE41857J (2013).

14 Chu, D., Hou Y., He J., Xu M., Wang Y., Wang S., Wang J. & Zha L. Nano TiO2 film electrode for electrocatalytic reduction of furfural in ionic liquids. *Journal of Nanoparticle Research* **11**, 1805-1809, doi:10.1007/s11051-009-9610-5 (2009).

15 Jung, S., Karaiskakis, A. N. & Biddinger, E. J. Enhanced activity for electrochemical hydrogenation and hydrogenolysis of furfural to biofuel using electrodeposited Cu catalysts. *Catal. Today* **323**, 26-34, doi:https://doi.org/10.1016/j.cattod.2018.09.011 (2019).

16 Lopez-Ruiz, J. A., Andrews, E., Akhade, S. A., Lee, M., Koh, K., Sanyal, U., Yuk, S. F., Karkamkar, A. J., Derewinski, M. A., Holladay, J., Glezakou, V., Rousseau, R., Gutiérrez, O. Y. & Holladay, J. D. Understanding the Role of Metal and Molecular Structure on the Electrocatalytic Hydrogenation of Oxygenated Organic Compounds. *ACS Catal* **9**, 9964-9972, doi:10.1021/acscatal.9b02921 (2019).

17 Jung, S. & Biddinger, E. J. Electrocatalytic Hydrogenation and Hydrogenolysis of Furfural and the Impact of Homogeneous Side Reactions of Furanic Compounds in Acidic Electrolytes. *ACS Sustainable Chem. Eng.* **4**, 6500-6508, doi:10.1021/acssuschemeng.6b01314 (2016).

18 Li, Z., Kelkar, S., Lam, C. H., Luczek, K., Jackson, J. E., Miller, D. J., Saffron, C. M. Aqueous electrocatalytic hydrogenation of furfural using a sacrificial anode. *Electrochimi Acta* **64**, 87-93, doi:https://doi.org/10.1016/j.electacta.2011.12.105 (2012).

19 Zhao, B., Chen, M., Guo, Q. & Fu, Y. Electrocatalytic hydrogenation of furfural to furfuryl alcohol using platinum supported on activated carbon fibers. *Electrochimi Acta* **135**, 139-146, doi:https://doi.org/10.1016/j.electacta.2014.04.164 (2014).

20 Jung, S. & Biddinger, E. J. Controlling Competitive Side Reactions in the Electrochemical Upgrading of

Furfural to Biofuel. *Energy Technology* **6**, 1370-1379, doi:10.1002/ente.201800216 (2018).

21 Gao, D., Arán-Ais, R. M., Jeon, H. S. & Roldan Cuenya, B. Rational catalyst and electrolyte design for CO2 electroreduction towards multicarbon products. *Nat Catal* **2**, 198-210, doi:10.1038/s41929-019-0235-5 (2019).

22 Qiao, J., Liu, Y., Hong, F. & Zhang, J. A review of catalysts for the electroreduction of carbon dioxide to produce low-carbon fuels. *Chem Soc Rev* **43**, 631-675, doi:10.1039/c3cs60323g (2014).

23 Banerjee, S., Anayah, R. I., Gerke, C. S. & Thoi, V. S. From Molecules to Porous Materials: Integrating Discrete Electrocatalytic Active Sites into Extended Frameworks. *ACS Cent Sci* **6**, 1671-1684, doi:10.1021/acscentsci.0c01088 (2020).

24 Benson, E. E., Kubiak, C. P., Sathrum, A. J. & Smieja, J. M. Electrocatalytic and homogeneous approaches to conversion of CO2 to liquid fuels. *Chem Soc Rev* **38**, 89-99, doi:10.1039/b804323j (2009).

25 Zhang, S., Fan, Q., Xia, R. & Meyer, T. J. CO(2) Reduction: From Homogeneous to Heterogeneous Electrocatalysis. *Acc Chem Res* **53**, 255-264, doi:10.1021/acs.accounts.9b00496 (2020).

26 Jeoung, J.-H. & Dobbek, H. Carbon Dioxide Activation at the Ni,Fe-Cluster of Anaerobic Carbon Monoxide Dehydrogenase. *Science* **318**, 1461-1464, doi:doi:10.1126/science.1148481 (2007).

27 Dobbek, H., Gremer, L., Meyer, O. & Huber, R. Crystal structure and mechanism of CO dehydrogenase, a molybdo iron-sulfur flavoprotein containing S-selanylcysteine. *Proceedings of the National Academy of Sciences* **96**, 8884-8889, doi:doi:10.1073/pnas.96.16.8884 (1999).

28 Haines, R. J., Wittrig, R. E. & Kubiak, C. P. Electrocatalytic Reduction of Carbon Dioxide by the Binuclear Copper Complex [Cu2(6-(diphenylphosphino-2,2'-bipyridyl)2(MeCN)2][PF6]2. *Inorg Chem* **33**, 4723-4728, doi:10.1021/ic00099a024 (1994).

29 Kuhl, K. P., Hatsukade, T., Cave, E. R., Abram, D. N., Kibsgaard, J. & Jaramillo, T. F. Electrocatalytic Conversion of Carbon Dioxide to Methane and Methanol on Transition Metal Surfaces. *J Am Chem Soc* **136**, 14107-14113, doi:10.1021/ja505791r (2014).

30 Reske, R., Mistry, H., Behafarid, F., Roldan Cuenya, B. & Strasser, P. Particle Size Effects in the Catalytic Electroreduction of CO2 on Cu Nanoparticles. *J Am Chem Soc* **136**, 6978-6986, doi:10.1021/ja500328k (2014).

31 Schouten, K. J. P., Pérez Gallent, E. & Koper, M. T. M. Structure Sensitivity of the Electrochemical Reduction of Carbon Monoxide on Copper Single Crystals. *ACS Catal* **3**, 1292-1295, doi:10.1021/cs4002404 (2013).

32 Liu, X., Xiao, J., Peng, H., Hong, X., Chan, K. & Nørskov, J. K. Understanding trends in electrochemical carbon dioxide reduction rates. *Nat Commun* **8**, 15438, doi:10.1038/ncomms15438 (2017).

33 Birdja, Y. Y., Pérez-Gallent, E., Figueiredo, M. C., Göttle, A. J., Calle-Vallejo, F. & Koper, M. T. M. Advances and challenges in understanding the electrocatalytic conversion of carbon dioxide to fuels. *Nat Energy* **4**, 732-745, doi:10.1038/s41560-019-0450-y (2019).

34 Handoko, A. D., Wei, F., Jenndy, Yeo, B. S. & Seh, Z. W. Understanding heterogeneous electrocatalytic carbon dioxide reduction through operando techniques. *Nat Catal* **1**, 922-934, doi:10.1038/s41929-018-0182-6 (2018).

35 Verdaguer-Casadevall, A., Li, C. W., Johansson, T. P., Scott, S. B., McKeown, J. T., Kumar, M., Stephens I. E. L., Kanan, M. W. & Chorkendorff I. Probing the Active Surface Sites for CO Reduction on Oxide-Derived Copper Electrocatalysts. *J Am Chem Soc* **137**, 9808-9811, doi:10.1021/jacs.5b06227 (2015).

36 Ma, S., Ma S., Sadakiyo, M., Heima, M., Luo, R., Haasch, R. T., Gold, J. I., Yamauchi, M., & Kenis, P. J. A. Electroreduction of Carbon Dioxide to Hydrocarbons Using Bimetallic Cu–Pd Catalysts with Different Mixing Patterns. *J Am Chem Soc* **139**, 47-50, doi:10.1021/jacs.6b10740 (2017).

37 Konig, M., Vaes, J., Klemm, E. & Pant, D. Solvents and Supporting Electrolytes in the Electrocatalytic Reduction of CO(2). *iScience* **19**, 135-160, doi:10.1016/j.isci.2019.07.014 (2019).

38 Fischer, J., Lehmann, T. & Heitz, E. The production of oxalic acid from CO2 and H2O. *J Appl Electrochem* **11**, 743-750, doi:10.1007/BF00615179 (1981).

39 Singh, M. R., Kwon, Y., Lum, Y., Ager III, J. W. & Bell, A. T. Hydrolysis of electrolyte cations enhances the electrochemical reduction of CO2 over Ag and Cu. *J Am Chem Soc* **138**, 13006-13012 (2016).

40 Dinh, C.-T., Burdyny, T., Kibria, MD G., Seifitokaldani, A., Gabardo, C. M., De Arquer, F. P. G., Kiani, A., Edwards, J. P., De Luna, P., Bushuyev, O. S., Zou, C., Quintero-Bermudez, R., Pang, Y., Sinton, D. & Sargent E. H. CO2 electroreduction to ethylene via hydroxide-mediated copper catalysis at an abrupt interface. *Science* **360**, 783-787 (2018).

41 Resasco, J., Lum, Y., Clark, E., Zeledon, J. Z. & Bell, A. T. Effects of anion identity and concentration on electrochemical reduction of CO2. *ChemElectroChem* **5**, 1064-1072 (2018).

42 Varela, A. S., Kroschel, M., Reier, T. & Strasser, P. Controlling the selectivity of CO2 electroreduction on copper: The effect of the electrolyte concentration and the importance of the local pH. *Catal Today* **260**, 8-13 (2016).

43 Kibria, M. G., Edwards, J. P., Gabardo, C. M., Dinh, C.-T., Seifitokaldani, A., Sinton, D. & Sargent, E. H. Electrochemical CO(2) Reduction into Chemical Feedstocks: From Mechanistic Electrocatalysis Models to System Design. *Adv Mater* **31**, e1807166, doi:10.1002/adma.201807166 (2019).

44 Li, J., Al-Mahayni, H., Chartrand, D., Seifitokaldani, A. & Kornienko, N. Electrochemical formation of C–S bonds from CO2 and small-molecule sulfur species. *Nat. Synth.*, doi:10.1038/s44160-023-00303-9

(2023).

45 Feaster, J. T., Shi, C., Cave, E. R., Hatsukade, T., Abram, D. N., Kuhl, K. P., Hahn, C., Nørskov, J. K. & Thomas, F. J. Understanding Selectivity for the Electrochemical Reduction of Carbon Dioxide to Formic Acid and Carbon Monoxide on Metal Electrodes. *ACS Catal* **7**, 4822-4827, doi:10.1021/acscatal.7b00687 (2017).

46 Hanselman, S., Koper, M. T. M. & Calle-Vallejo, F. Computational Comparison of Late Transition Metal (100) Surfaces for the Electrocatalytic Reduction of CO to C2 Species. *ACS Energy Lett* **3**, 1062-1067, doi:10.1021/acsenergylett.8b00326 (2018).

47 Liu, Y., Chen, S., Quan, X. & Yu, H. Efficient Electrochemical Reduction of Carbon Dioxide to Acetate on Nitrogen-Doped Nanodiamond. *J Am Chem Soc* **137**, 11631-11636, doi:10.1021/jacs.5b02975 (2015).

48 Heidary, N. & Kornienko, N. Electrochemical biomass valorization on gold-metal oxide nanoscale heterojunctions enables investigation of both catalyst and reaction dynamics with operando surface-enhanced Raman spectroscopy. *Chem Sci* **11**, 1798-1806, doi:10.1039/D0SC00136H (2020).

49 Duan, G. Y., Li, X., Ding, G., Han, L., Xu, B. & Zhang, S. Highly Efficient Electrocatalytic CO(2) Reduction to C(2+) Products on a Poly(ionic liquid)-Based Cu(0) -Cu(I) Tandem Catalyst. *Angew Chem Int Ed Engl* **61**, e202110657, doi:10.1002/anie.202110657 (2022).

50 Yang, P.-P., Zhang, X.-L., Gao, F.-Y., Zheng, Y.-R., Niu, Z.-Z., Yu, X., Liu R., Wu, Z.-Z., Qin S., Chi, L.-P., Duan, Y., Ma, T., Zheng, X.-S., Zhu, J.-F., Wang, H.-J., Gao, M.-R. & Yu, S.-H. Protecting Copper Oxidation State via Intermediate Confinement for Selective CO2 Electroreduction to C2+ Fuels. *J Am Chem Soc* **142**, 6400-6408, doi:10.1021/jacs.0c01699 (2020).

51 Zhao, Y., Chang, X., Malkani, A. S., Yang, X., Thompson, L., Jiao, F., & Xu, B. Speciation of Cu Surfaces During the Electrochemical CO Reduction Reaction. *J Am Chem Soc* **142**, 9735-9743, doi:10.1021/jacs.0c02354 (2020).

52 Li, J. & Kornienko, N. Electrochemically driven C–N bond formation from CO2 and ammonia at the triple-phase boundary. *Chem Sci* **13**, 3957-3964, doi:10.1039/D1SC06590D (2022).

53 Ma, W., Xie, S., Liu, T., Fan, Q., Ye, J., Sun, F., Jiang, Z., Zhang, Q., Cheng, J. & Wang, Y. Electrocatalytic reduction of CO2 to ethylene and ethanol through hydrogen-assisted C–C coupling over fluorine-modified copper. *Nat Catal* **3**, 478-487, doi:10.1038/s41929-020-0450-0 (2020).

54 Ge, W., Chen, Y., Fan, Y., Zhu, Y., Liu, H., Song, L., Liu, Z., Lian, C., Jiang, H. & Li, C. Dynamically Formed Surfactant Assembly at the Electrified Electrode–Electrolyte Interface Boosting CO2 Electroreduction. *J Am Chem Soc* **144**, 6613-6622, doi:10.1021/jacs.2c02486 (2022).

55 Li, J. & Gong, J. Operando characterization techniques for electrocatalysis. *Energy & Environmental*

Science **13**, 3748-3779, doi:10.1039/d0ee01706j (2020).

56 Li, J., Zhang, Y., Kuruvinashetti, K. & Kornienko, N. Construction of C–N bonds from small-molecule precursors through heterogeneous electrocatalysis. *Nat Rev Chem* **6**, 303-319, doi:10.1038/s41570-022-00379-5 (2022).

57 Zhao, Y. & Xia, W. Recent advances in radical-based C-N bond formation via photo-/electrochemistry. *Chem Soc Rev* **47**, 2591-2608, doi:10.1039/c7cs00572e (2018).

58 Gentry, E. C. & Knowles, R. R. Synthetic Applications of Proton-Coupled Electron Transfer. *Acc Chem Res* **49**, 1546-1556, doi:10.1021/acs.accounts.6b00272 (2016).

59 Tong, K., Liu, X., Zhang, Y. & Yu, S. Visible-Light-Induced Direct Oxidative C-H Amidation of Heteroarenes with Sulfonamides. *Chemistry* **22**, 15669-15673, doi:10.1002/chem.201604014 (2016).

60 Jouny, M., Lv, J.-J., Cheng, T., Ko B. H., Zhu, J.-J., Goddard, W. A. III & Jiao F. Formation of carbon-nitrogen bonds in carbon monoxide electrolysis. *Nat Chem* **11**, 846-851, doi:10.1038/s41557-019-0312-z (2019).

61 Feng, Y., Yang, H., Zhang, Y., Huang X., Li,, L., Cheng, T., and Shao, Q. Te-Doped Pd Nanocrystal for Electrochemical Urea Production by Efficiently Coupling Carbon Dioxide Reduction with Nitrite Reduction. *Nano Lett.* **20**, 8282-8289, doi:10.1021/acs.nanolett.0c03400 (2020).

62 Shibata, M., Yoshida, K. & Furuya, N. Electrochemical Synthesis of Urea at Gas-Diffusion Electrodes: IV. Simultaneous Reduction of Carbon Dioxide and Nitrate Ions with Various Metal Catalysts. *J. Electrochem. Soc.* **145**, 2348-2353, doi:10.1149/1.1838641 (1998).

63 Lv, C., Zhong, L., Liu, H., Fang, Z., Yan, C., Chen, M., Kong, Y. Lee C., Liu, D., Li, S., Liu, J., Song, L., Chen, G., Yan Q. & Yu, G. Selective electrocatalytic synthesis of urea with nitrate and carbon dioxide. *Nat Sustain* **4**, 868-876, doi:10.1038/s41893-021-00741-3 (2021).

64 Wu, Y., Jiang, Z., Lin, Z., Liang, Y. & Wang, H. Direct electrosynthesis of methylamine from carbon dioxide and nitrate. *Nat. Sustain* **4**, 725-730, doi:10.1038/s41893-021-00705-7 (2021).

65 Tao, Z., Wu, Y., Wu, Z., Shang, B., Rooney, C. & Wang, H. Cascade electrocatalytic reduction of carbon dioxide and nitrate to ethylamine. *J. Energy Chem.* **65**, 367-370, doi:https://doi.org/10.1016/j.jechem.2021.06.007 (2022).

66 Chen, C., Zhu, X., Wen, X., Zhou, Y., Zhou, L., Li, H., Tao, L., Li, Q., Du, S., Liu, T., Yan, D., Xie, C., Zou, Y., Wang, Y., Chen, R., Huo, J., Li, Y., Cheng, J., Su, H., Zhao, X., Cheng, W., Liu, Q., Lin, H., Luo, J., Chen, J., Dong, M., Cheng, K., Li C. & Wang, S. Coupling N2 and CO2 in H2O to synthesize urea under ambient conditions. *Nat Chem* **12**, 717-724, doi:10.1038/s41557-020-0481-9 (2020).

67 Yuan, M., Zhang, H., Xu, Y., Liu, R., Wang, R., Zhao, T., Zhang, J., Liu, Z., He, H., Yang, C., Zhang, S. &

Zhang, G. Artificial frustrated Lewis pairs facilitating the electrochemical N2 and CO2 conversion to urea. *Chem Catal* **2**, 309-320, doi:https://doi.org/10.1016/j.checat.2021.11.009 (2022).

68 Beletskaya, I. P. & Ananikov, V. P. Transition-Metal-Catalyzed C-S, C-Se, and C-Te Bond Formations via Cross-Coupling and Atom-Economic Addition Reactions. Achievements and Challenges. *Chem Rev* **122**, 16110-16293, doi:10.1021/acs.chemrev.1c00836 (2022).

69 Shen, C., Zhang, P., Sun, Q., Bai, S., Hor, T. S. A. & Liu, X. Recent advances in C-S bond formation via C-H bond functionalization and decarboxylation. *Chem Soc Rev* **44**, 291-314, doi:10.1039/c4cs00239c (2015).

70 Degtyareva, E. S., Borkovskaya, E. V. & Ananikov, V. P. Applying Green Metrics to Eco-Friendly Synthesis of Sulfur-Substituted Conjugated Dienes Based on Atom-Economic Hydrothiolation. *ACS Sustainable Chemistry & Engineering* **7**, 9680-9689, doi:10.1021/acssuschemeng.9b01405 (2019).

71 Wang, P., Tang, S., Huang, P. & Lei, A. Electrocatalytic Oxidant-Free Dehydrogenative C-H/S-H Cross-Coupling. *Angew Chem Int Ed Engl* **56**, 3009-3013, doi:10.1002/anie.201700012 (2017).

Chapitre 2 – Probing electrosynthetic reactions with furfural on copper surfaces

2.1 Résumé

Ce travail implique l'utilisation intégrée de l'électrochimie et de la spectroscopie Raman operando pour sonder la réduction d'une plate-forme de biomasse, le furfural, en produits chimiques à valeur ajoutée sur des électrodes de Cu. Les résultats révèlent des différences structurelles clés du Cu qui dictent la sélectivité pour l'alcool furfurylique ou le 2-méthylfurane.

Contribution:

Nikolay Kornienko and **Junnan Li** both designed the project, carried out experiments, processed data, contributed intellectual insights and wrote the manuscript.

Probing electrosynthetic reactions with furfural on copper surfaces

Junnan Li[1] and Nikolay Kornienko[1]*

[1]Department of Chemistry, Université de Montréal, 1375 Avenue Thérèse-Lavoie-Roux, Montréal, QC H2V 0B3, Canada.

*E-mail: nikolay.kornienko@umontreal.ca

Received: 16 Mar 2021; Accepted and First published:15 Apr 2021

DOI: 10.1039/D1CC01429C

Reproduced from *Chem. Commun.,* ***2021****,57, 5127-5130* with permission from the Royal Society of Chemistry.

2.2 Abstract

This work entails the integrated use of electrochemistry and *operando* Raman spectroscopy to probe the reduction of a biomass platform, furfural, to value-added chemicals on Cu electrodes. The results reveal key structural differences of the Cu that dictate selectivity for furfuryl alcohol or 2-methylfuran.

2.3 Introduction

Given the increasingly evident consequences of unmitigated fossil fuel consumption, there is a renewed focus on developing alternative energy technologies.[1] To this end, the innovation of renewable electricity-driven processes to replace current thermochemical ones is particularly attractive.[2-4] Ideally, such systems convert abundant reactants such as water, CO_2 or biomass (the focus of this work) into the fuels and chemicals necessary to power modern society.[5]

At the heart of electrosynthetic technologies is the catalyst which plays a principal role in determining the system's efficiency, selectivity, stability, and consequently economic viability. Underpinning the development of such highly performant catalysts is the fundamental understanding of how they function at a molecular level. Specifically, the interplay between applied potential, catalyst state, adsorbed intermediates and consequently reaction pathway should be uncovered and built upon. Against this backdrop, this work utilized an approach that combined electrochemical experiments and *operando* spectroscopy, that is, spectroscopy performed on the catalytic system as it is functioning.

The reaction of choice here was the electrochemical reduction of furfural, a biomass platform readily obtained from the dehydration of sugars.[6-8] While furfural is only modestly valuable, its reduction products of furfural alcohol (FA) and 2-methylfuran (2MF), widely used in resin production, flavourings, and alternative fuels.[6,7,9] In parallel, we chose Cu as the electrode material as it is inexpensive and has been shown to be active for such reactions in the past.[10-13] The particular contribution in this work is the novel extracted

insights into the molecular level reaction mechanism on Cu surfaces through the evaluation of both roughened and single crystal Cu surfaces and *operando* Raman spectroscopy (Fig. 2.1).

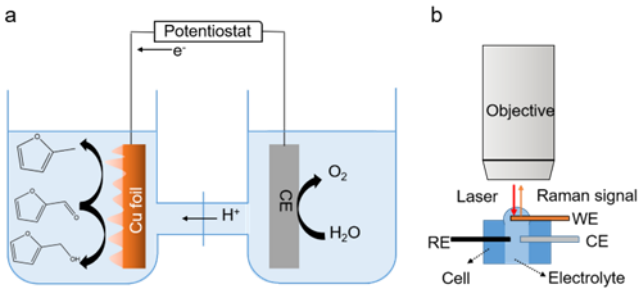

Figure 2.1 - Illustration of the approach of this work in using electrochemistry (a) and operando Raman spectroscopy (b) to develop a mechanistic understanding of furfural reduction on heterogeneous Cu electrodes.

In general, the reduction of furfural on Cu surfaces is believed to proceed through hydrogenation with surface hydrogen species. The kinetics and selectivity of furfural reduction is also steered by applied potential, reactant concentration, type of electrolyte and pH used.[8,10,12,14-16] However, comparatively less is known in terms of how catalyst-reactant interactions dictate the reaction at a molecular level.

2.4 Result and discussion

As a starting point, we used electrochemically roughened Cu (R-Cu) electrodes as model high-surface area catalysts which are free of any surface ligands and would also be suitable to use as surface-enhanced Raman (SER) substrates. R-Cu electrodes were generated by electrochemically cycling a polished polycrystalline Cu foil, resulting in an oxide-derived R-Cu material (Fig. 2.1 a).[17] This particular roughening procedure was chosen as it was established a method of reliably generating a SER-active electrode and its high surface area would be useful for attaining sufficient reaction rates for product quantification. However, it should be noted that the exact type surface roughness may affect local pH and reactant gradients, surface electromagnetic fields and the electrochemical double layer while the valence state and surface crystallinity would play a significant role in determining

binding energies of reactants and intermediates.[18-21] While these effects are not understood for furfural reduction as they are for more mature areas such as CO_2 reduction, they are nevertheless expected to play a significant role. Generally, the formation of undercoordinated surface sites, defects, and grain boundaries through the roughening procedure serves to increase the active site density and consequently the catalytic activity.

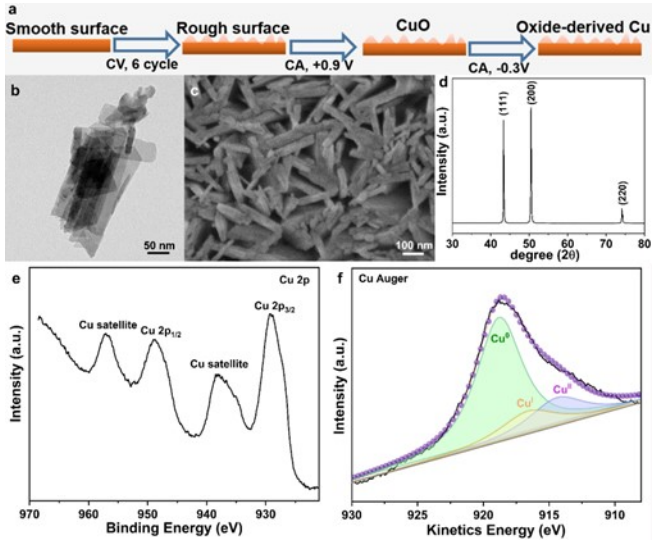

Figure 2.2 - Synthetic procedure of R-Cu (a) alongside of TEM (b), SEM (c), XRD (d) and XPS (e, f) of the resultant material**.**

Transmission electron microscopy (TEM) (Fig. 2.2b, 6.1) and scanning electron microscopy (SEM) (Fig. 2.2c) revealed the prevalence of a flake-like morphology on the surface as a result of the roughening procedure. X-ray diffraction (XRD) (Fig. 2.2d), X-ray photoelectron spectroscopy (XPS) (Fig. 2.2e, f) measurements indicated that the R-Cu is predominantly in the $Cu^{(0)}$ state but has a surface covered by an amorphous CuO_x layer.

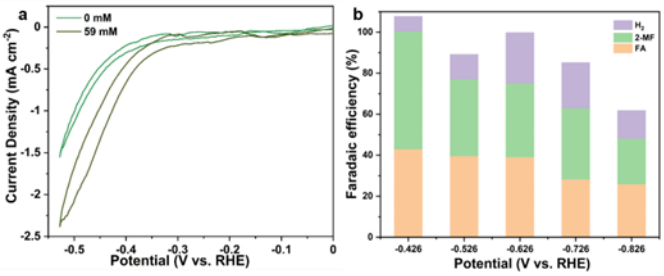

Figure 2.3 - CV scans of the R-Cu electrodes in the absence and presence of furfural (a) and product selectivity as a function of applied potential (b).

The R-Cu was first tested in a pH 3 electrolyte in a conventional 3-electrode electrochemical setup through cyclic voltammetry (CV). In the absence of furfural, reductive catalytic current due to the hydrogen evolution reaction (HER) initiated at approximately -0.4V vs. the reversible hydrogen electrode (RHE) (Fig. 2.3a). A noticeable enhancement in the catalytic current was evident upon the addition of furfural to the electrolyte in otherwise similar conditions. To initially optimize the reaction conditions, different amount of furfural was added in the electrolyte and CV curves are recorded. When the concentration of furfural was 59 mM, the current density was maximal (Fig 6.2a). Higher concentrations may lead to surface saturation and inhibit proton reduction necessary for furfural hydrogenation.

Product quantification (NMR for liquid, gas chromatography (GC), for gas) was then used to probe the reactions occurring. At -0.426 V, the earliest potential in which products accumulated in sufficient quantities, the main products were FA and 2-MF, alongside of a minor amount of hydrogen gas (Fig 2.3b).

At more negative potentials, the Faradaic efficiency (FE) for FA and 2-MF decreased progressively with potential. This occurrence was likely due to an increase of undesirable reaction pathways involving dimerization or ring-opening reactions driven by the highly negative applied potentials or homogeneous side reactions occurring in the reaction medium.[13,16] While it is not possible to compare directly the efficiencies and selectivity of this process with hydrogenation of biomass performed via thermochemical methods as the power input is different (thermal/chemical vs. electric), it must be noted that thermochemical methods have also attained comparable or even higher selectivities in similar reactions as this.[22-24] A recent analysis suggest that there may even be a technoeconomic advantage for hybrid systems for specific reactions.[25] However, while thermocatalytic reactions are already largely economically practical, typically electrochemical reactions need to be conducted at 100-100 mA/cm^2 at 70% or higher

Faradaic efficiency to be reach that level. While this system is not yet there, improvements via reactor engineering and catalyst improvement offer a straightforward path forward.

Next, to probe the mechanism of this reaction on the R-Cu surface, we turned to *operando* Raman spectroscopy. This technique, alongside of complementary infrared and other related techniques, is playing a significant role in enhancing the community's understanding of catalyst transformations, reaction pathways, and in general, how to rationally design next-generation materials for electrosynthetic systems.[26,27]

In this experiment, we used a 633 nm laser, custom spectroelectrochemical cells and immersion objectives to acquire SER spectra but otherwise, the electrochemical conditions were the same. The resultant spectra were assigned on the basis of previous theoretical and experimental investigations.[28-30] Further, comparison to spectra of the R-Cu in the electrolyte without furfural present (Fig 6.3) and through surveying the literature enabled us to verify that the peaks not assigned in Figure 2.4 can be attributed to electrolyte species.

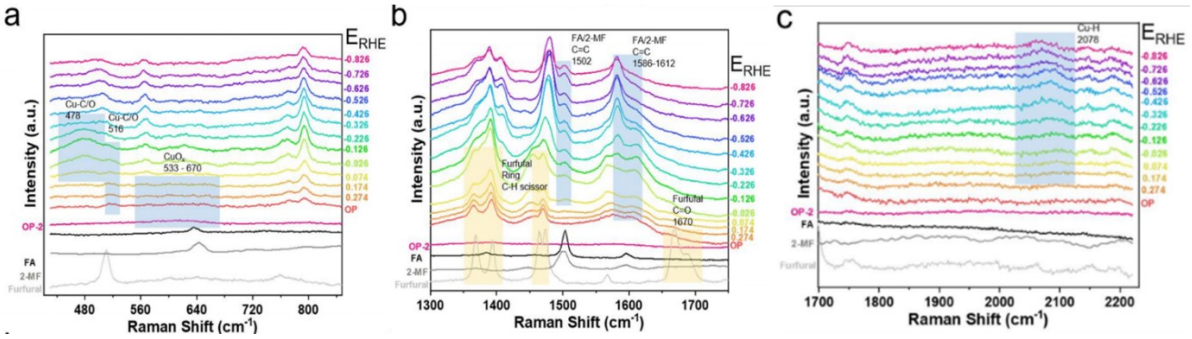

Figure 2.4 - Operando SER spectra of furfural reduction on R-Cu surfaces in the low frequency (a) and medium frequency (b) and high frequency (c) regions.

The spectra are divided into 3 distinct regions: the low frequency region which exhibits bands related to the catalyst-intermediate bands (Fig. 2.4a), the high frequency region which features marker bands related to furfural and the products and the high-frequency region containing the Cu-H stretch. OP denotes the spectra at open circuit and OP-2 signifies spectra at open circuit following the stepped chronoamperometry used for potential-dependent spectra. First, looking at the low frequency region, the surface of the

R-Cu is covered by an amorphous layer of oxidized copper (CuO_x).[17,31,32] As the potential is progressively increased, the CuO_x is reduced away to metallic Cu and several new bands appear. Cu-H intermediates from the reduction of aqueous protons appear, as do Cu-C and Cu-O intermediates, the latter two only detected in furfural containing solutions. The alternative possibility would be that these modes come from different types of surface sites or binding motifs. In general, unmarked bands are thought to originate from other electrolyte species as they are present in the spectra of the R-Cu without furfural.

In the medium frequency region, the spectrum at open circuit indicated that the aldehyde group of furfural was possible hydrated or distorted through interactions with the Cu surface, as seen before with Ag.[29] However, the rest of the furfural marker bands were easily seen. At progressively negative potentials, the furfural bands disappeared and C=C bands attributed to FA and 2-MF appeared. Several bands in the 1580-1612 cm^{-1} region may indicate a distribution of different intermediate on the surface en route to FA and 2-MF products. Unfortunately, the similarity of the FA and 2-MF spectra made it impossible to unambiguously distinguish between them. Compared with Figure 2.4b, Raman spectrum on R-Cu without addition of furfural showed a completely different result (Fig 6.3b). No C species were observed under this condition. This confirms that the peaks which were observed in Figure 2.4b is attributed to FA or 2-MF intermediates. Because reaction intermediates were readily seen at potentials more positive than reduction products could be detected in the bulk reaction, we postulate that the adsorption and initial reduction steps occur readily once the CuO_x layer is reduced away while the rate-limiting steps, in turn, are the hydrogenation and desorption of the intermediates. Finally, the high frequency region spectra, containing the typical M-H stretch,[33-35] indicated that hydrogen species become adsorbed strongly after -0.326 V_{RHE}. This occurs after the Cu-C/O intermediate bands appear and point to the hydrogenation of the intermediates after their adsorption being rate-limiting.

Because the R-Cu contained a variety of surface crystal facets and possible active sites, we sought to utilize single-crystal copper substrates as the next step. Figure 6.2b shows that Cu (110) showed the highest current density among the three single crystal Cu catalyst.

The current density of the addition of furfural is higher than without furfural (Figure 6.4). Using (100), (110) and (111) Cu substrates in an identical configuration as the R-Cu, we measured the product distribution at -0.526 and -0.726 $V_{RHE.}$ Interestingly, none of the electrodes generated any detectable 2-MF and only Cu(110) generated a significant amount of FA. This last observation indicates that Cu(110) surfaces are like the dominant component behind FA electrosynthesis under these conditions. In contrast, we hypothesized that electrochemically generated defects or surface/subsurface oxygen species remaining after the CuO_x layer reduction were primarily responsible for 2-MF generation. We confirmed this by electrochemically roughening the single crystal Cu surfaces and testing their activity. Indeed, 2-MF production could be recovered on the Cu(100) and Cu(111) substrates, through Cu(110) continued to exhibit selectivity for primarily FA (Fig 6.5). These results effectively establish a surface structural basis of Cu for directing selectivity of furfural reduction pathways (Fig 2.5).

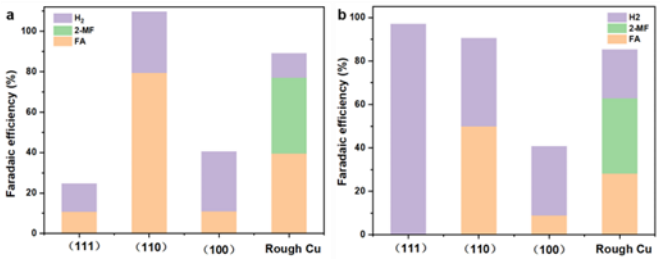

Figure 2.5 - Product distribution of single crystal and R-Cu electrodes at -0.526 (a) and -0.726 VRHE (b).

Combining the above results, we proposed a possible mechanism of furfural reduction. At the initial stage of the reaction, the copper oxide surface layer is reduced to metallic copper and protons are reduced to H atoms (H_{ads}) on the metallic surface. In parallel, furfural adsorbs onto the surface. Subsequently, H_{ads} will interact with absorbed furfural molecule and hydrogenate aldehyde group leading to the formation of a C-O bond and O-H bond. If this intermediate desorbed from the surface of the catalyst, FA will form as the final product. This is the dominant pathway on Cu(110) However, if the molecule is retained on the surface and the carbon is further hydrogenated by H_{ads}, the alcohol C-O bond is cleaved and 2-MF is formed. We can rule out the sequential reduction of FA into

2-MF as significant contributor as no 2-MF products were detected in FA reduction electrolysis.

2.5 Conclusion

To conclude, 2-MF and FA were obtained as the principal products of furfural reduction reaction with R-Cu electrocatalysts. *Operando* Raman spectroscopy illustrated that the intermediate formation occurred as the CuO_x layer was reduced away and enabled the proposal of a possible reaction mechanism. Investigation of single crystal Cu substrates demonstrated that Cu(110) has the best selectivity for FA production, while the defects likely contribute to 2-MF formation. This work puts forth a structural basis to the relationship between the catalytic activity and active species, key for catalyst design across a wide variety of electrosynthetic systems.

Conflicts of interest

There are no conflicts to declare.

2.6 References

1 S. Chu and A. Majumdar, *Nature*, 2012, **488**, 294-303.

2 V. R. Stamenkovic, D. Strmcnik, P. P. Lopes and N. M. Markovic, *Nature Mater.*, 2017, **16**, 57-69.

3 Z. Yan, J. L. Hitt, J. A. Turner and T. E. Mallouk, *Proc. Natl. Acad. Sci. U.S.A.*, 2020, **117**, 12558.

4 L. Du, Y. Shao, J. Sun, G. Yin, C. Du and Y. Wang, *Catal. Sci. Technol.*, 2018, **8**, 3216-3232.

5 F. W. S. Lucas, R. G. Grim, S. A. Tacey, C. A. Downes, J. Hasse, A. M. Roman, C. A. Farberow, J. A. Schaidle and A. Holewinski, *ACS Energy Lett.*, 2021, 1205-1270.

6 J.-P. Lange, E. van der Heide, J. van Buijtenen and R. Price, *ChemSusChem*, 2012, **5**, 150-166.

7 R. Mariscal, P. Maireles-Torres, M. Ojeda, I. Sádaba and M. López Granados, *Energy Environ. Sci.*, 2016, **9**, 1144-1189.

8 A. S. May and E. J. Biddinger, *ACS Catal.*, 2020, **10**, 3212-3221.

9 Y. Kwon, K. J. P. Schouten, J. C. van der Waal, E. de Jong and M. T. M. Koper, *ACS Catal.*, 2016, **6**, 6704-6717.

10 X. H. Chadderdon, D. J. Chadderdon, J. E. Matthiesen, Y. Qiu, J. M. Carraher, J.-P. Tessonnier and W. Li, *J. Am. Chem. Soc.*, 2017, **139**, 14120-14128.

11 P. Nilges and U. Schröder, *Energy Environ. Sci.*, 2013, **6**, 2925-2931.

12 Y. Cao and T. Noël, *Org. Process Res. Dev.*, 2019, **23**, 403-408.

13 S. Jung and E. J. Biddinger, *ACS Sustainable Chem. Eng.*, 2016, **4**, 6500-6508.

14 W. C. Albert and A. Lowy, *Trans. Electrochem. Soc.*, 1939, **75**, 367.

15 S. Jung, A. N. Karaiskakis and E. J. Biddinger, *Catal. Today*, 2019, **323**, 26-34.

16 S. Jung and E. J. Biddinger, *Energy Tech.*, 2018, **6**, 1370-1379.

17 I. V. Chernyshova, P. Somasundaran and S. Ponnurangam, *Proc. Natl. Acad. Sci. U.S.A.*, 2018, **115**, E9261.

18 L. Wang, S. Nitopi, A. B. Wong, J. L. Snider, A. C. Nielander, C. G. Morales-Guio, M. Orazov, D. C. Higgins, C. Hahn and T. F. Jaramillo, *Nature Catalysis*, 2019, **2**, 702-708.

19 A. S. Hall, Y. Yoon, A. Wuttig and Y. Surendranath, *J. Am. Chem. Soc.*, 2015, **137**, 14834-14837.

20 M. Liu, Y. Pang, B. Zhang, P. De Luna, O. Voznyy, J. Xu, X. Zheng, C. T. Dinh, F. Fan, C. Cao, F. P. G. de Arquer, T. S. Safaei, A. Mepham, A. Klinkova, E. Kumacheva, T. Filleter, D. Sinton, S. O. Kelley and E. H. Sargent, *Nature*, 2016, **537**, 382-386.

21 P.-P. Yang, X.-L. Zhang, F.-Y. Gao, Y.-R. Zheng, Z.-Z. Niu, X. Yu, R. Liu, Z.-Z. Wu, S. Qin, L.-P. Chi, Y. Duan, T. Ma, X.-S. Zheng, J.-F. Zhu, H.-J. Wang, M.-R. Gao and S.-H. Yu, *J. Am. Chem. Soc.*, 2020, **142**, 6400-6408.

22 F. Liu, W. Kong, L. Wang, X. Yi, I. Noshadi, A. Zheng and C. Qi, *Green Chemistry*, 2015, **17**, 480-489.

23 F. Liu, X. Yi, W. Chen, Z. Liu, W. Chen, C.-Z. Qi, Y.-F. Song and A. Zheng, *Chemical Science*, 2019, **10**, 5875-5883.

24 F. Liu, B. Li, C. Liu, W. Kong, X. Yi, A. Zheng and C. Qi, *Catal. Sci. Technol.*, 2016, **6**, 2995-3007.

25 B. M. Tackett, E. Gomez and J. G. Chen, *Nature Catalysis*, 2019, **2**, 381-386.

26 N. Heidary, K. H. Ly and N. Kornienko, *Nano Lett.*, 2019, **19**, 4817-4826.

27 N. Heidary and N. Kornienko, *Chem. Commun.*, 2020, **56**, 8726-8734.

28 L. Strandman-Long and J. Murto, *Spectrochim. Acta, Part A*, 1981, **37**, 643-653.

29 T.-j. Jia, P.-w. Li, Z.-g. Shang, L. Zhang, T.-c. He and Y.-j. Mo, *J. Mol. Struct.*, 2008, **873**, 1-4.

30 T. Kim, R. S. Assary, L. A. Curtiss, C. L. Marshall and P. C. Stair, *J. Raman Spectrosc.*, 2011, **42**, 2069-2076.

31 M. He, C. Li, H. Zhang, X. Chang, J. G. Chen, W. A. Goddard, M.-j. Cheng, B. Xu and Q. Lu, *Nature Commun.*, 2020, **11**, 3844.

32 Y. Deng, A. D. Handoko, Y. Du, S. Xi and B. S. Yeo, *ACS Catal.*, 2016, **6**, 2473-2481.

33 E. Bennett, T. Wilson, P. J. Murphy, K. Refson, A. C. Hannon, S. Imberti, S. K. Callear, G. A. Chass and S.

F. Parker, *Inorg. Chem.*, 2015, **54**, 2213-2220.

34 J. F. Li, Y. F. Huang, Y. Ding, Z. L. Yang, S. B. Li, X. S. Zhou, F. R. Fan, W. Zhang, Z. Y. Zhou, D. Y. Wu, B. Ren, Z. L. Wang and Z. Q. Tian, *Nature*, 2010, **464**, 392-395.

35 K. O. Bugaev, A. A. Zelenina and V. A. Volodin, *Int. J. Raman. Spec.*, 2012, **2012**, 281851.

Chapitre 3 – Electrochemically Driven C-N Bond Formation from CO_2 and Ammonia at the Triple-Phase Boundary

3.1 Résumé

Les techniques électrosynthétiques gagnent en importance dans les domaines de la chimie, de l'ingénierie et des sciences de l'énergie. Cependant, la plupart des travaux dans le sens de l'électrocatalyse hétérogène synthétique se concentrent sur l'électrolyse de l'eau et la réduction du CO_2. Dans ce travail, nous avons élargi la portée de l'électrosynthèse de petites molécules en développant un schéma de synthèse qui couple CO_2 et NH_3 à une frontière gaz-liquide-solide pour produire des espèces avec des liaisons C-N. Plus précisément, en réunissant le CO_2 de la phase gazeuse et le NH_3 de la phase liquide sur des catalyseurs en cuivre solide, nous avons réussi à former pour la première fois des produits formamide et acétamide à partir de ces réactifs. Dans une étape complémentaire ultérieure, nous avons combiné l'analyse électrochimique et une méthode spectroélectrochimique operando nouvellement développée, capable de sonder la frontière gaz-liquide-solide susmentionnée, pour extraire un premier niveau d'analyse mécaniste concernant les voies de réaction de ces réactions et le système actuel. limites. Nous pensons que le développement et la compréhension de cet ensemble de voies de réaction joueront un rôle important dans l'élargissement de la compréhension de la communauté des réactions électrosynthétiques en surface et pousseront cet ensemble de technologies intrinsèquement durables vers une applicabilité généralisée.

Contribution :

Nikolay Kornienko and **Junnan Li** both designed the project, carried out experiments, processed data, contributed intellectual insights and wrote the manuscript.

Electrochemically Driven C-N Bond Formation from CO_2 and Ammonia at the Triple-Phase Boundary

Junnan Li[1] and Nikolay Kornienko[1]*

[1]Department of Chemistry, Université de Montréal, 1375 Avenue Thérèse-Lavoie-Roux, Montréal, QC H2V 0B3, Canada.

*E-mail: nikolay.kornienko@umontreal.ca

Recieved: 25 Nov 2021; Accepted: 25 Feb 2022; First published: 28 Feb 2022

DOI: 10.1039/D1SC06590D

Reproduced from *Chem. Sci.*, **2022**,13, 3957-3964 with permission from the Royal Society of Chemistry.

3.2 Abstract

Electrosynthetic techniques are gaining prominence across the fields of chemistry, engineering and energy science. However, most works within the direction of synthetic heterogeneous electrocatalysis focus on water electrolysis and CO_2 reduction. In this work, we moved to expand the scope of small molecule electrosynthesis by developing a synthetic scheme which couples CO_2 and NH_3 at a gas-liquid-solid boundary to produce species with C-N bonds. Specifically, by bringing in CO_2 from the gas phase and NH_3 from the liquid phase together over solid copper catalysts, we have succeeded in forming formamide and acetamide products for the first time from these reactants. In a subsequent complementary step, we have combined electrochemical analysis and a newly developed *operando* spectroelectrochemical method, capable of probing the aforementioned gas-liquid-solid boundary, to extract an initial level of mechanistic analysis regarding the reaction pathways of these reactions and the current system's limitations. We believe that the development and understanding of this set of reaction pathways will play significant role in expanding the community's understanding of on-surface electrosynthetic reactions as well as push this set of inherently sustainable technologies towards widespread applicability.

3.3 Introduction

With the increased focus on attaining global sustainability as a means to mitigate climate change and environmental degradation, the development of green technologies to enable the transition is increasingly important. Within this context, renewable electricity-powered electrosynthetic routes towards generating the fuels and chemicals that drive modern society stand to play a significant role if they manage to displace currently used fossil-fuel dependent methods.[1-4] While the recent decade of academic research has largely focused on water electrolysis[5] and CO_2 reduction[6] to generate H_2 and carbon-based fuels, respectively, there is no reason that the scope of heterogeneous electrosynthesis needs to be limited to these reactions. In principle, almost any commodity chemical can be synthesized from abundant small molecule building blocks (N_2, H_2O, CH_4, biomass…) if the proper catalytic system would be developed.[7] The difficulty in realizing this ambitious aim is that at this point, only relatively simple electrosynthetic

reactions over heterogeneous catalysts are well-understood and can be carried out at high rates and selectivity.

To this end, we moved to develop electrosynthetic routes to C-N bond formation using CO_2 and NH_3 as model building blocks. In general, despite the biological, societal and technological importance of many chemicals containing C-N bonds[8-11], the area of electrochemical C-N bond formation is very nascent. While biological[12-14] and chemical[8,15] routes are established, only few examples exist in carrying out C-N coupling on heterogeneous electrocatalysts. Thus, new reaction schemes and mechanistic insights in this context stand to provide a significant boost to the community[16-22]. In the context of heterogeneous catalysis, urea has previously been synthesized from co-electrolysis of N_2 or nitrate together with CO_2.[17,19,20,22] α-keto acids have been converted into amino acids with hydroxylamine as a N-source.[23] Further, CO was co-electrolyzed with a series of different amines to generate amide products[18]. Finally, a host biomass-derived furans were reductively aminated to produce to amine derivatives.[21] To expand the scope of possibilities of heterogeneously catalyzed C-N bond formation, we have developed a novel electrosynthetic scheme. Here, NH_3 from the liquid phase would react with CO_2 from the gas phase over a heterogeneous Cu catalyst at a gas-liquid-solid boundary (Fig.1). As such, we generated formamide and acetamide from CO_2 and NH_3 for the first time, opening up a new avenue to the research community. Through quantitative reaction analysis and newly-developed infrared spectroelectrochemical investigations, we have built up a set of mechanistic insights in terms of elucidating reaction pathways and performance limitations, thus enabling the rational design of next-generation electrosynthetic systems.

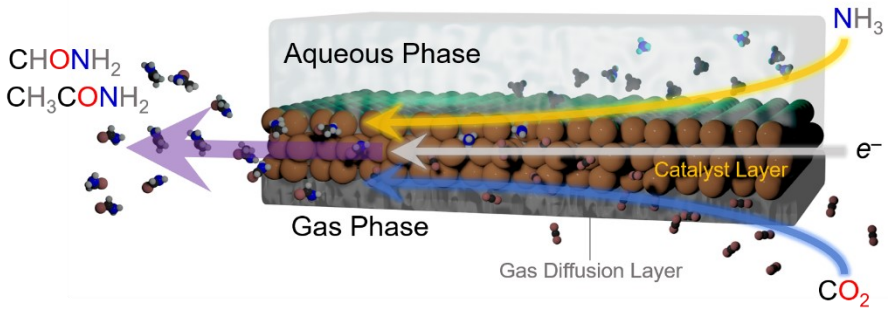

Figure 3.1 - Illustration of electrosynthetic strategy for on-surface C-N bond formation. A gas diffusion electrode was employed in which the reactants were simultaneously brought in from

the gas phase (CO_2) and from the liquid phase (NH_3) and reacted over a solid Cu catalyst onto which an electrochemical potential was applied. This configuration enabled the generation of formamide and acetamide C-N bond containing products.

3.4 Results and discussion

3.4.1 Catalyst Construction :

As a starting point, we selected two types of commercially available copper catalysts, Cu and CuO nanoparticles, for use in our study. Copper was selected as the element of choice because it has an intermediate binding energy to many carbon-based species.[24] This is a favorable metric in CO_2 reduction because it enables the retention of surface intermediates en route to the formation of highly reduced products like ethylene. At the same time, the binding strength to the intermediates is not too high to poison the surface. Thus, we reasoned that the same argument would apply in retaining CO_2 reduction intermediates long enough for their coupling with NH_3 would hold. While there is a plethora of studies of Cu-based catalysts and how defects, surface crystallographic facets, ligands, oxygen species and more dictate reaction pathways, we chose to leave such catalyst modifications for future follow-up works given the novelty of this reaction path.[24] The one variable that we did choose to investigate was the use of CuO as a starting material, which, when reduced to Cu under cathodic potentials, would likely contain additional binding sites in the form of defects. As such, Cu (Fig. 3.2a) and CuO (Fig. 3.2b) with no deliberate surface or structural modifications and size around 100 nm were used. The catalysts were mixed with a nafion binder to generate an ink which was then drop cast onto a gas diffusion electrode. This type of electrode featured a gas-permeable gas diffusion layer and microporous layer through which CO_2 could reach the catalyst layer on top (Fig. 3.2c). The goal here was to drive the C-N coupling reaction at this interfacial gas-liquid-solid boundary. This type of electrode geometry is particularly beneficial in overcoming the limited solubility of CO_2 in aqueous electrolyte through the use of alkaline electrolytes that minimize the competing hydrogen evolution reaction at industrially relevant current densities (hundreds of mA/cm^{-2}).[25-26] The reaction cell was a modified one from those commonly employed in the field in order to minimize reaction volume and

consequently maximize sensitivity for products. In particular, we employed an open cell design in which approximately 1 mL volume of electrolyte was used (Fig. 7.2).

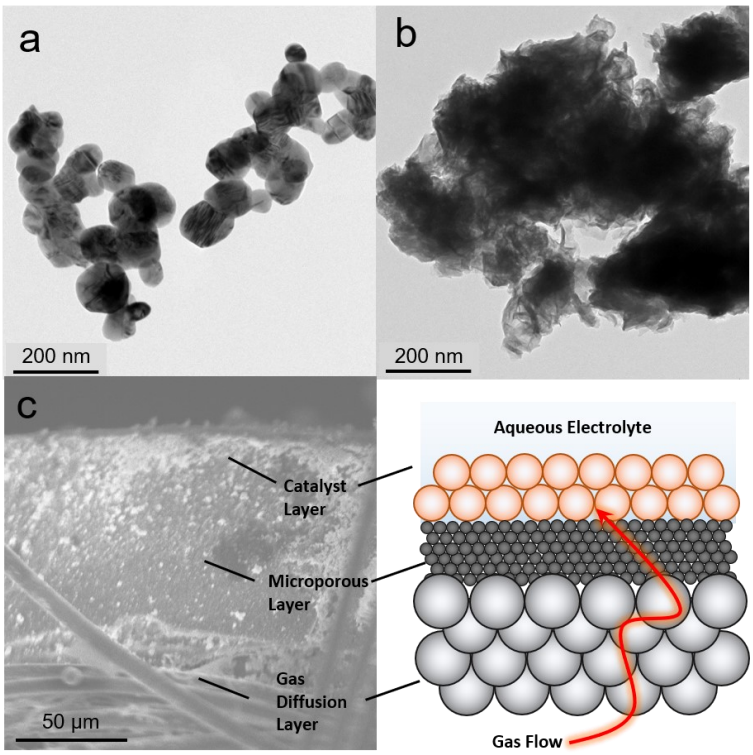

Figure 3.2 - The Cu (a) and CuO (b) catalyst particles were first characterized through transmission electron microscopy to probe their size and morphology. They were drop-cast onto a gas-diffusion electrode, which was characterized through scanning electron microscopy (c). The gas diffusion electrode consisted of several layers, illustrated with the graphic as a simplified representation. This electrode enabled gaseous reactants (CO_2 in this case) to reach a solid electrocatalyst (Cu/CuO) and circumvent the limited solubility of CO_2.

3.4.2 Electrosynthetic Studies:

We employed 1M KOH as an electrolyte for this work as highly alkaline electrolytes tend to minimize the hydrogen evolution reaction (HER) and thus favor CO_2 reduction. NH_3 was set to be a model nitrogen source. In the long term, NH_3 would ideally be replaced directly by N_2 as an abundant feedstock, though at this stage, electrochemically activating N_2 not yet a well-established reaction[27,28]. Formamide (Fig. 3.3a) and acetamide (Fig. 3.3b) primary amines were two likely C-N coupled products that could be formed from NH_3 and C_1 and C_2 surface

intermediates via several proton and electron transfer steps. In a gas-diffusion based electrochemical cell, both Cu and CuO featured an onset of catalytic current around 0 V vs. the reversible hydrogen electrode (RHE) and reached 100 mA/cm^2 by -1.0 V_{RHE} (Fig. 7.3 a,b). The addition of NH_4OH (present as mainly NH_3 in alkaline solutions) to the electrolyte did not significantly alter the current density. Product quantification with gas chromatography (GC) and NMR revealed formate and H_2 to be the two main products from the reaction (Fig. 7.4). However, on both Cu and CuO, formamide and acetamide were detected and were formed with partial current densities of ranging from 0.1 to 1.2 mA/cm^2, depending on the applied potential (Fig. 3.3c, d). While the Faradaic efficiency for their formation was rather modest, peaking at approximately 1% (Fig. 3e, f), this study constitutes the first report of their synthesis from CO_2 and NH_3 building blocks. In addition, performing the same measurements in a standard 3-electrode setup with the working electrode completely immersed in the aqueous phase did not result in any detectible C-N products, even after 24 hrs of electrolysis. This is likely due to a lower CO_2 concentration and lack of an alkaline environment that together promote a high degree of strongly bound C-based intermediates needed to couple with NH_3. As a control experiment, CO_2 electrolysis alone only resulted in formate (Fig. 3.3g) and acetate (Fig. 3.3h) products that gave rise to NMR peaks in the range of interest. Interestingly, while the formate selectivity was very high (up to 90%) without NH_3, NH_3 addition to the electrolyte decreased this value by a factor of 2-3 (Fig. 7.5) while promoting hydrogen evolution. While this performance is not yet sufficient for economically competitive electrosynthesis, improving the initial system should certainly be feasible as one could point to the rapid maturation of CO_2 electrosynthetic technologies over the last decade.[2]

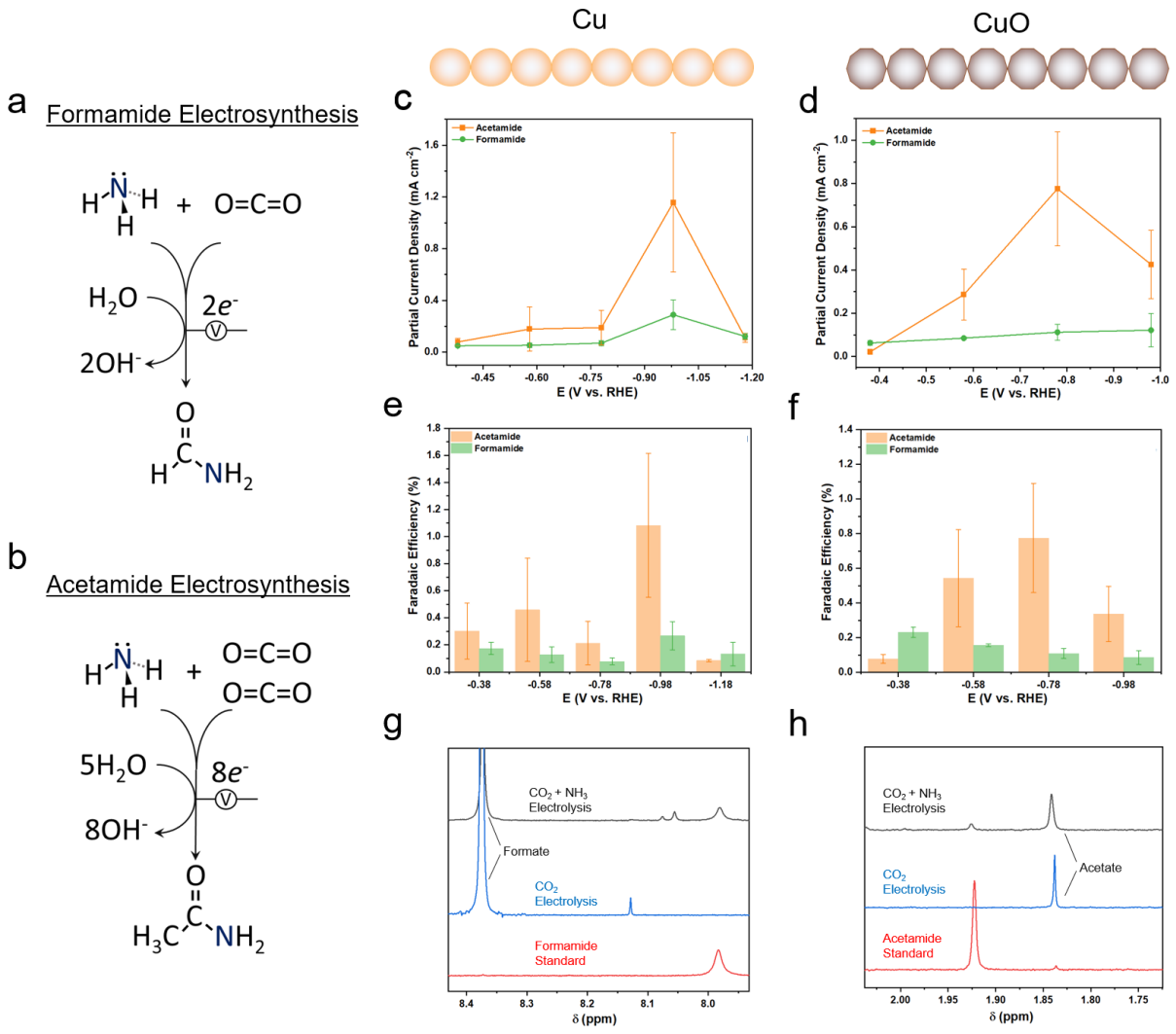

Figure 3.3 - The overall reaction is depicted for formamide involves 2 electrons and 1 CO_2 molecule (a) while acetamide electrosynthesis entails 8 electrons and 2 CO_2 molecules (b). In the gas diffusion electrode cell with a 1 M KOH electrolyte, 6 SCCM CO_2 flow, and the optimized concentration of NH_3, formamide (c) and acetamide (d) were quantified and their partial current densities derived from the resulting concentrations. The Faradaic efficiencies for both products were similarly obtained for Cu (a) and CuO (b) catalysts. Representative NMR spectra are shown for formamide (g) and acetamide (h) from which the concentrations are quantified.

3.4.3 Infrared Spectroscopy:

To extract a further level of insights into the formamide and acetamide electrosynthetic pathways, we turned to infrared spectroscopy.[29] This technique measures the vibrational modes of species within the electrolyte and on the catalyst surface. Typically, measurements are carried out in difference mode, using the system at open circuit as a refence and subtracting this from the spectra under applied bias, thus detecting the appearance of new species (positive bands) and disappearance of others (negative bands). The spectroscopic measurements were carried out in an attenuated-total reflection (ATR) mode using a home-built spectroelectrochemical setup (Fig. 3.4a). Briefly, a thin layer of aqueous electrolyte (KOH or KOH + NH_3) was on top of the diamond-coated ZnSe ATR crystal. The Cu catalyst layer/microporous layer/gas diffusion layer composite electrode was placed overtop so that the gas/liquid/solid boundary could be spectroscopically probed. In this configuration, the liquid was in static mode while the gas flowed above. The ability to probe this region was evident when measuring the difference spectrum between Ar flow and CO_2 flow in this configuration, which shows the presence of both gaseous and dissolved CO_2 and carbonate species (Fig. 7.12) .[30]

Under an argon flow with NH_3 and no CO_2, the main spectral features corresponded mainly to that of water and to that of NH_3 (Fig. 7.13-15).[30] Under the same conditions but with CO_2 flowing in place of Ar, a new set of positive bands appeared which can primarily be assigned to carbonate and bicarbonate species coming from CO_2 reacting with the KOH electrolyte and changes in pH (Fig. 7.14)[31]. Such species been shown to spontaneously appear at the gas-liquid-solid interface in similar conditions with Raman measurements.[32] While spectral features in the 1800-2100 cm^{-1} are noted where the C-O stretch of *CO is located, the inherent absorbance of our diamond-coated ATR crystal makes this region rather noisy rendering bands here more difficult to fit and explicitly assign.

In the presence of both CO_2 and NH_3, new bands appeared in the region containing N-H bonds from the generation of NH_4^+ (Fig. 3.4b).[33] As a method of validation, spectra were also acquired with $^{15}NH_3$ instead of $^{14}NH_3$ (Fig. 7.13). Indeed, the isotope effect was noted via a red-shift around 30 cm^{-1} for bands at both spectral regions. Interestingly, the intensity of the bicarbonate band at 1300 cm^{-1} saturated very early with only CO_2 present, but continually gained

intensity under increasingly higher currents when NH_3 was present (Fig. 7.13). A possible explanation for this could that be the presence of NH_3 diminishes the concentration of CO_2/carbonate reactants near the interface at low currents.

Finally, as (bi)carbonate species dominate the IR spectra, we opted to subtract spectra of the catalyst systems operating at -1 mA from those at -200 mA, as the (bi)carbonate species are mostly saturated and those with smaller spectral contributions could be visualized (Fig. 3.4c). Indeed, for the CuO catalyst in the presence of CO_2 and NH_3, the evolution of positive spectral features (1645, 1598, 1547 1402 and 1096 cm^{-1}) and negative bands (1660, 1425 and 1362 cm^{-1}) were noted. While a fully unambiguous assignment at this stage is not yet possible, we note that these spectral features correlate well with those previously assigned to $*COO^-$ and *COOH and these species are thus our tentative assignments.[34-36] The complete set of plausible band assignments is compiled in table 3.1.

As formate is the dominant product in each of these systems, it would seem reasonable to have a substantial $*COO^-$ surface coverage and thus this is our tentative assignment. While the precise mechanism of formate electrosynthesis is still under debate, on copper surfaces, it has been argued through a combination of surface-enhanced Raman spectroscopy and DFT modelling that the all CO_2 reduction pathways share a common first intermediate in a μ_2, -C, -O bound $CO_2{}^{*-}$ that subsequently gets hydrogenated en route to formate or protonated to *COOH en route to CO and other C_2 downstream products.[37] Thus, the observation of $*COO^-$ and *COOH intermediates being the main ones on the surface would support our product distribution.

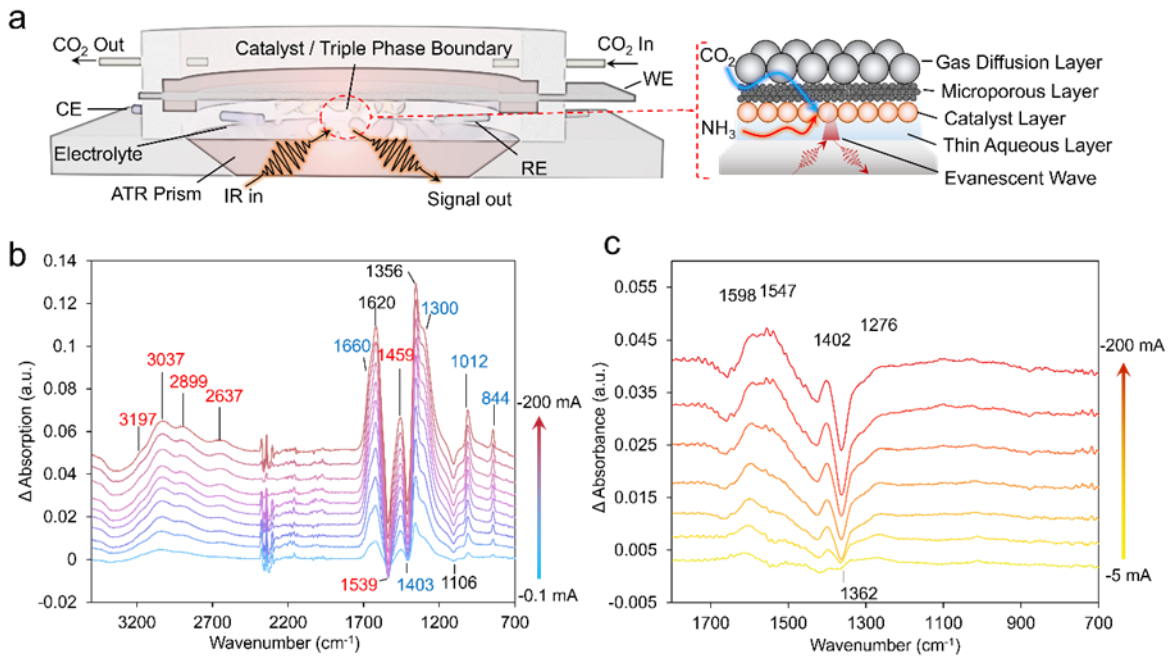

Figure 3.4 - Spectroelectrochemical setup enabling *operando* infrared spectroscopic probing of the electrosynthetic reactions in a gas-diffusion electrode cell (a). This setup used a thin electrolyte window with the GDE just overtop to probe both liquid, gas and solid phases. The gas was flowing through while the liquid was static. Using the spectrum at open circuit as the background, spectra under select operating current densities with CO_2 and NH_3 present were recorded (b). Subtracting out the bi(carbonate) contributions using the spectra at 1 mA/cm^2 as a background, enables the identification of additional species present on the CuO surface (c).

Table 3.1 - Peaks detected and plausible assignments from infrared experiments.

Band position (cm^{-1})	Species	Figure	Possible Assignment
1660	HCO_3^-	4b	ν_{as}(–C–O)[124]
1356	HCO_3^-	4b	ν(–C–O)[124]
1300	HCO_3^-	4b	δ(C–OH)[124]
1012	HCO_3^-	4b	ν_{as}(C–OH)[124]
844	HCO_3^-	4b	ν_s(C-OH)[131]
1459	CO_3^{2-}	4b	δ(–NH)[124]
3197	NH_4^+	4b	ν(N-H)[127]
3037	NH_4^+	4b	ν(N-H)[127]
2899	NH_4^+	4b	ν(N-H)[127]
1459	NH_4^+	4b	ν(N-H)[127]
1645	H_2O	4c	δ(H-O-H)
1598	*COO^-	4c	$\nu_{as}(COO^-)$[83]
1547	*COO^-	4c	$\nu_{as}(COO^-)$[129]
1402	*COO^-	4c	$\nu_s(COO^-)$[129,130]
1276	*COOH	4c	νCOOH, OH-deformation[129]

While this study used NH_3 as a starting point for generating C-N bond containing products, ideally, the nitrogen source would be gaseous N_2 as the technology matures and scales. To this end, we have explored as an intermediate step the co-reduction of nitrate and nitrite ions in place of NH_3 to generate the same products. The experimental procedure was the same except that the nitrate/nitrite was in place of NH_3 in the electrolyte, with optimized concentrations of NO_2/NO_3 (Fig. 7.15, 16). Over a Cu catalyst at -0.98 V vs. RHE, formamide and acetamide were indeed formed, albeit at reduced faradaic efficiencies and partial current densities (Fig. 3.5). While a comprehensive set of electroanalytical and spectroscopic experiments is outside of the scope of this initial work, the results indicate that there is much to discover in optimizing the reduction pathways of both C and N sources en route to C-N bond formation. A likely reaction pathway that would explain our results would be the reduction of nitrate/nitrite on the electrode surface to NH_3 or $*NH_2$, which then couples with intermediates from CO_2 reduction.

When using NH_3 as the starting point we believe that it is not directly bound to the surface but rather located in the near-surface region (Fig. 7.18). Its presence seems to hinder both hydrogen evolution and CO_2 reduction, likely through inhibiting reactant diffusion to active sites on the catalyst. The tendency to enhance hydrogen evolution likely stems through an enhanced hinderance of CO_2 diffusion as opposed to that of water molecules.

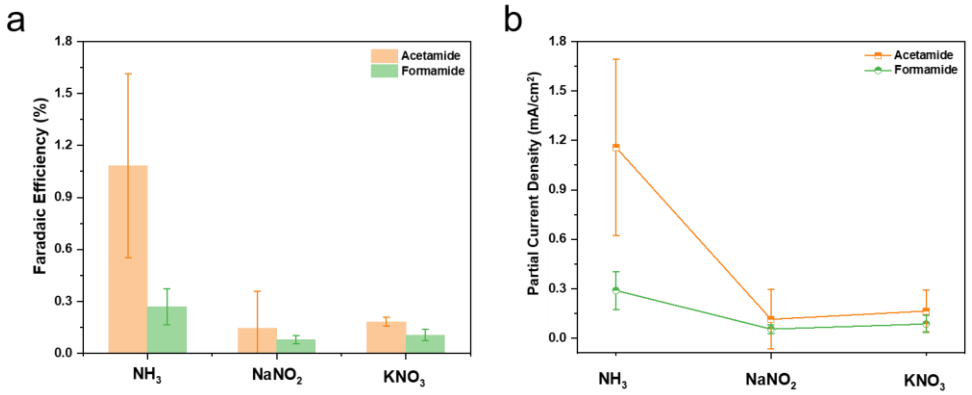

Figure 3.5 - In the equivalent reaction setup as in figure 3 with Cu catalysts and NO_2^- (0.5M) or NO_3^-(1M) in place of NH_3 at -0.98V vs. RHE, formamide and acetamide were generated. The Faradaic efficiencies (a) and partial current densities (b) for their generation were compared to those from using NH_3.

Finally, we moved to optimize the C-N product generation of our system. We first screened the parameters of KOH concentration, Cu catalyst loading, and cation identity (Fig. 7.21). The biggest enhancement in acetamide generation came from a higher Cu loading (10 mg/cm^2 vs. 2 mg/cm^2). We attribute this to the propensity of the catalyst layer to generate a higher amount of highly reduced C_2 intermediates through the thicker Cu film (Fig. 3.6 a, b). Further, a lower KOH concentration and a change from K^+ to Cs^+ also yielded selectivity enhancements for acetamide, possible due to a more favorable near-surface reaction environment to stabilize reaction intermediates en route to the C_2 species that can couple with NH_3.[39] Interestingly, the activity enhancements were not realized for formamide. This can be rationalized as the factors necessary for favorizing a CO_2 reduction pathway to C_2 species as not being necessary for formamide, which is more dependent on the initial $*COO^-$ intermediate coupling with NH_3.

Then, with all three optimized parameters incorporated (0.1M CsOH electrolyte, 10 mg/cm^1 Cu loading), we compared the Faradaic efficiency and partial current densities for the optimized system to that of the original from Fig. 3.2 across the experimental potential range (Fig. 3.6c).

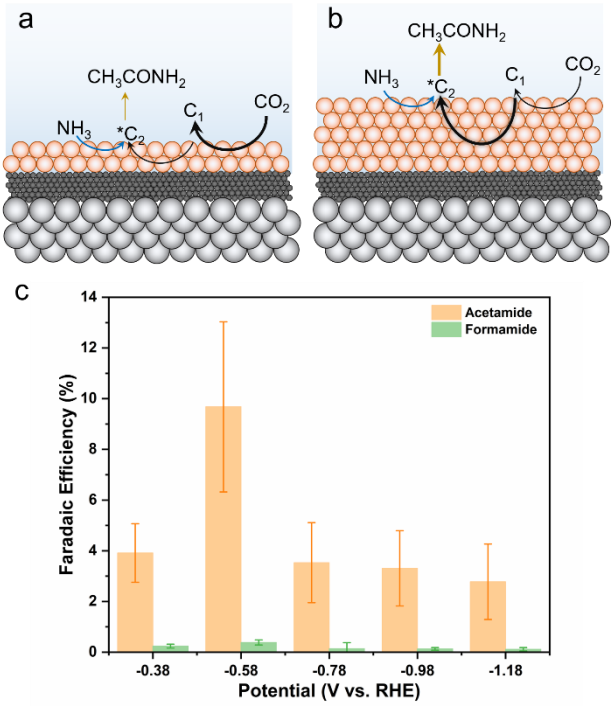

Figure 3.6 - A thicker catalyst loading was found to promote acetamide formation. Thin layers tend to form C_1 products at a greater rate (a) while increasing the layer thickness leads to further reduction and accumulation of C_2 intermediates that can be used for C-N bond formation (b). As such, an optimized Cu loading of 10 mg/cm^2 resulted in up to 10% acetamide selectivity (c).

We believe that the formate and formamide electrosynthetic pathways are linked on the Cu surface in that they share a common intermediate. This belief is backed by their similarity in chemical structure. Considering that the formation of C-N containing products involves the nucleophilic attack of a carbon atom by the lone pair on the nitrogen atom of ammonia, an activated, yet exposed carbon species that could couple with ammonia for formamide generation could be that of the μ_2, -C, -O bound $*CO_2^-$[37]. There would then be a competition between hydrogenation of this species to produce formate or a nucleophilic attack to eventually form formamide (Fig. 3.7a). This branching point is also supported by the fact that using 1M formate

instead of CO_2 as the C-source in otherwise identical conditions did not lead to any detectable formamide and only a small amount of acetamide (Figure 7.14).

On the other hand, acetamide synthesis likely shares a reaction pathway with acetate and thus requires a C_2 intermediate to already be present[18]. The branching for this step also plausible occurs at the $*CO_2^-$ intermediate, which is converted to *CO. The coupling of 2 *CO molecules is thought to be a key step to generating C_2 products (acetate, ethanol, ethylene). The *CCO intermediate was recently proposed as a likely candidate for this through a DFT analysis of acetamide synthesis via CO and NH_3 building blocks and would be a plausible candidate for our work as well.[18] The middle carbon would thus be subject to nucleophilic attack by the NH_3 in this pathway where it diverges from the acetate pathway as previously postulated.[18] The enhancement of C_2 intermediates such as this with a thick catalyst layer is postulated to be the main driving factor for its generation.

The two pathways presented here are not so different than what occurs in enzymatic catalytic pockets, where an electron rich amine couples with an electron poor carbon[12-14] and one can imagine that generating on-surface catalytic pockets in a synthetic system to promote this reaction would lead to further enhancements of electrosynthetic selectivity. As the nucleophilic attach is by the ammonia nitrogen is a thermodynamically downhill step, reduction potential for both of these reactions is still dictated by that necessary to reduce CO_2.

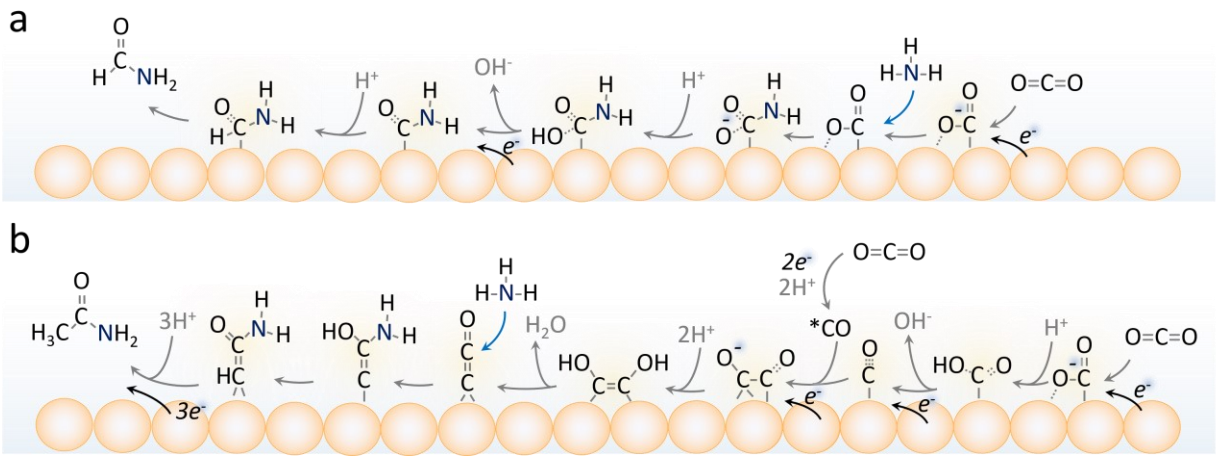

Figure 3.7 - Plausible surface reaction pathways in the electrosynthetic process of formamide (a) and acetamide (b) generation. Formamide generation depends on NH_3 coupling with the first reaction intermediate while acetamide generation requires highly reduced C_2 intermediates to be present on the catalyst surface. For simplicity, the donation of a proton to surface intermediates via $H_2O \rightarrow OH^-$ is depicted as $\rightarrow H^+$.

3.5 Concluding Remarks

While two new reaction pathways have been discovered in formamide and acetamide electrosynthesis using CO_2 and NH_3 building blocks, many avenues are now opened for further understanding and improving the efficiency of these reactions. First, while we used commercially purchased Cu and CuO nanoparticles as a readily available model system, they feature a diversity of active sites, defects, (sub)surface oxygen species, and exposed crystallographic facets. It is entirely possible that each of these factors may influence the reaction like they do in the electrosynthesis of carbon-based products via CO_2 reduction. A rational way forward would be the precise study of well-defined copper catalysts in which the nature surface-active sites are known and with complementary theoretical modelling of likely reaction pathways on these surfaces. Further, it is not known if Cu is the only catalyst capable of carrying out this reaction and if formate-selective metals like Sn and Bi would thus be more effective at formamide synthesis. In addition, we have developed an *operando* infrared spectroscopic method for the first time that was used to help understand this reaction pathway but additional complementary techniques such as Raman and X-ray absorption would contribute immensely valuable pieces to this puzzle.[40]

This principal significance to this work is the electrosynthetic reaction discovery which we envision will accelerate the adoption of this methodology at large in both the academic and industrial domains. While NH_3 is used as the model nitrogen source and nitrate and nitrite as further examples, eventually, this may be replaced by N_2 in a fully sustainable nitrogen cycle. In general, the capacity to drive heteroatomic surface coupling reactions with renewable-electricity powered systems stands to open up an abundance of decentralized green synthetic routes in place of heavy-infrastructure requiring fossil fuel based thermochemical approaches. In parallel,

there is much more fundamental chemistry to be discovered through the use of new interfaces, spectroscopic methodology, and catalytic systems.

Acknowledgements:

N.K. and J.L acknowledge NSERC Discovery Grant RGPIN-2019-05927

Author Contributions:

N.K and J.L both designed the project, carried out experiments, processed data, contributed intellectual insights and wrote the manuscript.

Competing Interests:

None to declare.

3.6 References:

1. J. Masa, C. Andronescu and W. Schuhmann, *Angew. Chem. Int. Ed.*, 2020, **59**, 15298-15312.
2. P. De Luna, C. Hahn, D. Higgins, S. A. Jaffer, T. F. Jaramillo and E. H. Sargent, *Science*, 2019, **364**, eaav3506.
3. M. Wang, M. A. Khan, I. Mohsin, J. Wicks, A. H. Ip, K. Z. Sumon, C.-T. Dinh, E. H. Sargent, I. D. Gates and M. G. Kibria, *Energy Environ. Sci.*, 2021, DOI: 10.1039/D0EE03808C.
4. Y. Zhang, J. Li and N. Kornienko, *Cell Rep. Phys. Sci.*, 2021, **2**, 100682.
5. J. Kibsgaard and I. Chorkendorff, *Nat. Energy*, 2019, **4**, 430-433.
6. M. B. Ross, P. De Luna, Y. Li, C.-T. Dinh, D. Kim, P. Yang and E. H. Sargent, *Nat. Catal.*, 2019, **2**, 648-658.
7. Z. J. Schiffer and K. Manthiram, *Joule*, 2017, **1**, 10-14.
8. O. I. Afanasyev, E. Kuchuk, D. L. Usanov and D. Chusov, *Chemical Reviews*, 2019, **119**, 11857-11911.
9. J. R. Dunetz, J. Magano and G. A. Weisenburger, *Org. Process Res. Dev.*, 2016, **20**, 140-177.
10. X. Guo, A. Facchetti and T. J. Marks, *Chemical Reviews*, 2014, **114**, 8943-9021.
11. M. Höhne and U. T. Bornscheuer, *ChemCatChem*, 2009, **1**, 42-51.
12. M. D. Patil, G. Grogan, A. Bommarius and H. Yun, *ACS Catal.*, 2018, **8**, 10985-11015.
13. O. Mayol, K. Bastard, L. Beloti, A. Frese, J. P. Turkenburg, J.-L. Petit, A. Mariage, A. Debard, V. Pellouin, A. Perret, V. de Berardinis, A. Zaparucha, G. Grogan and C. Vergne-Vaxelaire, *Nat. Catal.*, 2019, **2**, 324-333.

14. G. A. Aleku, S. P. France, H. Man, J. Mangas-Sanchez, S. L. Montgomery, M. Sharma, F. Leipold, S. Hussain, G. Grogan and N. J. Turner, *Nat. Chem.*, 2017, **9**, 961-969.
15. H. Kim and S. Chang, *ACS Catal.*, 2016, **6**, 2341-2351.
16. J. E. Kim, S. Choi, M. Balamurugan, J. H. Jang and K. T. Nam, *Trends Chem.*, 2020, **2**, 1004-1019.
17. C. Chen, X. Zhu, X. Wen, Y. Zhou, L. Zhou, H. Li, L. Tao, Q. Li, S. Du, T. Liu, D. Yan, C. Xie, Y. Zou, Y. Wang, R. Chen, J. Huo, Y. Li, J. Cheng, H. Su, X. Zhao, W. Cheng, Q. Liu, H. Lin, J. Luo, J. Chen, M. Dong, K. Cheng, C. Li and S. Wang, *Nat. Chem.*, 2020, **12**, 717-724.
18. M. Jouny, J.-J. Lv, T. Cheng, B. H. Ko, J.-J. Zhu, W. A. Goddard and F. Jiao, *Nat. Chem.*, 2019, **11**, 846-851.
19. N. Meng, Y. Huang, Y. Liu, Y. Yu and B. Zhang, *Cell Rep. Phys. Sci.*, 2021, **2**, 100378.
20. Y. Feng, H. Yang, Y. Zhang, X. Huang, L. Li, T. Cheng and Q. Shao, *Nano Lett.*, 2020, **20**, 8282-8289.
21. J. J. Roylance and K.-S. Choi, *Green Chem.*, 2016, **18**, 5412-5417.
22. M. Shibata, K. Yoshida and N. Furuya, *J. Electrochem. Soc.*, 1998, **145**, 2348-2353.
23. T. Fukushima and M. Yamauchi, *Chem. Commun.*, 2019, **55**, 14721-14724.
24. S. Nitopi, E. Bertheussen, S. B. Scott, X. Liu, A. K. Engstfeld, S. Horch, B. Seger, I. E. L. Stephens, K. Chan, C. Hahn, J. K. Nørskov, T. F. Jaramillo and I. Chorkendorff, *Chemical Reviews*, 2019, **119**, 7610-7672.
25. D. Higgins, C. Hahn, C. Xiang, T. F. Jaramillo and A. Z. Weber, *ACS Energy Lett.*, 2019, **4**, 317-324.
26. F. P. García de Arquer, C.-T. Dinh, A. Ozden, J. Wicks, C. McCallum, A. R. Kirmani, D.-H. Nam, C. Gabardo, A. Seifitokaldani, X. Wang, Y. C. Li, F. Li, J. Edwards, L. J. Richter, S. J. Thorpe, D. Sinton and E. H. Sargent, *Science*, 2020, **367**, 661-666.
27. S. L. Foster, S. I. P. Bakovic, R. D. Duda, S. Maheshwari, R. D. Milton, S. D. Minteer, M. J. Janik, J. N. Renner and L. F. Greenlee, *Nat. Catal.*, 2018, **1**, 490-500.
28. D. Liu, M. Chen, X. Du, H. Ai, K. H. Lo, S. Wang, S. Chen, G. Xing, X. Wang and H. Pan, *Adv. Func. Mater.*, 2021, **31**, 2008983.
29. N. Heidary, K. H. Ly and N. Kornienko, *Nano Lett.*, 2019, **19**, 4817-4826.
30. F. Milella and M. Mazzotti, *React. Chem. Eng.*, 2019, **4**, 1284-1302.
31. R. Kas, O. Ayemoba, N. J. Firet, J. Middelkoop, W. A. Smith and A. Cuesta, *ChemPhysChem*, 2019, **20**, 2904-2925.
32. X. Lu, C. Zhu, Z. Wu, J. Xuan, J. S. Francisco and H. Wang, *J. Am. Chem. Sci.*, 2020, **142**, 15438-15444.
33. P. P. Sethna, H. D. Downing, L. W. Pinkley and D. Williams, *J. Opt. Soc. Am.*, 1978, **68**, 429-431.
34. M. F. Baruch, J. E. Pander, J. L. White and A. B. Bocarsly, *ACS Catal.*, 2015, **5**, 3148-3156.
35. N. J. Firet and W. A. Smith, *ACS Catal.*, 2017, **7**, 606-612.

36. S. Zhu, B. Jiang, W.-B. Cai and M. Shao, *J. Am. Chem. Sci.*, 2017, **139**, 15664-15667.

37. I. V. Chernyshova, P. Somasundaran and S. Ponnurangam, *Proc. Natl. Acad. Sci. U.S.A.*, 2018, **115**, E9261.

38. E. Garand, T. Wende, D. J. Goebbert, R. Bergmann, G. Meijer, D. M. Neumark and K. R. Asmis, *J. Am. Chem. Sci.*, 2010, **132**, 849-856.

39. J. Resasco, L. D. Chen, E. Clark, C. Tsai, C. Hahn, T. F. Jaramillo, K. Chan and A. T. Bell, *J. Am. Chem. Sci.*, 2017, **139**, 11277-11287.

40. Y. Zhu, J. Wang, H. Chu, Y.-C. Chu and H. M. Chen, *ACS Energy Lett.*, 2020, **5**, 1281-1291.

Chapitre 4 – Electrochemical Formation of C-S Bonds from CO_2 and Small Molecule Sulfur Species

4.1 Résumé

La formation de liaisons C-S est une étape importante dans la synthèse de produits pharmaceutiques, biologiques et chimiques. Une voie verte très attrayante vers des espèces contenant des liaisons C-S serait celle conduite par électrocatalyse en utilisant d'abondants précurseurs de petites molécules, mais les exemples dans ce contexte sont largement absents de la littérature. À cette fin, ce travail démontre l'utilisation du CO_2 et du SO_3^{2-} comme blocs de construction bon marché qui couplent en surface des catalyseurs hétérogènes à base de Cu pour former pour la première fois de l'hydroxyméthanesulfonate, du sulfoacétate et du méthanesulfonate, avec des rendements faradiques allant jusqu'à 6,8 %. Une combinaison de mesures d'opérandes et de modélisation informatique révèle que *CHOH formé sur du Cu métallique est un intermédiaire électrophile clé qui est attaqué de manière nucléophile par SO_3^{2-} lors de l'étape principale de formation de la liaison C-S. Dans l'ensemble, la preuve de concept pour la formation de liaisons C-S électrocatalytiques et les connaissances mécanistes acquises devraient considérablement élargir la portée du domaine émergent de l'électrosynthèse.

Contribution : **Nikolay Kornienko, Junnan Li**, and Daniel Chartrand carried out electrochemical and operando studies. Hasan Al-Mahayni and Ali Seifitokaldani carried out computational work. All authors contributed to analysis and to the manuscript.

Electrochemical Formation of C-S Bonds from CO_2 and Small Molecule Sulfur Species

Junnan Li,[a,1] Hasan Al-Mahayni,[b,1] Daniel Chartrand,[a] Ali Seifitokaldani,[b] and Nikolay Kornienko[a*]*

1 Equal contribution

a Department of Chemistry, Université de Montréal, 1375 Ave. Thérèse-Lavoie-Roux, Montréal, QC H2V 0B3

b Department of Chemical Engineering, McGill University, 3610 University Street, Montréal, H3A 0C5 Québec, Canada

*Correspondence to: ali.seifitokaldani@mcgill.ca and nikolay.kornienko@umontreal.ca

Published: 27 April, 2023

DOI: /doi.org/10.1038/s44160-023-00303-9

4.2 Abstract

The formation of C-S bonds is an important step in the synthesis of pharmaceutical, biological, and chemical products. Electrocatalysis using abundant small molecule precursors is an attractive and green route to C-S bond containing species but examples within this context are largely absent from the literature. To this end, this work demonstrates the use of CO_2 and SO_3^{2-} as cheap building blocks which couple on the surface Cu-based heterogeneous catalysts. Hydroxymethanesulfonate, sulfoacetate and methanesulfonate are formed, with Faradaic efficiencies of up to 6.8%. A combination of operando measurements and computational modelling reveal that the *CHOH intermediate formed on metallic Cu is a key electrophilic species which is nucleophilically attacked by SO_3^{2-} in the principal C-S bond forming step. The proof-of-concept for electrocatalytic C-S bond formation and mechanistic insights gained will broaden the scope of the emerging field of electrosynthesis.

4.3 Introduction

Considering the ever-growing consequences of fossil fuel consumption, the development of green, low-emitting technologies like electrosynthesis is becoming increasingly important. Previous work in this field has focused on water electrolysis[1] to produce H_2 as an energy vector and chemical feedstock as well as CO_2 reduction[2,3] to generate carbon-based fuels and commodity chemicals. However, these two classes of reactions do not fully meet the needs of society and the chemical industry. Therefore, a recent push in the field of electrocatalysis has been to expand the scope of products that can be generated from abundant building blocks[4] and this includes directions such as H_2O_2 electrosynthesis from water and O_2,[5] N_2 reduction for NH_3 production,[6] and the formation of products with C-N bonds.[7]

Despite sulfur's abundance on earth and the importance of molecules with C-S bonds in biology,[8,9] pharmaceuticals,[10] agriculture,[11] battery technologies[12] and optoelectronic materials,[13] the bottom-up electrosynthesis of C-S bonds remains unexplored. Though the organic chemistry of C-S bond formation is established with strategies such as Diels-Alder reactions,[14] allylic or methane sulfonation[15,16] and sulfa-Michael addition[17], they face limitations of complex synthetic methodology, toxic byproducts and solvents and scalability limits thus hampering their

sustainable implementation in the chemicals industry. Renewable energy-driven routes have therefore begun to be explored. For example, photochemical C-S bond formation can be attained with carbon nitride photocatalysts in which C-S coupling occurs through radical-based routes[18] or through the addition of H_2S onto C=N bonds.[19] Methane sulfonation under high pressure conditions, presumably through radical-based C-S coupling in the electrolyte, is also being explored.[20] However, direct electrochemical C-S bond coupling under ambient conditions using starting reactants like CO_2, is yet to be realized.

Recently, we, and others in the field has shown the capacity for electrochemical C-N bond generation using CO_2 and small molecule N-sources (such as N_2, NO_3^-, NO_2^- and NH_3).[21-24] These reactions primarily proceed through the reduction of CO_2 to form an activated electrophilic intermediate and subsequent coupling with a (near-)surface N-containing nucleophile. This extension of traditional electrochemical routes enabled the build-up of higher-value, complex products than those simply available through CO_2 reduction. With this in mind, we hypothesized that C-S coupling should also be possible through a similar pathway as sulfur and nitrogen should have similar properties from the diagonal relationships found within the periodic table.[25] Thus, we moved to translate our methodology to C-S bond formation in a similar reaction setup. As a starting point, we used Cu-based catalysts[26] as a model system to generate activated electrophilic intermediates from CO_2 and $NaSO_3$ as a representative S-based nucleophile (Fig. 1). In doing so, we established reaction pathways to hydroxymethane sulfonate (HMS), sulfoacetate (SA) and methane sulfonate (MS) products via electrochemical C-S coupling with up to 6.8% Faradaic efficiency (FE).

SO_3^{2-} naturally forms in minerals in the environment, is produced as a byproduct in processes like sulfuric acid or thiosulfate manufacturing,[27] and is commonly used in wood pulping[28] or as a preservative.[29] Sulfonates made from the coupling of CO_2 and SO_3^{2-} in this work have use as cement additives and membrane components (SA),[30,31] electrolytes and agents in organic synthesis (MS),[32-34] and within various facets of the textile industry (HMS).[35] In all, the sulfonate additives market is valued at 6 billion USD with primary applications as lubricants and detergents,[36] and as an example, MS has a market of 700 million USD with applications in electroplating, pharmaceuticals and esterification.[37]

To investigate the reaction pathway and extract out mechanistic insights translatable to future works, we carried out a combination of *operando* and computation modelling which pointed to *CHOH coupling to SO_3^{2-} as a likely rate-limiting step. Crucially, this work introduces C-S bond formation in an expansion of the scope of sustainable electrosynthesis and opens potential avenues for C-S chemical production from abundant sources, powered via renewable electricity.

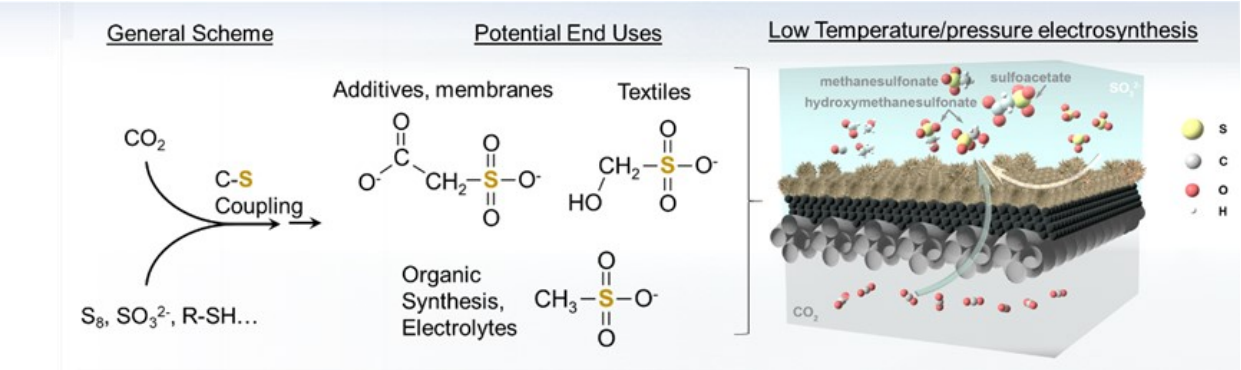

Figure 4.1 - End-use applications of C-S bond containing products with several representative molecules and illustration of electrochemical C-S bond formation from CO_2 and SO_3^{2-} building blocks.

4.4 Result and Discussion

4.4.1 Material synthesis and electrocatalysis

Cuprous oxide catalysts were synthesized via a simple room-temperature method (Fig. 8.1, 8.2).[38] A catalyst ink was then made from these materials and loaded onto a standard gas diffusion layer which was used as the working electrode in a modified gas-diffusion half-cell configuration (Fig. 8.3). In this setup, CO_2 was fed through the gas phase directly to the interface between the gas, catalyst and electrolyte, thereby promoting CO_2 reduction by circumventing its solubility limits and enabling the use of alkaline electrolyte (1 M KOH) which suppresses the competing hydrogen evolution reaction (HER). 200 mM SO_3^{2-} as the sulfur source was added directly to the aqueous electrolyte. Screening of possible products in the NMR spectra revealed that HMS, SA and MS were formed as $4e^-$, $6e^-$ and $6e^-$ products (Fig. 4.2a and 8.8).

While enabling C-S reaction pathways, the presence of sulfite decreased the total current density (Fig. 4.2b) and favored the production of liquid products from CO_2 reduction (Fig. 4.2c). Across the measured potential, the FE for detected C-S products ranged from 4.7-9.5% (Fig. 4.2d) and the partial current density for each only modestly increased with more negative potentials (Fig. 4.2e). This weak dependence on product formation with applied potential is potentially indicative of the sluggish kinetics of the reaction and the need for the SO_3^{2-} reactant to diffuse to the surface and find a suitable surface reaction intermediate to couple with.

The production of HMS, SA and MS from CO_2 and SO_3^{2-} represents three reaction pathways and opens up the possibility of building up a wide spectrum of S-C containing chemicals such as thiols, sulfonates and organic sulfides with simple electrochemical methods as an alternative to organic chemistry routes. HMS has been observed before from the nucleophilic attack of CH_2O (locally generated from CO) by SO_3^{2-} and in our case a similar coupling step may be in play.[39] SA and MS on the other hand, are tentatively thought to arise from a (near) surface SO_3^{2-} nucleophilic attack onto a C_2 intermediate in the methane or acetate pathway. There was no HMS, SA or MS formed in control experiments that omitted CO_2, SO_3^{2-}, the Cu catalyst or an applied bias (Fig. 8.11). Further, using commercially purchased Cu, Cu_2O, CuO or synthesized Cu_2O with other morphologies resulted in HMS and SA formation with lower, but comparable FEs (Fig. 8.10, 8.18), indicating that the C-S bond pathway is generalizable on a variety of Cu-based materials. In contrast, Ag particles which produce CO as the main CO_2 reduction product, did not show any detectable C-S products (Fig. 8.19), indicating the need for the catalyst to produce and stabilize further reduced intermediates than CO. Further, copper sulfide catalysts could not produce C-S products in the absence of SO_3^{2-}, and with SO_3^{2-} were less active than the oxide-derived materials (Fig. 8.20). When SO_3^{2-} was omitted from the electrolyte, methane was a dominant product (Fig. 8.21). This may indicate that the route to C-S products shares a similar pathway to methane formation and thus intercepts the intermediates before they are reduced to methane, or that the presence of near-surface SO_3^{2-} alters the reaction route to minimize the methane pathway. Post-reaction analysis (after 1 hr at -0.68 V) indicates that the catalysts are largely reduced to the metallic state and restructure to smoother morphologies (Fig. 8.23-26), likely leaving the low energy facets of Cu exposed.

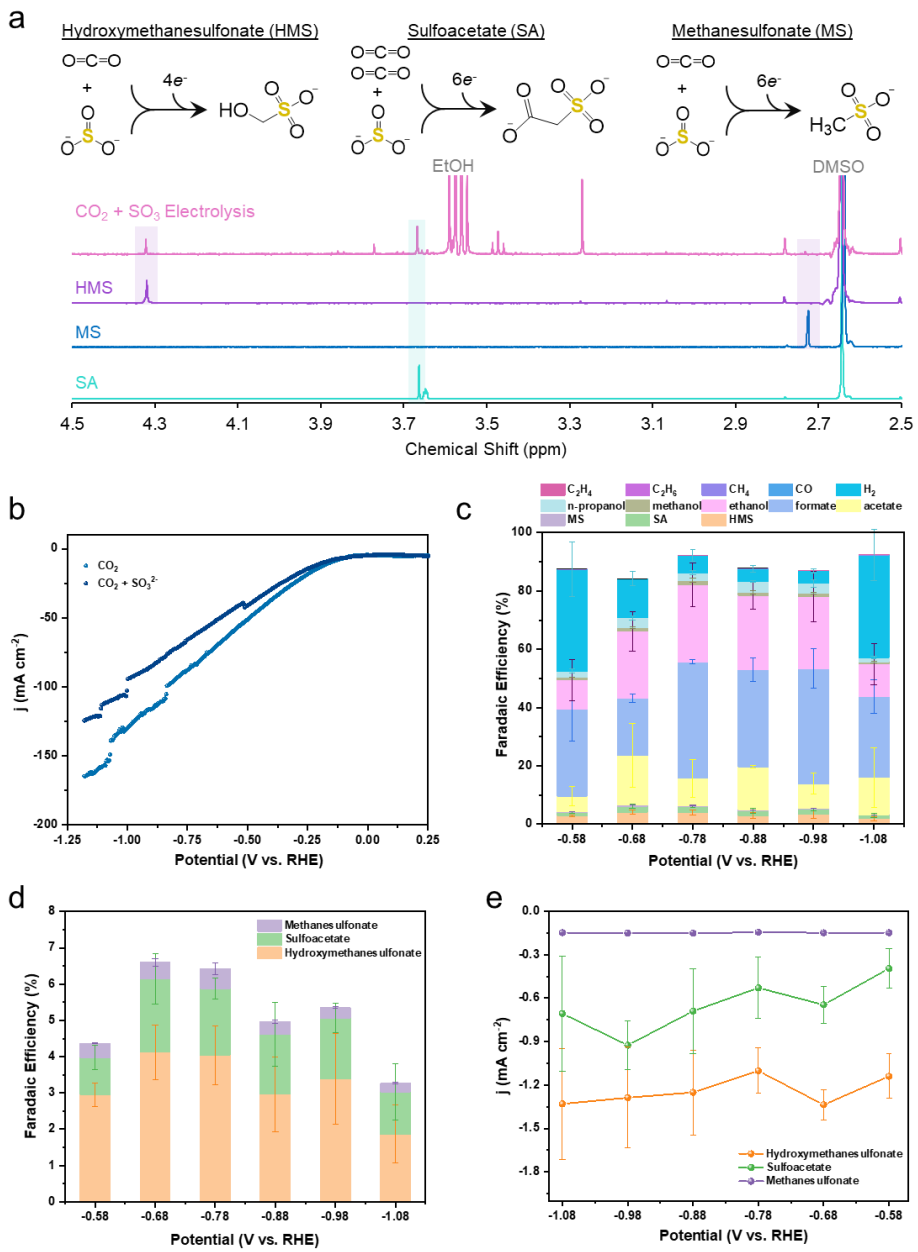

Figure 4.2 - Identification and structure of HMS, MS and SA products constructed from CO_2 and SO_3^{2-} (a). The presence of 200 mM SO_3^{2-} decreases the overall current density (b) and pushes the selectivity towards liquid products (c). In all, C-S products are formed with up to 9.5% FE (d) with only a weak dependence of their formation rates on the applied potential (e).

4.4.2 Mechanistic Investigations

We next moved to carry out a round of experimental mechanistic studies to gain an initial insight into the dynamics of the electrosynthetic system. The faceted Cu_2O starting material loses its well-defined structure during electrocatalysis under reductive potentials, as evident from transmission electron microscope (TEM) images (Fig. 4.3a). Translating the setup to a powder x-ray diffraction (XRD) instrument, enabled us to visualize changes in crystallinity immediately after applying a reducing potential.[40,41] Indeed, the Cu_2O peaks disappear within 4 minutes after shifting from open circuit conditions to -0.68 V_{RHE} and only Cu peak stemming from metallic Cu remains (Fig. 4.3b). This indicates that while an oxide is the starting material, the main phase of the catalyst under working conditions is indeed metallic Cu, though sub-surface oxygen or defects induced by the structural change could certainly be present and affecting the catalytic process.

Raman spectroscopywas subsequently utilized to capture the reaction intermediates on the Cu surface under equivalent reaction conditions (Fig. 4.3c).[42] While the assignment of each peak is not entirely unambiguous, we base our interpretation on previously established works.[43-48] As the potentially was systematically shifted negatively from open circuit conditions, Cu_2O bands (220 and 417-670 cm^{-1}) diminished, pointing to the transition to metallic Cu by -0.58V_{RHE}. At the same time, the Cu-CO band (369 cm^{-1}) appeared starting at -0.58V_{RHE}. Similarly, weak features potentially stemming from $*CO_{bridge}$ (1850-1900 cm^{-1}, 0.42 to -0.18 V_{RHE}) were noted (Fig. 8.31). In addition to CO, $*CO_2^-$ (700 cm^{-1}), SO_3^{2-} (983 cm^{-1}), HCO_3^- (1022 cm^{-1}) and CO_3^{2-} (1069 cm^{-1}) were identified as (near) surface species. These bands, with the exception of SO_3^{2-}, were similarly detected during electrolysis with CO_2 only. Finally, a set of bands at 700, 1331-1371, and 1580-1620 cm^{-1} arose under reductive potentials. While there is debate as to their exact identity, previous works have attributed them to $*COO^-$ or *COOH species and this is our tentative assignment (Fig. 8.31).[43,44,49,50]

Overall, the above experiments show that most oxide-like features disappeared from the catalyst under operating conditions, SO_3^{2-} was continually present as a (near)surface species, and CO and CO_2^- were the primary reaction intermediates on the Cu surface. Thus, CO is a likely principal intermediate in the reaction pathways towards higher order products. Given that the measured quantities of CO were very low, it is likely that all of the detected *CO reacted further on the

catalyst surface via hydrogenation or C-C coupling. Hydrogenation would occur en route to CH_4 production while a combination of C-C coupling and hydrogenation would terminate in the observed ethanol and acetate in our system. Because CH_4 is the primary product that is suppressed in the presence of SO_3^{2-}, it would be reasonable to assume that a partially hydrogenated *CO (such as *CHO or CH_2O) in the CH_4 pathway may be the main species coupling with SO_3^{2-} en route to HMS formation. The Raman and XRD experiments further point to Cu as the main phase during catalysis rather than oxide or sulfide phases of Cu that were not detected within the limits of our experimental sensitivity. This is further substantiated by post-electrolysis energy dispersive spectroscopy (EDS) measurements, in which S is either absent or only detected in very small quantities (Fig. 8.26). The decrease in current upon addition of SO_3^{2-} to the electrolyte (Fig. 4.2b and 8.9), as well as lack of significant SO_3^{2-} reduction on the Cu surface seen through Raman studies (Fig. 8.32-33) points to the role of SO_3^{2-} as a spectator species prior to a possible coupling step with a CO_2 reduction intermediate.

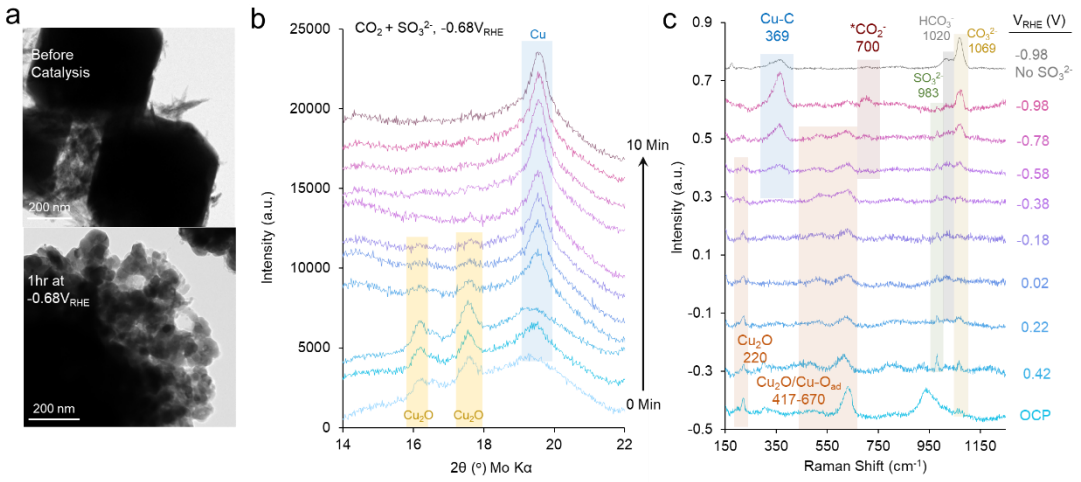

Figure 4.3 - TEM imaging illustrates morphological changes during the catalytic cycle (a) while the changes in crystallinity are probed during the reaction with *operando* XRD measurements (b). Similarly, *operando* Raman experiments capture surface-bound intermediates en route to CO_2 and SO_3^{2-} coupling.

4.4.3 Theoretical Modelling

A complementary investigation into the mechanism for heterogeneous C-S bond formation was performed with density functional theory (DFT) computations using the results from electrocatalytic and spectroscopic experiments as a starting point. Here, three slab structures for copper (100), (110) and (111) were constructed as the model catalyst to simulate the reaction pathway. Further computational details are given in the SI and elsewhere.[51] Based on the observations in figures 4.2 and 4.3, CO was used as a starting intermediate as it is featured in the CO_2 reduction pathway to higher order products.

To compute energy differences of elementary proton coupled electron transfer (PCET) steps, the computational hydrogen electrode (CHE) model[52] was used. Since explicit negative charge(s) was added to the simulation for SO_3^{2-} and HSO_3^-, to calculate the energy difference of the adsorption step and coupling step, the following equations were used, respectively:

$$SO_3^{2-} + * \rightarrow {}^*SO_3 + 2e^-;\ \Delta E_{ads} = E_{{}^*SO_3} + 2eV - E_{SO_3^{2-}} - E_* \quad \text{(Rx1)}$$

$$SO_3^{2-} + {}^*CO \rightarrow {}^*SO_3CO + 2e^-;\ \Delta E_{coupling} = E_{{}^*SO_3CO} + 2eV - E_{SO_3^{2-}} - E_{{}^*CO} \quad \text{(Rx2)}$$

$${}^*SO_3 + {}^*CO \rightarrow {}^*SO_3CO;\ \Delta E_{coupling} = E_{{}^*SO_3CO} - E_{{}^*SO_3} - E_{{}^*CO} \quad \text{(Rx3)}$$

$$HSO_3^- + * \rightarrow {}^*HSO_3 + e^-;\ \Delta E_{ads} = E_{{}^*HSO_3} + eV - E_{HSO_3^-} - E_* \quad \text{(Rx4)}$$

$$HSO_3^- + {}^*CO \rightarrow {}^* HSO_3CO + e^-;\ \Delta E_{coupling} = E_{HSO_3CO} + eV - E_{HSO_3^-} - E_{{}^*CO} \quad \text{(Rx5)}$$

$${}^*HSO_3 + {}^*CO \rightarrow {}^* HSO_3CO\ ;\ \Delta E_{coupling} = E_{HSO_3CO} - E_{{}^*HSO_3} - E_{{}^*CO} \quad \text{(Rx6)}$$

To compute the energy differences for multiple reaction pathways, the basic CORR mechanisms are considered:

$$CO \longrightarrow {}^*CO \longrightarrow {}^*COH \longrightarrow {}^*C \longrightarrow {}^*CH \longrightarrow {}^*CH_2 \longrightarrow {}^*CH_3 \longrightarrow CH_4 \quad \text{(Rx7)}$$

$$CO \longrightarrow {}^*CO \longrightarrow {}^*CHO \longrightarrow {}^*CHOH\ , {}^*CH_2O \longrightarrow {}^*CH_2OH \longrightarrow CH_3OH \quad \text{(Rx8)}$$

All steps except the first adsorption are PCET steps. The intermediates investigated that can couple with SO_3^{2-} or HSO_3^- are CO, COH, CHO, CHOH, CH_2O and CH_2OH. In Rx7, the intermediates following COH were not considered since formation of COH is unfavourable at 0.6 eV on Cu (100), as shown in Fig. 4. However, COH coupling with SO_3^{2-} was still considered since COH is believed to be an intermediate to methane production. For Rx8, CHO, CHOH, CH_2O and CH_2OH were coupled with SO_3^{2-} to create the C-S bond.

The final product considered in DFT calculations was HMS as seen in Fig. 4.2 as it is the primary C-S product in the electrolysis experiments. In solution, SO_3^{2-} or HSO_3^- can exist depending on the *pH* of the electrolyte. Thus, both compounds are tested for the nucleophilic attack. Furthermore, at any point during protonation, one of the oxygens attached to the sulfur can be protonated to yield -RSO_2OH. All of the aforementioned pathways are considered and this is illustrated in Fig. S34, 35.

Two mechanisms are investigated for the C-S coupling step: (*i*) a nucleophilic attack of either SO_3^{2-} (Rx2) or HSO_3^- (Rx4) on the carbon of an adsorbed intermediate; and (*ii*) surface coupling of an adsorbed $^*SO_3$ (Rx1 and Rx3) or $^*HSO_3$ (Rx4 and Rx6) with the carbon of an adsorbed intermediate.

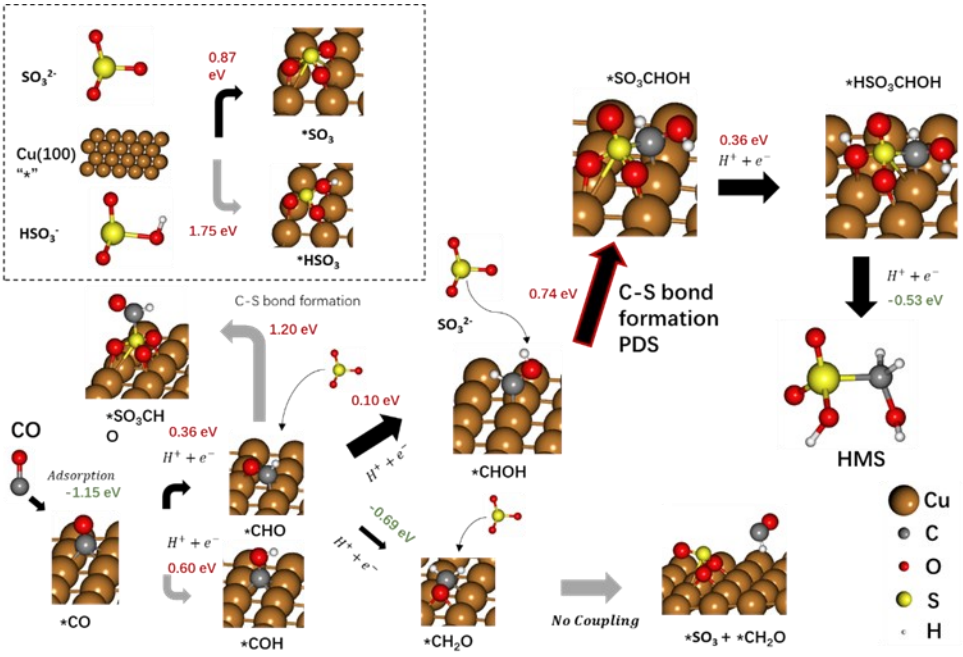

Figure 4.4 - Reaction pathway from CO to HMS. Red numbers are positive energy barriers (uphill) while green numbers are negative (downhill).

Adsorption energy calculations of S species on all three copper facets (Table 8.2) reveal that: (*i*) SO_3^{2-} is adsorbed more favourably than HSO_3^-. This is mostly because SO_3^{2-} species has 2 negative charges and is relatively smaller than HSO_3^-, making it easier to bond with copper atoms (Fig. 4.4); (*ii*) Both S species are adsorbed more strongly on the (110) facet, followed by (100) then (111) facets, as seen on Table 8.2. Accordingly, the rest of the simulations to calculate the reaction energy diagram are performed only on (110) and (100) facets.

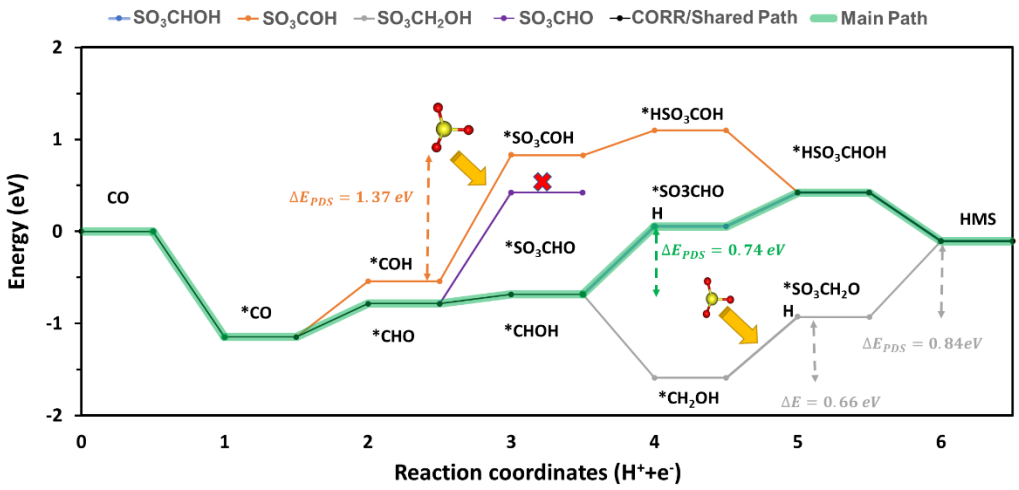

Figure 4.5 - Energy diagram on Cu (100). The blue curve is for C-S coupling with CHOH. The orange curve is for HSO_3COH. The grey curve is for SO_3CH_2OH. The black curve on the left is the shared CORR path while the black curve on the right represents intersecting paths. The green highlighted curve shows the most favourable path to HMS. All steps are electrochemical except the ones denoted with an SO_3^{2-} molecule and a yellow arrow. These denote a nucleophilic attack. The very first step corresponds to CO adsorption on the surface. No potential is applied to the system.

The (110) facet might perform the best as it interacts more strongly with S species compared to the other two surfaces. However, according to the Sabatier principle, the middle adsorption by (100) facet could render it the best performing as the adsorption is neither too weak (not able to hold the species on the surface for enough time to react with other reaction intermediates) nor

too strong (to avoid further interactions with other reaction intermediates). The reaction energy diagram is shown for the (100) facet on Fig. 4.5, and that for the (110) facet is demonstrated on Fig. 8.36.

The optimized energies for all the structures are provided in Table 8.3, 8.4. Through these DFT computations we seek: (*i*) to understand which reaction intermediates are involved in the C-S coupling step; (ii) to calculate the reaction energy barrier of the C-S coupling step; and (*iii*) to specify the best performing facet for the C-S bond formation. The optimal path is shown with thick black arrows on Fig. 4.4. The energy diagram comparing different C-S coupling steps is shown on Fig. 4.5. Coupling through SO_3^{2-} is more favourable than HSO_3^-, regardless of which intermediates are involved in the C-S coupling step and no matter what the copper surface is. Furthermore, due to the high adsorption energy of $^*SO_3$ on (100), surface coupling is deemed less likely than the nucleophilic attack of the species from the electrolyte. The optimal coupling step is found to be through *CHOH. The energy barrier of the C-S coupling step is 0.74 eV and is the potential determining step (PDS). Coupling through *COH has a large energy barrier of 1.37 eV. Surprisingly, coupling through *CH_2OH has an energy barrier of 0.66 eV, which is lower than *CHOH coupling. However, protonating the sulfur of SO_3CH_2OH has a barrier of 0.82 eV, making this path unfavourable. Comparing the energy barrier of the PDS to typical PDS's of CO_2RR, it is reasonable to observe that the maximal FE obtained in this study is ~10% since most thermodynamic energy barrier for the CO_2RR are lower than 0.74 eV. Lowering the energy barrier of the *CHOH coupling step is key to further increasing the FE in future studies.

The same methodology and calculations are applied to the (110) facet since it appears to have the lowest $^*SO_3$ adsorption energy. Figure 8.30 shows the energy diagram of the most favourable path on both (100) and (110). The most promising coupling path on (110) appears to be consistent with *CHOH coupling being the most favourable, as seen for (100). The coupling energy barrier, however, is only 0.11 eV. The largest subsequent protonation energy barrier is the protonation of sulfur in SO_3CHOH to HSO_3CHOH, at 0.29 eV (Fig. 8.35, 36). Thus, the PDS remains *CO hydrogenation to *CHO, a typical PDS for the CO_2RR. The DFT results show that (110) should be superior to (100) when it comes to C-S bond formation as seen in Figure 8.30 however our

experiments do not show that. This could be due to changes in size, surface reconstruction and other unaccounted-for effects. We encourage future studies to explore the Cu (110) facet further.

The C-S coupling mechanism here bears much similarity several aforementioned C-N coupling works. Amide,[53,54] amine,[23,55] and urea[56-58] synthetic routes also proceed through a nucleophilic attach of a nitrogen species (such as $*NH_2$, NH_3 or NH_2OH) onto an electrophilic CO_2 reduction intermediate (*CO, *CCO, $*CH_2O$). A difference here lies within the nucleophilicity of the C and N reactants, previously shown to play a determining role in coupling efficiency,[55] though both rely on stabilizing a partially reduced CO_2 reduction intermediate so it can undergo the coupling step. Further, other coupling steps in C-N bond formation like *NN* + *CO coupling[22,59] en route to urea formation are quite different in nature.

4.4.4 Expansion of scope

As a final step, we sought to expand the scope in terms of potential C-S coupling reactions. While the partial current densities for C-S products was rather modest when using CO_2 as the reactant, amounting to less than 5 mA/cm^2, we reasoned that potentially more active C-precursors that can be produced from CO_2 reduction would lead to enhanced rates (Fig. 4.6a). To this end, we maintained identical reaction conditions (-1.18V_{RHE}, 200 mM SO_3^{2-} in 1 M KOH) and substituted 200 mM of CH_3OH, $HCOO^-$, CH_2O or CH_3COO^- in place of CO_2. Indeed, we was that the formation of SA was greatly increased by up to 2 orders of magnitude for CH_3OH and by 30X for $HCOO^-$ (Fig. 4.6b). Note, no products were observed if SO_3^{2-} and the C-reactants were simply mixed in the electrolyte (Fig. 8.37). The equilibration with methanediol in alkaline media likely prevented formaldehyde from directly coupling with SO_3^{2-} through non-electrochemical steps. We chose to use formation rate as a metric of comparison as the precise mechanism and electron transfer steps are not yet unambiguous. This set of results indicates that a variety of partially reduced CO_2 products species may act as effective building blocks for C-C and C-S bond formation. Strategies for C-S product synthesis with increased rates could then entail the use of flow reactors utilize a CO_2 activation catalyst (e.g. Sn or Bi – based materials selective for $HCOO^-$) and a secondary C-S coupling catalyst (Cu in this work but other materials may yet be better). Interestingly, HMS was not observed in these experiments. Possible routes to SA formation are given in Fig. 8.39-41,

taking into account preliminary Raman experiments and previous studies of formate[60,61] and methanol[62-64] interactions with metallic surfaces.

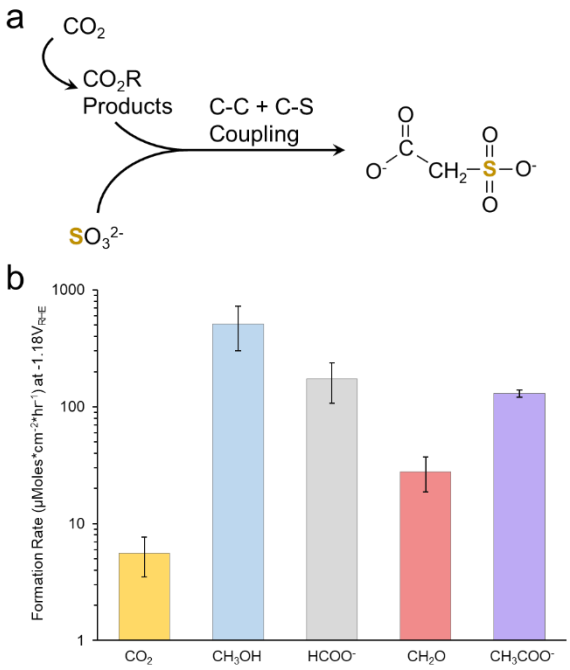

Figure 4.6 - Scheme of using partially reduced CO2 products as activated reagents for C-S bond formation (a). The formation rate of SA at -1.18VRHE is significantly enhanced when substituting 200 mM of C-reactant in place of CO2 (b).

4.5 Concluding Remarks

In summary, this work develops a C-S coupling pathway via heterogeneous electrocatalysis using CO_2 as a building block. Using Cu-based catalysts as a model system, we illustrate how CO_2 is reduced to surface-bound electrophilic intermediates like *CHOH, which are then subject to nucleophilic attack by near-surface SO_3^{2-} species, yielding three distinct C-S bond containing species. The expansion of scope of CO_2 reduction to include products with C-S bonds is set to grant electrocatalytic technologies access to not only fuels and commodity chemicals, but also to important sets of fine/specialty chemicals and widen the impact of this growing domain.

Moving ahead towards practical realization of C-S coupling there are several issues to be addressed. The initial iteration of this system operates in alkaline electrolytes, whose use can lead

CO_2 interconversion to carbonates and ultimately low CO_2 utilization efficiencies.[65] This can be alleviated by moving towards acidic electrolytes[66-68] or instituting CO_2 recovery strategies.[69] Further, increasing partial current density and FE is key towards realizing a commercially viable system, which is expected to come from the advancement of catalyst and electrolyzer design, underpinned by a fundamental understanding of the catalytic chemistry at play. Finally, the scope of C-S coupling can be further expanded beyond sulfonates, as thiols, sulfides, and other organosulfur compounds could potentially be generated through small molecule electrolysis.

Acknowledgements:

N.K. and J. L. acknowledge NSERC for its Discovery Grant RGPIN-2019-05927. A.S. acknowledges NSERC for its Discovery Grant RGPIN-2020-04960 and Canada Research Chair (950-23288). Computations in this research were enabled in part by support provided by Calcul Quebec and Compute Canada.

Declaration of Interests:

The authors declare no competing interests

Data Availability Statement:

All data will be deposited in Papyrus, a publicly accessible repository.

4.6 References:

1 Lagadec, M. F. & Grimaud, A. Water electrolysers with closed and open electrochemical systems. *Nat. Mater.* **19**, 1140-1150 (2020).

2 Ross, M. B., De Luna, P., Li, Y., Dinh, C.-T., Kim, D., Yang, P. & Sargent, E. H. Designing materials for electrochemical carbon dioxide recycling. *Nat. Catal.* **2**, 648-658 (2019).

3 Masel, R. I., Liu Z., Yang, H., Kaczur, J. J., Carrillo, D., Ren, S., Salvatore, D. & Berlinguette, C. P. An industrial perspective on catalysts for low-temperature CO2 electrolysis. *Nat. Nanotechnol.* **16**, 118-128 (2021).

4 Zhang, Y., Li, J. & Kornienko, N. Strategies for heterogeneous small-molecule electrosynthesis. *Cell Rep. Phys. Sci.* **2**, 100682 (2021).

5 Perry, S. C., Pangotra, D., Vieira, L., Csepei, L.-I., Sieber, V., Wang, L., De León, C. P. & Walsh, F. C.

Electrochemical synthesis of hydrogen peroxide from water and oxygen. *Nat. Rev. Chem.* **3**, 442-458 (2019).

6 Suryanto, B. H. R., Du, H.-L., Wang, D., Chen, J., Simonov A. N. & MacFarlane D. R. Challenges and prospects in the catalysis of electroreduction of nitrogen to ammonia. *Nat. Catal.* **2**, 290-296 (2019).

7 Li, J., Zhang, Y., Kuruvinashetti, K. & Kornienko, N. Construction of C–N bonds from small-molecule precursors through heterogeneous electrocatalysis. *Nat. Rev. Chem.* **6**, 303-319 (2022).

8 Fontecave, M., Ollagnier-de-Choudens, S. & Mulliez, E. Biological Radical Sulfur Insertion Reactions. *Chem. Rev.* **103**, 2149-2166 (2003).

9 Mansy, S. S. & Cowan, J. A. Iron–Sulfur Cluster Biosynthesis: Toward an Understanding of Cellular Machinery and Molecular Mechanism. *Acc. Chem. Res.* **37**, 719-725 (2004).

10 Zhao, C., Rakesh, K. P., Ravidar, L., Fang, W.-Y. & Qin, H.-L. Pharmaceutical and medicinal significance of sulfur (SVI)-Containing motifs for drug discovery: A critical review. *Eur. J. Med. Chem.* **162**, 679-734 (2019).

11 Devendar, P. & Yang, G.-F. in *Sulfur Chemistry* (ed Xuefeng Jiang) 35-78 (Springer International Publishing, 2019).

12 Rosenman, A., Markevich E., Salitra G., Aurbach D., Garsuch A., Chesneau F. F. Review on Li-Sulfur Battery Systems: an Integral Perspective. *Adv. Energy Mater.* **5**, 1500212 (2015).

13 Barbarella, G., Melucci, M. & Sotgiu, G. The Versatile Thiophene: An Overview of Recent Research on Thiophene-Based Materials. *Adv. Mater.* **17**, 1581-1593 (2005).

14 Sakakura, A., Yamada, H. & Ishihara, K. Enantioselective Diels–Alder Reaction of α-(Acylthio)acroleins: A New Entry to Sulfur-Containing Chiral Quaternary Carbons. *Org. Lett.* **14**, 2972-2975 (2012).

15 Wu, X.-S., Chen, Y., Li, M.-B., Zhou, M.-G. & Tian, S.-K. Direct Substitution of Primary Allylic Amines with Sulfinate Salts. *J. Am. Chem. Soc.* **134**, 14694-14697 (2012).

16 Mukhopadhyay, S. & Bell, A. T. Catalyzed sulfonation of methane to methanesulfonic acid. *J. Mol. Catal. A: Chem.* **211**, 59-65 (2004).

17 Uraguchi, D., Kinoshita, N., Nakashima, D. & Ooi, T. Chiral ionic Brønsted acid–achiral Brønsted base synergistic catalysis for asymmetric sulfa-Michael addition to nitroolefins. *Chem. Sci.* **3**, 3161-3164 (2012).

18 Savateev, A., Kurpil, B., Mishchenko, A., Zhang, G. & Antonietti, M. A "waiting" carbon nitride radical anion: a charge storage material and key intermediate in direct C–H thiolation of methylarenes using elemental sulfur as the "S"-source. *Chem. Sci.* **9**, 3584-3591 (2018).

19 Su, F., Mathew, S. C., Möhlmann, L., Antonietti, M., Wang, X., Blechert, S. Aerobic Oxidative Coupling

of Amines by Carbon Nitride Photocatalysis with Visible Light. *Angew. Chem. Int. Ed.* **50**, 657-660 (2011).

20 Britschgi, J., Kersten, W., Waldvogel, S. R. & Schüth, F. Electrochemically Initiated Synthesis of Methanesulfonic Acid. *Angew. Chem. Int. Ed.* **61**, e202209591 (2022).

21 Li, J. & Kornienko, N. Electrochemically driven C–N bond formation from CO2 and ammonia at the triple-phase boundary. *Chem. Sci.* **13**, 3957-3964 (2022).

22 Chen, C., Zhu, X., Wen, X., Zhou, Y., Zhou, L., Li, H., Tao, L., Li, Q., Du, S., Liu, T., Yan, D., Xie, C., Zou, Y., Wang, Y., Chen, R., Huo, J., Li Y., Cheng, J., Su, H., Zhao, X., Cheng, W., Liu, Q., Lin, H., Luo, J., Chen, J., Dong, M., Cheng, K., Li, C. & Wang, S. Coupling N_2 and CO_2 in H_2O to synthesize urea under ambient conditions. *Nat. Chem.* **12**, 717-724 (2020).

23 Wu, Y., Jiang, Z., Lin, Z., Liang, Y. & Wang, H. Direct electrosynthesis of methylamine from carbon dioxide and nitrate. *Nat. Sustainability* **4**, 725-730 (2021).

24 Meng, N., Huang, Y., Liu, Y., Yu, Y. & Zhang, B. Electrosynthesis of urea from nitrite and CO2 over oxygen vacancy-rich ZnO porous nanosheets. *Cell Rep. Phys. Sci.* **2**, 100378 (2021).

25 Rayner-Canham, G. Isodiagonality in the periodic table. *Found. Chem.* **13**, 121-129 (2011).

26 Nitopi, S., Bertheussen E., Scott S. B., Liu X., Engstfeld A. K., Horch S., Seger B., Stephens I. E. L., Chan K., Hahn C., Nørskov J. K., Jaramillo T. F., & Chorkendorff I. Progress and Perspectives of Electrochemical CO2 Reduction on Copper in Aqueous Electrolyte. *Chem. Rev.* **119**, 7610-7672 (2019).

27 Barberá, J. J., Metzger, A. & Wolf, M. in *Ullmann's Encyclopedia of Industrial Chemistry* (2000).

28 Fatehi, P. & Ni, Y. in *Sustainable Production of Fuels, Chemicals, and Fibers from Forest Biomass* Vol. 1067 *ACS Symposium Series* Ch. 16, 409-441 (American Chemical Society, 2011).

29 Taylor, S. L., Higley, N. A. & Bush, R. K. in *Advances in Food Research* Vol. 30 (eds C. O. Chichester, E. M. Mrak, & B. S. Schweigert) 1-76 (Academic Press, 1986).

30 Nascimento, B., Filho G. R., Frigoni E. S., Soares H. M., Meireles C. S., Cerqueira D. A., Valente A. J. M., Carvalho R. A., De Assunção R. M. N., De Castro Motta L. A. Application of cellulose sulfoacetate obtained from sugarcane bagasse as an additive in mortars. *J. App. Polym. Sci.* **124**, 510-517 (2012).

31 Seeponkai, N. & Wootthikanokkhan, J. Proton conductivity and methanol permeability of sulfonated poly(vinyl alcohol) membranes modified by using sulfoacetic acid and poly(acrylic acid). *J. App. Polym. Sci.* **105**, 838-845 (2007).

32 D. Gernon, M., Wu, M., Buszta, T. & Janney, P. Environmental benefits of methanesulfonic acid . Comparative properties and advantages. *Green Chem.* **1**, 127-140 (1999).

33 Balaji, R. & Pushpavanam, M. Methanesulphonic acid in electroplating related metal finishing industries.

Trans. IMF **81**, 154-158 (2003).

34 Nacsa, E. D. & Lambert, T. H. Cyclopropenone Catalyzed Substitution of Alcohols with Mesylate Ion. *Org. Lett.* **15**, 38-41 (2013).

35 V. Makarov, S. Recent trends in the chemistry of sulfur-containing reducing agents. *Russ. Chem. Rev.* **70**, 885-895 (2001).

36 Sulphonate Additives Market. (Fact.MR, 2022).

37 Methane Sulfonic Acid Market. (Market Research Future, 2023).

38 Ho, J.-Y. & Huang, M. H. Synthesis of Submicrometer-Sized Cu2O Crystals with Morphological Evolution from Cubic to Hexapod Structures and Their Comparative Photocatalytic Activity. *J. Phys. Chem. C* **113**, 14159-14164 (2009).

39 Boutin, E., Salamé, A., Merakeb, L., Chatterjee, T. & Robert, M. On the Existence and Role of Formaldehyde During Aqueous Electrochemical Reduction of Carbon Monoxide to Methanol by Cobalt Phthalocyanine. *Chem. Eur. J* **28**, e202200697 (2022).

40 Scott, S. B., Hogg T. V., Landers A. T., Maagaard T., Bertheussen E., Lin J. C., Davis R. C., Beeman J. W., Higgins D., Drisdell W. S., Hahn C., Mehta A., Seger B., Jaramillo T. F. & Chorkendorff I. Absence of Oxidized Phases in Cu under CO Reduction Conditions. *ACS Energy Letters* **4**, 803-804 (2019).

41 Yang, S., Liu Z., An H., Arnouts S., De Ruiter J., Rollier F., Bals S., Altantzis T., Figueiredo M. C., Filot I. A.W., Hensen E. J.M., Weckhuysen B. M. & Stam W. Near-Unity Electrochemical CO2 to CO Conversion over Sn-Doped Copper Oxide Nanoparticles. *ACS Catal.* **12**, 15146-15156 (2022).

42 Markin, A. V., Markina, N. E., Popp, J. & Cialla-May, D. Copper nanostructures for chemical analysis using surface-enhanced Raman spectroscopy. *TrAC Trends in Analytical Chemistry* **108**, 247-259 (2018).

43 Chernyshova Irina, V., Somasundaran, P. & Ponnurangam, S. On the origin of the elusive first intermediate of CO2 electroreduction. *Proc. Natlù Acad. Sci. U.S.A.* **115**, E9261-E9270 (2018).

44 Firet, N. J. & Smith, W. A. Probing the Reaction Mechanism of CO2 Electroreduction over Ag Films via Operando Infrared Spectroscopy. *ACS Catal.* **7**, 606-612 (2017).

45 Gunathunge, C. M., Li X., Li J., Hicks R. P., Ovalle V. J., and Waegele M. M. Spectroscopic Observation of Reversible Surface Reconstruction of Copper Electrodes under CO2 Reduction. *J. Phys. Chem. C* **121**, 12337-12344 (2017).

46 Chen, X., Henckel D. A., Nwabara U. O., Li Y., Frenkel A. I., Fister T. T., Kenis P.I J. A. & Gewirth A. A. Controlling Speciation during CO2 Reduction on Cu-Alloy Electrodes. *ACS Catal.* **10**, 672-682 (2020).

47 Li, X., Sun Y., Xu J., Shao Y., Wu J., Xu X., Pan Y., Ju H., Zhu J. & Xie Y. Selective visible-light-driven

photocatalytic CO2 reduction to CH4 mediated by atomically thin CuIn5S8 layers. *Nat. Energy* **4**, 690-699 (2019).

48 Zhao, Y., Chang X., Malkani A. S., Yang X., Thompson L., Jiao F., and Xu B. Speciation of Cu Surfaces During the Electrochemical CO Reduction Reaction. *J. Am. Chem. Soc.* **142**, 9735-9743 (2020).

49 Niu, Z.-Z., Gao F.-Y., Zhang X.-L., Yang P.-P., Liu R., Chi L.-P., Wu Z.-Z., Qin S., Yu X., and Gao M.-R. Hierarchical Copper with Inherent Hydrophobicity Mitigates Electrode Flooding for High-Rate CO2 Electroreduction to Multicarbon Products. *J. Am. Chem. Soc.* **143**, 8011-8021 (2021).

50 Pan, Z., Wang, K., Ye K., Wang, Y., Su, H.-Y., Hu, B., Xiao, J., Yu, T., Wang,, Y. & Song S. Intermediate Adsorption States Switch to Selectively Catalyze Electrochemical CO2 Reduction. *ACS Catal.* **10**, 3871-3880 (2020).

51 Al-Mahayni, H., Wang, X., Harvey, J.-P., Patience, G. S. & Seifitokaldani, A. Experimental methods in chemical engineering: Density functional theory. *Can. J. Chem. Eng.* **99**, 1885-1911 (2021).

52 Nørskov, J. K., J. Rossmeisl, A. Logadottir, L. Lindqvist, J. R. Kitchin, T. Bligaard, and H. Jónsson Origin of the Overpotential for Oxygen Reduction at a Fuel-Cell Cathode. *J. Phys. Chem. B* **108**, 17886-17892 (2004).

53 Jouny, M., Lv, J.-J., Cheng, T., Ko B. H., Zhu, J.-J., Goddard, W. A. III & Jiao F. Formation of carbon–nitrogen bonds in carbon monoxide electrolysis. *Nat. Chem.* **11**, 846-851 (2019).

54 Meng, N., Shao J., Li H., Wang Y., Fu X., Liu C., Yu Y. & Zhang B. Electrosynthesis of formamide from methanol and ammonia under ambient conditions. *Nature Communications* **13**, 5452 (2022).

55 Rooney, C. L., Wu, Y., Tao, Z. & Wang, H. Electrochemical Reductive N-Methylation with CO2 Enabled by a Molecular Catalyst. *J. Am. Chem. Soc.* **143**, 19983-19991 (2021).

56 Zhang, Y. Al-Mahayni H., Chartrand D., Seifitokaldani A., & Kornienko N. Oxy-reductive CN bond formation via pulsed electrolysis. *ChemRxiv* (2022).

57 Feng, Y., Yang, H., Zhang, Y., Huang X., Li,, L., Cheng, T., and Shao, Q. Te-Doped Pd Nanocrystal for Electrochemical Urea Production by Efficiently Coupling Carbon Dioxide Reduction with Nitrite Reduction. *Nano Letters* **20**, 8282-8289 (2020).

58 Cao, N., Quan Y., Guan A., Yang C., Ji Y., Zhang L., Zheng G. Oxygen vacancies enhanced cooperative electrocatalytic reduction of carbon dioxide and nitrite ions to urea. *Journal of Colloid and Interface Science* **577**, 109-114 (2020).

59 Yuan, M., Chen, J., Xu, Y., Liu, R., Zhao, T., Zhang, J., Ren, Z., Liu, Z., Streb, C., He, H., Yang, C., Zhang, S. & Zhang, G. Highly selective electroreduction of N2 and CO2 to urea over artificial frustrated Lewis pairs. *Energy & Environmental Science* **14**, 6605-6615 (2021).

60 Muramoto, E., Chen, W., Jia, X. Friend, C. M., Sautet, P., Madix, R. J. Toward benchmarking theoretical computations of elementary rate constants on catalytic surfaces: formate decomposition on Au and Cu. *Chem. Sci.* **13**, 804-815 (2022).

61 Ojeda, M. & Iglesia, E. Formic Acid Dehydrogenation on Au-Based Catalysts at Near-Ambient Temperatures. *Angew. Chem. Int. Ed.* **48**, 4800-4803 (2009).

62 Ammon, C., A. Bayer, G. Held, B. Richter, Th. Schmidt, H.-P. Steinrück Dissociation and oxidation of methanol on Cu(110). *Surface Science* **507-510**, 845-850 (2002).

63 Chen, W.-K., Liu, S.-H., Cao, M.-J., Yan, Q.-G. & Lu, C.-H. Adsorption and dissociation of methanol on Au(1 1 1) surface: A first-principles periodic density functional study. *Journal of Molecular Structure: THEOCHEM* **770**, 87-91 (2006).

64 Ben David, R., Ben Yaacov, A., Head, A. R. & Eren, B. Methanol Decomposition on Copper Surfaces under Ambient Conditions: Mechanism, Surface Kinetics, and Structure Sensitivity. *ACS Catal.* **12**, 7709-7718 (2022).

65 Rabinowitz, J. A. & Kanan, M. W. The future of low-temperature carbon dioxide electrolysis depends on solving one basic problem. *Nature Communications* **11**, 5231 (2020).

66 Huang, J. E., Li F., Ozden A., Rasouli A. S., F. De Arquer P. G., Liu S., Zhang S., Luo M., Wang X., Lum Y., Xu Y., Bertens K., Miao R. K., Dinh C.-T., Sinton D., & Sargent E. H. CO2 electrolysis to multicarbon products in strong acid. *Science* **372**, 1074-1078 (2021).

67 Gu, J., Liu S., Ni W., Ren W., Haussener S. & Hu X. Modulating electric field distribution by alkali cations for CO2 electroreduction in strongly acidic medium. *Nat. Catal.* **5**, 268-276 (2022).

68 Li, J. & Kornienko, N. Electrocatalytic carbon dioxide reduction in acid. *Chem Catalysis* **2**, 29-38 (2022).

69 Kim, J. Y. T., Zhu, P, Chen, F.-Y., Wu, Z.-Y., Cullen, D. A. & Wang, H. Recovering carbon losses in CO2 electrolysis using a solid electrolyte reactor. *Nat. Catal.* **5**, 288-299 (2022).

Chapitre 5 – Conclusion and perspectives

Using biomass-derived furfural and CO_2 as building blocks to synthesize fuels or useful chemicals can relieve the reliance on fossil fuels, solve the energy crisis and environmental deterioration. Also, the products function as a route to store energy in chemical bonds as a medium for storing discontinuous renewable electricity. Although these research directions have been developed for many years, varieties of electrocatalysts have been designed for these reactions, and the effects of the reaction have been investigated, the understanding of the reaction mechanisms are still unclear and there exist significant debates on this. Thus, using advanced techniques to reveal the reaction pathways is important for the improvement of these reactions. Herein, we use operando spectroscopy, Raman, IR and XRD to show the reaction intermediates, active sites, and the evolution of the catalysts during the reactions. Possible mechanisms were proposed with the assistance of control experiments or DFT calculations, which provide new possibilities for designing new reactions and highly efficient catalysts.

5.1 Furfural reduction

Using electrochemically roughed Cu foil as a model catalyst for furfural reduction reaction. MF and FA were obtained as the final products, FE is 57.5 and 43.0% respectively. The investigation of different facets shows that Cu (110) shows a higher FA production than Cu (111), Cu (100), and Cu foil, which means that (110) facets are the active sites for the formation of FA. On the contrary, the production of MF on these single facets is negligible. After these facets were roughed, the production of MF increased, which shows that the defects might be the active sites for MF. In-situ Raman shows that the formation of MF and FA share the same intermediate, the desorption of the intermediate will form FA, the hydrogenation of the intermediate will form MF as the final product. Elucidating the chemical nature of active sites and reaction pathways can help control the selectivity of the reaction and achieve the accurate adjustment of the aim products.

5.2 C-N bond formation

Coupling CO_2 and NH_3 to synthesize acetamide and formamide as C-N bond products on Cu or CuO nanoparticles. The FE of C-N bond products is ~ 10% in total, and acetamide is the main C-N

bond product. The effect of different amounts of catalyst, concentration of NH_3, pH, cations, and potential are investigated to optimize the reaction conditions, and the best option is 50 mg Cu NPs, 0.3 M NH_3, 1 M KOH, -0.78 V (vs. RHE). In-situ IR results reveal the intermediates of the reaction, the formation of formamide and formate share the same intermediates. The production of acetamide undergoes a similar reaction pathway to acetate, the difference is the nucleophilic attack of NH_3 or OH^- (form acetate) to ketene intermediate. Although the FE of the C-N bond formation is still low, a highly efficient catalyst can be designed based on the mechanism. This reaction expands the application of CO_2RR and also benefits the development of organic synthesis.

5.3 C-S bond formation

Co-electrolysis of CO_2 and sulfide in an aqueous solution produces organic sulfide HMS, SA, and MS as C-S bond compounds. The FE is approximately 6% in total, and HMS is the major C-S bond product. In-situ XRD shows that Cu^0 is the active species for the production of HMS, and the combination of operando Raman and DFT calculation suggests *CHOH is the key intermediate. The rate-determining step is the interaction between *CHOH and SO_3^{2-}. Although the FE of this reaction is low, based on the mechanism we can develop a catalyst that has high efficiency in producing aldehyde, due to it being the intermediate of the formation of HMS, for synthesizing C-S bond products in a high yield. It's the first time to report combining CO_2RR with the addition of sulfur species for C-S bond formation. For future applications, except for the development of the electrocatalyst, optimizing the reaction condition and designing a suitable electrolyzer may also improve the selectivity of the C-S coupling reaction. This method provides a new and sustainable avenue for the synthesis of organic sulfide.

In all, developing new reactions with abundant natural feedstocks is essential for the improvement of organic synthesis, with the help of in-situ techniques, making the enhancement of the efficiency of these reactions becomes possible, and providing the possibility for partially replacing traditional organic synthesis methods.

5.4 Perspective

Furfural reduction and CO_2 reduction reaction are sustainable ways to synthesize useful chemicals. Considering their future applications in real industry, energy efficiency, selectivity, and the duration of the reaction should be considered. To achieve this, a robust and highly efficient reaction system should be designed.

As we mentioned in Chapter 1, electrocatalyst, electrolyte, local environment around the electrode, and the configuration of the cell are the essential factors for the reaction performance. Thus we need to optimize these conditions and elucidate the precise functions of these factors. In-situ techniques can guide the design of the reaction system by revealing the evolution of the catalysts, active sites, reaction intermediates, and the function of pH changes, cations, and anions.

In addition to optimizing the reaction system, expanding the products can also be beneficial to the future applications of these reactions. Combining CO_2 and furfural with other small molecules such as ammonia, nitrate or nitrite, nitrogen, and sulfite to synthesize compounds with heteroatoms is a green and sustainable way of synthesizing organic molecules. We have already used CO_2 with nitrogen and sulfur source to synthesize C-N bond and C-S bond products, more nitrogen and sulfur source can be explored to expand the types of products. Apart from acetamide and formamide, urea, methylamine, and ethylamine are also obtained as C-N bond products. The electrosynthesis of C-S bond products is yet to be established. More organic nitride and organic sulfide are expected to be obtained by this method, which can be used to partially replace traditional organic synthetic routes such as Pd-based cross-coupling methods. Furthermore, different heteroatoms such as phosphorus, especially non-toxic phosphate, hypophosphite, or phosphite can also be used as feedstock to synthesize organophosphorus because of their similar properties with nitrogen and sulfur. Through this, toxic and flammable precursors PCl_3, PH_3, or white phosphorus can be avoided. In addition, similar like traditional CO_2RR to produce C-H or C-O products, the selectivity and activity of the reaction should also be improved, by using results of in situ techniques for guidance.

In all, developing electrocatalytic biomass and CO_2 reduction reaction pathways for synthesizing products with heteroatoms as new reactions, designing a highly efficient reaction system and

especially new catalysts, using in-situ techniques to reveal reaction mechanisms is beneficial for green and sustainable organic synthesis en route to achieving a zero carbon society.

Chapitre 6 –Supplementary information for: Probing electrosynthetic reactions with furfural on copper surfaces

6.1 Materials and methods:

6.1.1 Cu synthesis:

Rough Cu foil was obtained by an electrochemical roughening method. Commercial Cu foil was cut to a suitable size as the precursor, and polished with Al powder. Then the Cu foil was washed by DI water and ultrasonic to remove the impurities on the surface. After this procedure, the Cu foil was used as working electrode in a three-electrode system (Ag/AgCl as reference, carbon rod as counter), with CO_2-saturated $KHCO_3$ as electrolyte, 6 cyclic voltammetry cycles were conducted in the range of 0 to -1.6 V (vs. Ag/AgCl), with a scan rate at 50 mV/s. Subsequently, chronoamperometry was carried out at +0.9 V for 1 min to oxidize the Cu foil, followed by the reduction process at -0.3 V for 10 mins. The illustration of the roughening scheme is shown in Figure 2.

Single crystal Cu substrates were purchased from MTI corporation and used as received after making electrical contact to a substrate holder. The crystallinity and orientation is confirmed through XRD measurements and through the acquisition of rocking curve data that shows peak FWHMs on the order of 0.6 – 0.7^{o}.

6.1.2 Physical characterization:

X-ray diffraction (XRD) patterns were measured on a Bruker D8 Advance diffractometer with a Cu Kα radiation source (λ = 1.5418 Å). High-resolution x-ray photoelectron spectroscopy (XPS) measurements were conducted on a Vacuum Generator Escalab 220i XL x-ray photoelectron spectrometer, calibrated by using carbon (C1s 284.6 eV). A Jeol, JSM -840A was used for scanning electron microscopy (SEM) measurements. Transmission electron microscopic (TEM) images were performed on JEOL JEM-2100F FEG-TEM, operated at 200 kV. The sample was scratched from rough Cu foil on to carbon film.

6.1.3 Electrochemistry and product quantification:

Cyclic voltammetry (CV) and other electrochemical techniques were performed using a Bio-Logic SP-150 Potentiostat (BioLogic Science Instruments, France). A three-electrode system has been employed by applying the above rough Cu foil as the working electrode, Ag/AgCl as the reference electrode and a Pt wire as the counter electrode. K_2SO_4 solution (1 M, with added H_2SO_4 to adjust to pH 3) was used as the electrolyte in the measurements. The CVs were measured in the range of 0~-0.526 V (vs. RHE) at a sweep rate of 20 mV s^{-1}. Potentiostatic electrolysis was conducted in a two-compartment custom built glass H-cell reactor.

The anode and cathode chambers were separated by a glass frit. Before each electrolysis experiment, 20 ml electrolyte was added into the reactor and purged with N_2 for 15 mins to remove dissolved gases. The reactor was sealed and the electrolyte was stirred at 500 rpm during the reaction. All reactions were carried out at room temperature.

In order to analyze the products of the reaction, gas chromatography (GC, SRI 8610C, Mandel) and NMR (Bruker AVANCE II 400 se) were performed to reveal the content and composition of the gas and liquid products respectively. After 3 hs electrolysis, 10 mL gas was extracted from the reactor by syringe and injected into GC to test the content of hydrogen. 400 µL liquid product was mixed with 100 µL D_2O to test the NMR and investigate the content of furfural alcohol (FA) and 2-methylfuran (MF). The faradaic efficiency (FE) was calculated by using the following formula:

$$\varepsilon_{FE} = \frac{\alpha n F}{Q}$$

where α is electron transfer numbers (for the formation of H_2 and FA is 2, MF is 4), n is the moles of the products, F is faraday constant (96485 C mol^{-1}), Q is the charge passed in total during the reaction.

The pH of the solution did not change by more than 0.3 pH units throughout each catalytic run, as calculated from the total charge passed through the circuit.

6.1.4 Raman spectroscopy:

A three-electrode electrochemical cell was used for in-situ Raman experiment. Titanium foil was used as the counter electrode, Ag/AgCl was used as reference, and rough Cu foil as working electrode in a custom-built Teflon spectroelectrochemical cell. The scheme was shown in the main text Figure 2.1. The electrolyte is 1M K_2SO_4 (with H_2SO_4, pH3), which is also bubbled with N_2 for 15 mins to remove the dissolved gas. Raman spectroscopy were recorded on a Renishaw InVia Raman Microscope and excited with 633 nm excitation laser.

6.2 Supplementary figures and tables

Table 6.1 - Yields of the reaction, corresponding to Figure 3 in the main text.

Potential (V vs. RHE)	2-MF(%)	FA(%)
-0.426	0.75	1.12
-0.526	0.77	1.62
-0.626	0.90	1.97
-0.726	1.18	1.19
-0.826	0.88	1.53

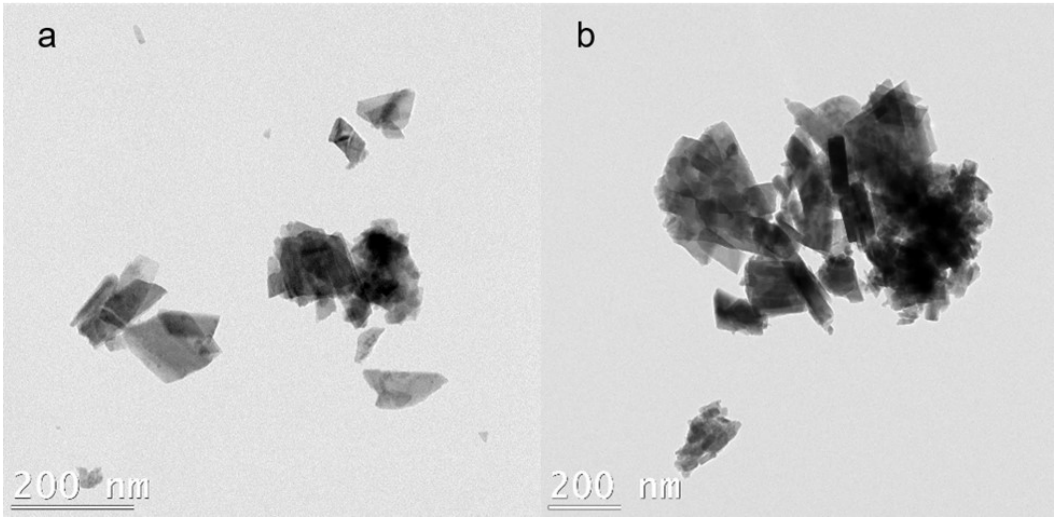

Figure 6.1 - TEM images of rough Cu foil.

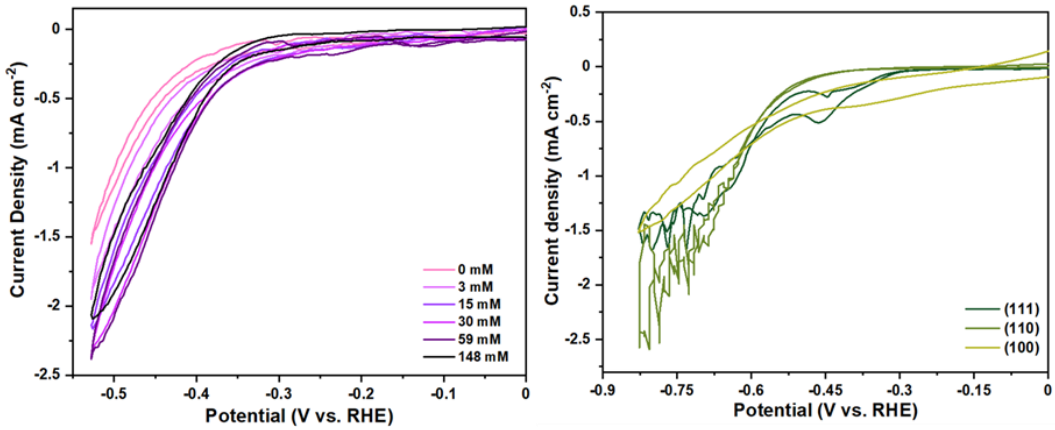

Figure 6.2 - CV curves of (a) rough Cu foil with different amount of furfural; (b) single crystal Cu foil with 59 mM furfural.

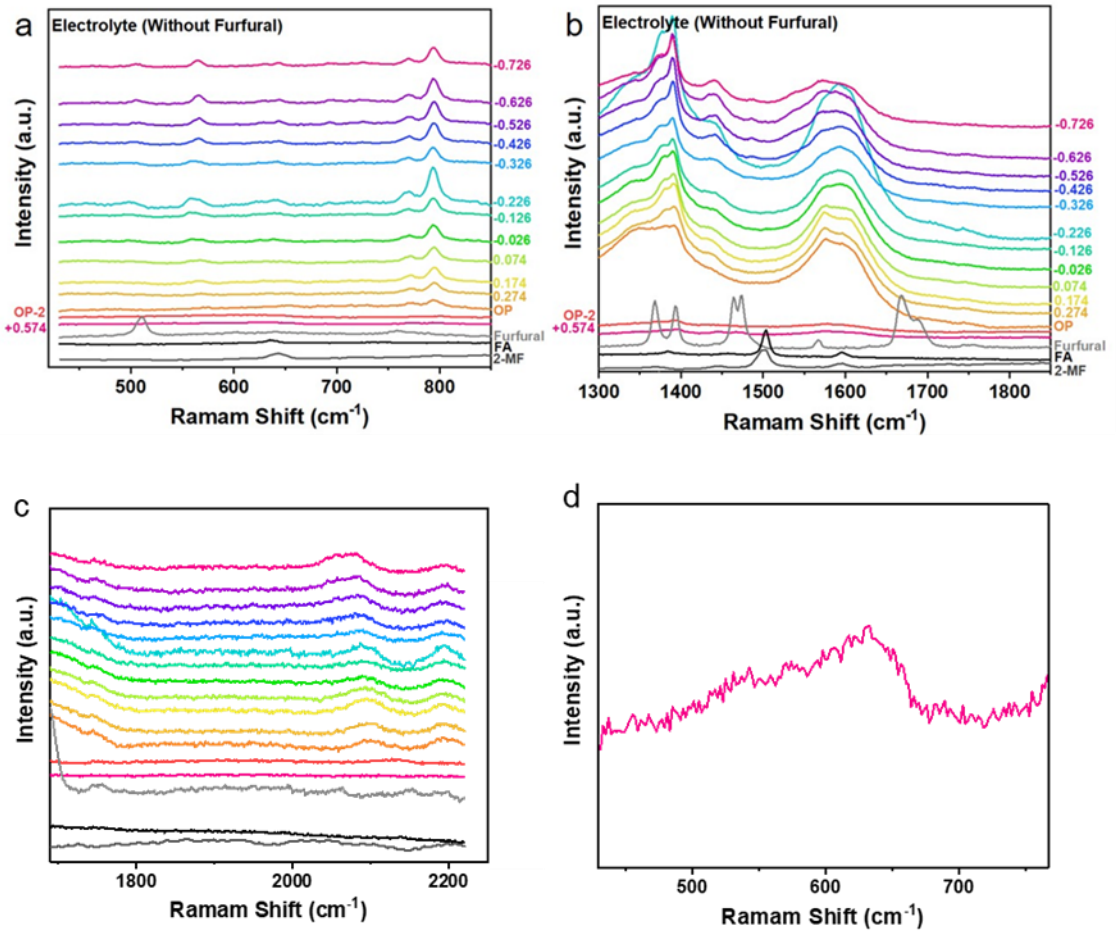

Figure 6.3 - Operando SER spectra on R-Cu surface without adding furfural in the (a) low frequency (b) medium frequency and (c) high frequency regions. A zoomed in spectra of the R-

Cu at open circuit potentials is also illustrated to clearly show the spectrum corresponding to the CuO_x surface.

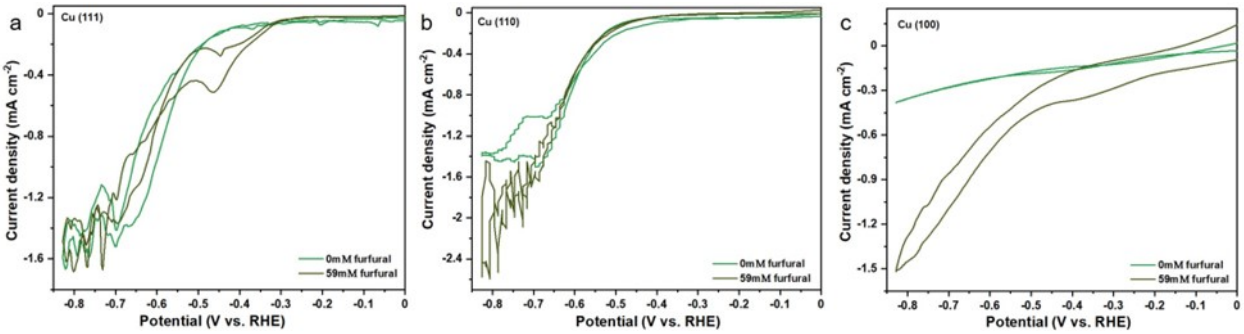

Figure 6.4 - CV curves of single crystal Cu (a) Cu (111); (b) Cu (110); (c) Cu (100) with (dark green) and without furfural (light green).

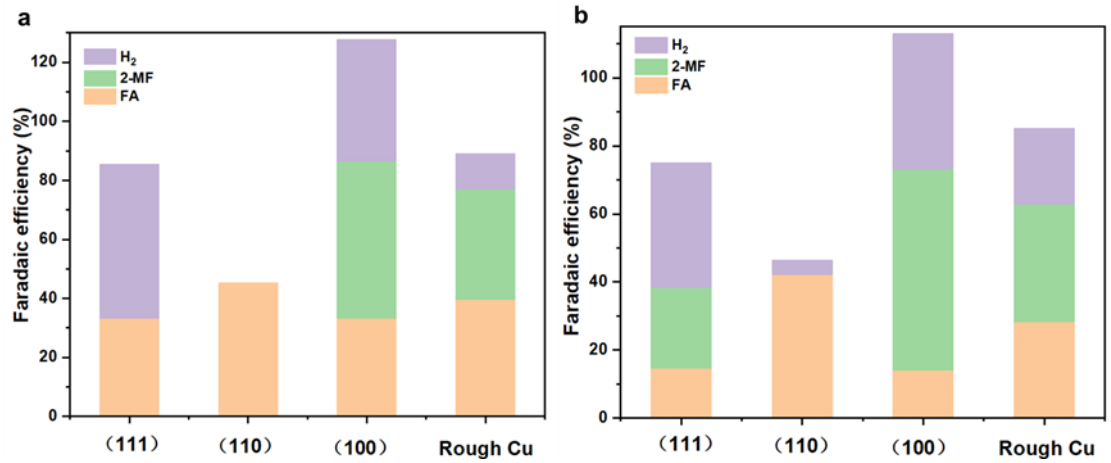

Figure 6.5 - Faradaic efficiency of roughen single crystal Cu under with 59 mM furfural at different applied potential (a) -0.526 V; (b) -0.726 V vs. RHE.

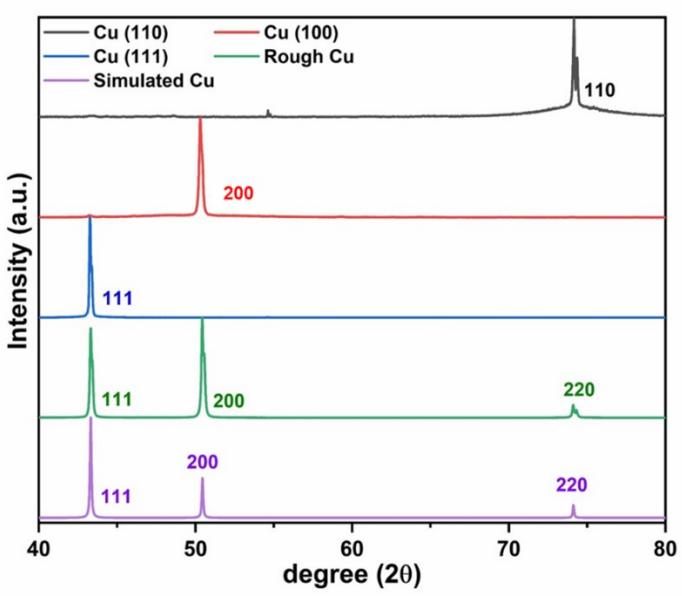

Figure 6.6 - Low-magnification XRD patterns of rough Cu and single crystal Cu electrodes.

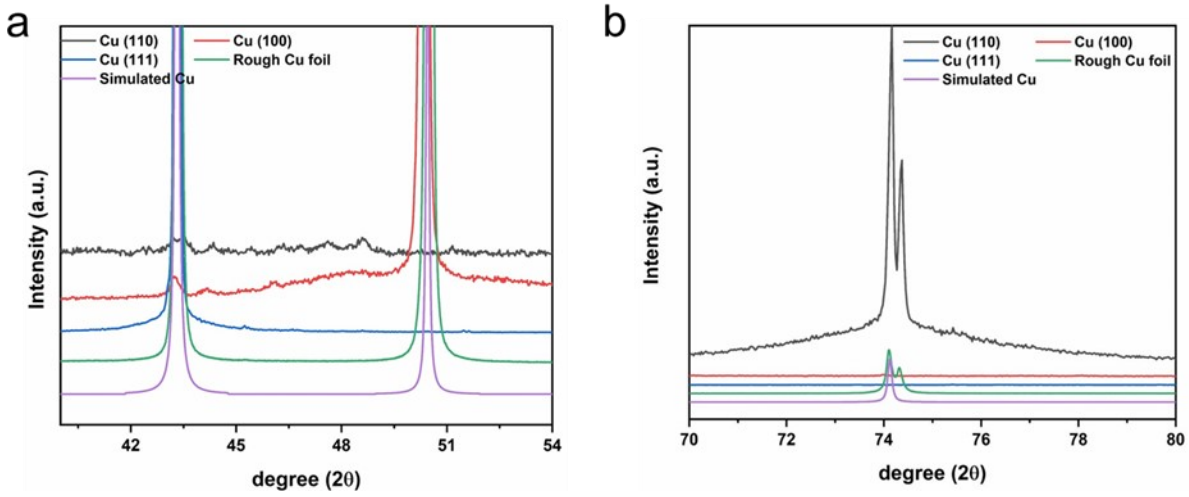

Figure 6.7 - Zoomed-in XRD patterns of single crystal Cu electrodes after roughening show the appearance of weak peaks and a broadening at the base of the main peaks, indicating the onset of the formation of a polycrystalline surface structure.

Chapitre 7 – Supplementary information for: Electrochemically Driven C-N Bond Formation from CO_2 and Ammonia at the Triple-Phase Boundary

7.1 Characterization

Scanning electron microscopic (SEM) images and EDS were measured using a JEOL JSM-7600F Field Emission SEM microscope. Transmission electron microscopic (TEM) images were performed on JEOL JEM-2100F FEG-TEM, operated at 200 kV.

7.1.1 Electrochemistry and product quantification:

Linearly sweep voltammetry (LSV) was accomplished using a Bio-Logic SP-200 Potentiostat (BioLogic Science Instruments, France). A three-electrode system has been employed by applying the carbon cloth gas diffusion layer (GDL-CT (W1S1009, Fuel Cells Etc.) as the working electrode, Ag/AgCl as the reference electrode and a glassy carbon rod as the counter electrode. While a Hg/HgOH reference is preferred for alkaline conditions due to its higher stability, we needed a small Ag/AgCl electrode to fit within our cell and referenced it periodically to a master Ag/AgCl electrode to ensure that there was no significant potential drift.

The preparation of working electrode followed steps: 10 mg Cu (Alfa Aesar, Copper Nanopowder, 99.9% APS 20-50 nm, Lot P11F044) or CuO (Alfa Aesar, Copper(II) Oxide, nanopowder, Lot Y19E022) commercial catalyst powder (20-50 nm particle size) was added into a mixture with 100 µL H_2O, 300 µL ethanol, 25 µL Nafion (5% wt.). After ultrasonic mixing for 10 minutes, 100 µL of the catalyst ink was dropped onto the carbon cloth and allowed to dry naturally under ambient conditions. This led to a Cu loading of approximately 2 mg/cm^2. 1M KOH solution with different amounts of NH_4OH was used as the electrolyte in all of the measurements. The LSVs were measured in the range of 0.7 ~ -0.98 V (vs. RHE) at a sweep rate of 20 mV s^{-1}. Potentiostatic electrolysis was conducted in a gas diffusion electrode (GDE) cell. Before each electrolysis experiment, 1 mL electrolyte was added into the cell, the flow rate of CO_2 is 6mL/min. All reactions

were carried out at room temperature (23 ± 1 °C). Bulk electrolysis was carried out with 0.3 M NH_3 for Cu and 1.6 M NH_3 for CuO as these were the experimentally optimized conditions for C-N product generation rates. Because of the high gas generation rates and bubbling, we opted to carry out measurements in static mode (no flow) and in a 1-compartment cell. While this likely led to some crossover, product re-oxidation at the counter electrode, and an underestimation of the reaction efficiency, this geometry was nonetheless more optimal to minimize electrolyte volume and overcome the bubbling issue.

NH_3 was only fed through the liquid phase (as NH_4OH) while CO_2 was only added in through the gas phase. Further, no products were detected in the gas phase via GC analysis beyond CO, CH_4 and H_2.

In order to quantify the products of the reaction, gas chromatography (GC, SRI 8610C) and NMR (Bruker AVANCE II 400 se) were performed to reveal the content and composition of the gas and liquid products respectively. A sealed GDE cell was used and connected with the GC. The CO_2 flow rate employed was 6 mL/min and the products were probed in flow mode as the outlet from the GDE cell flowed directly through the GC. For NMR analysis, 400 µL liquid electrolyte after an electrolysis run was mixed with 400 µL D_2O to quantify liquid products. For NMR measurements, products were quantified using DMSO as an internal standard and calibration curves for several main products in the liquid phase like formate, acetate and ethanol (Fig. S1). Gaseous products were similarly quantified through the integration of peak area corresponding to various products, which were first measured with a series of calibration curves (H_2, CO, CH_4, C_2H_6…). The GC measurements were also collected in flow mode at 6 SCCM CO_2 flow with N_2 as the carrier gas in the GC. There was no evidence of nitrogenated products in the gas phase from GC measurements.

Typically, liquid products were acquired after 30 minutes of electrolysis. The Faradaic efficiency (FE) was calculated by using the following formula:

$$\varepsilon_{FE} = \frac{\alpha n F}{Q}$$

where α is electron transfer numbers, n is the moles of the products, F is the Faraday constant (96485 C mol^{-1}), Q is the charge passed in total during the reaction.

7.1.2 In-situ infrared (IR) spectroscopy:

IR spectra were acquired on a ThermoFischer Nicolet 380 FTIR-ATR with a ZnSe ATR crystal that was coated with a diamond surface. Typically, 200 scans were acquired for each measurement. A three-electrode GDE cell was used for the in-situ IR experiment. Cu wire was used as counter electrode, Ag/AgCl was used as reference, the above carbon cloth with CuO or Cu as working electrode. The electrolyte employed was 1M KOH with or without NH_4OH under a constant CO_2 gas flow. Thecatalyst, deposited onto a carbon cloth gas diffusion layer (coated with a microporous layer) was facing downwards towards the ATR crystal, with a thin electrolyte layer between. The working electrode was gently pressed with a porous foam stud so that there was still ample gas permeation into the triple-phase boundary that was being probed with the IR evanescent wave.

Raman Spectroscopy: Raman Spectra were collected using a Renishaw Invia system with a 785 nm laser having a 5mW output power. The laser line focus illumination technique was used that spread the laser intensity out over a line and minimized the power concentrated at any one spot. The spectra were collected at full intensity power and a typical collection time was 60 seconds. A water immersion objective (numerical aperture of 0.7, working distance of 1mm) was used to maximize signal intensity. Raman measurements were performed in a standard 3-electrode configuration instead of adapting to a gas-diffusion electrode as an initial test. For *operando* Raman measurements, Ag/AgCl reference and carbon cloth were used as reference and counter electrodes. N_2 or CO_2 purged 1M KOH or 1M KOH + NH_4OH were used as the electrolyte solutions. The working electrode consisted of Cu NPs loaded onto a Toray carbon paper electrode at approximately the same degree of catalyst loading as for the GDE. For surface-enhanced Raman measurements, a silver foil was roughened in a 0.1M KCl solution by cycling the potential between -0.2 to 0.4V vs. Ag/AgCl at 10 mV/s for 4 cycles. The roughened foil was rinsed and dried under ambient conditions prior to use. A drop of approx. 50 µl of the electrolysis solution was added overtop and measured with an immersion objective and 514 nm laser, operating at approx. 1 mW output power for 60 seconds.

7.2 Supplementary figures and tables

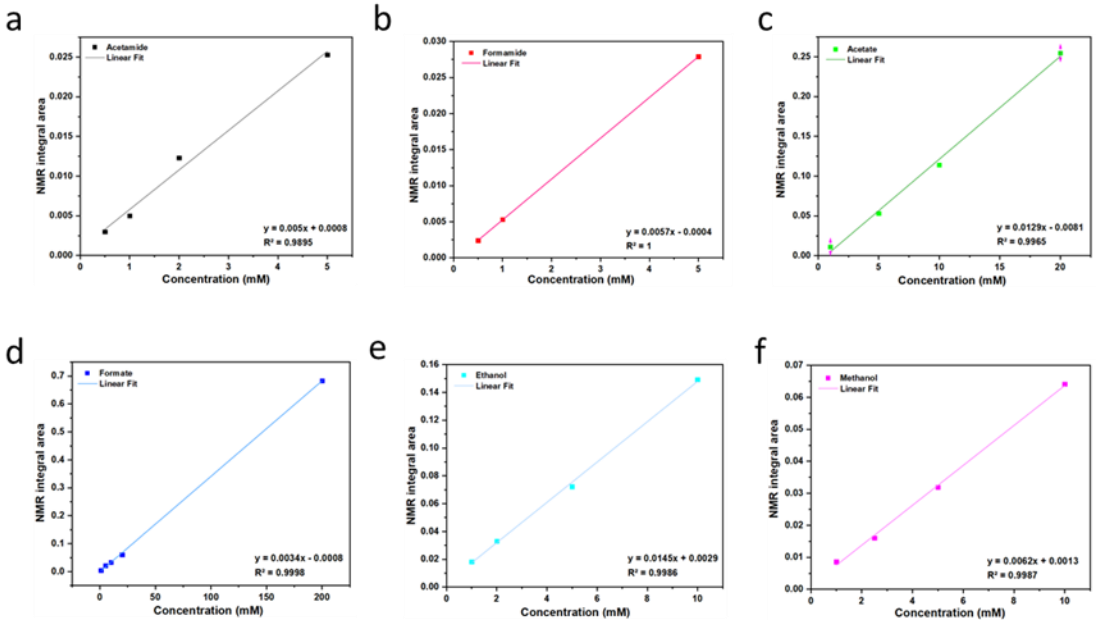

Figure 7.1 - NMR calibration curve of (a) Acetamide; (b) Formamide; (c) Acetate; (d) Formate; (e) Ethanol; (f) Methanol. The relative peak area is plotted vs. that of the DMSO internal standard.

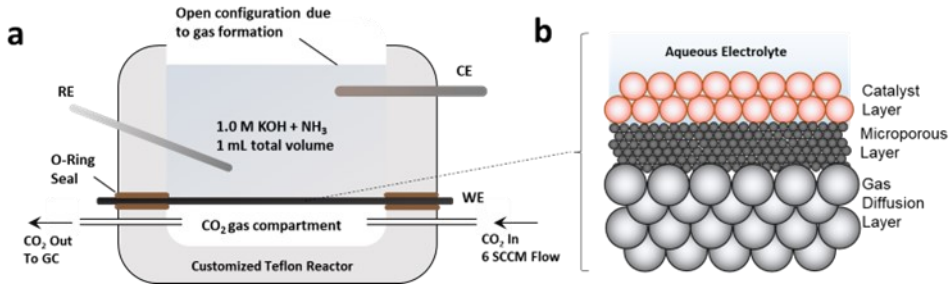

Figure 7.2 - Simplified schematic of CO_2 reduction reaction cell that enabled high-sensitivity detection of liquid products through the use of minimal (1mL) total electrolyte volume (a) sitting overtop of a gas-diffusion electrode (b). An open configuration was employed as gas bubbles generated throughout the reaction process prohibited using a conventional configuration.

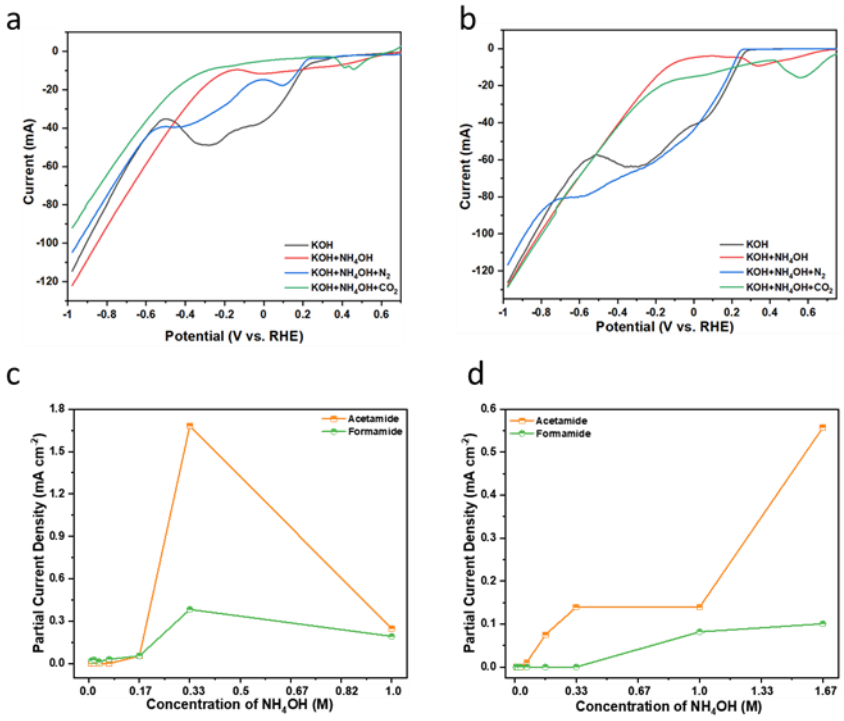

Figure 7.3 - LSV curves under different gas environment of (a) Cu; (b) CuO catalyst in different electrolytes. Partial current densities for C-N products from an initial screening of selecting optimal NH_4OH concentrations to add to the electrolyte were also different for Cu (c) and CuO (d).

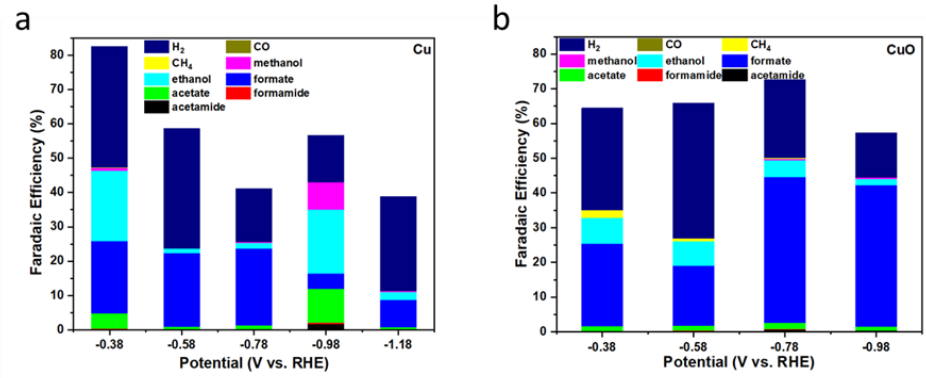

Figure 7.4 - Total product quantification for Cu (a) and CuO (b) catalysts.

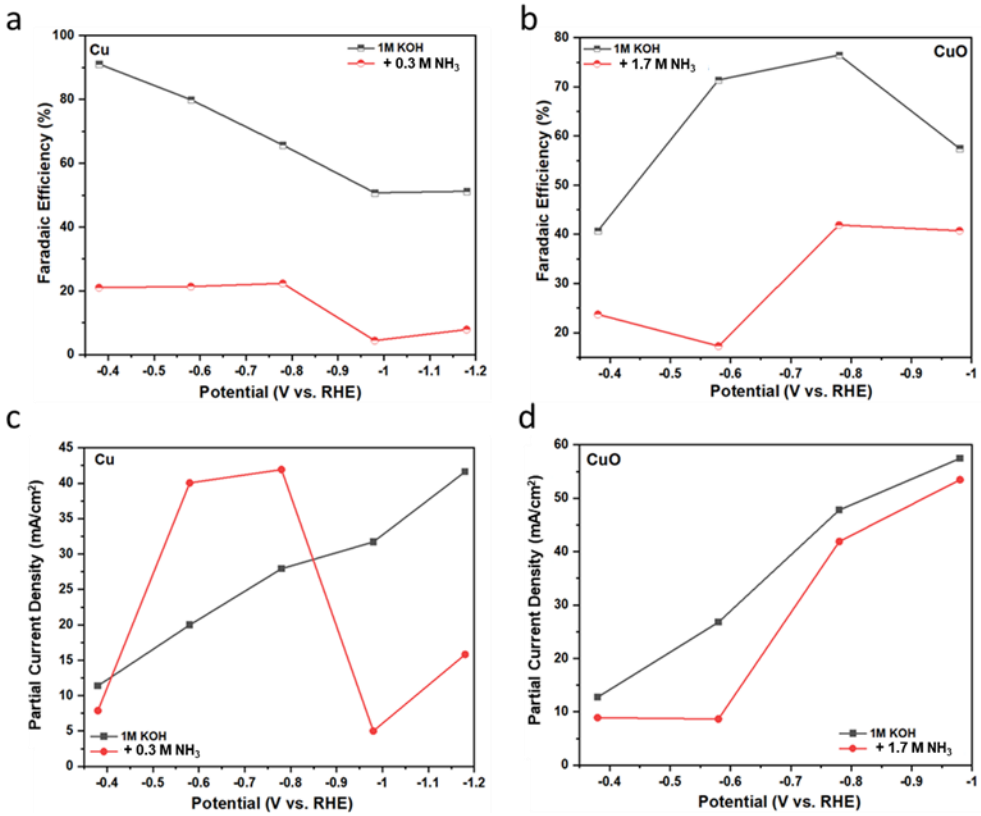

Figure 7.5 - Faradaic efficiency and partial current density for formate production in the absence and presence of NH_3 for Cu (a, c) and CuO (b, d) catalysts.

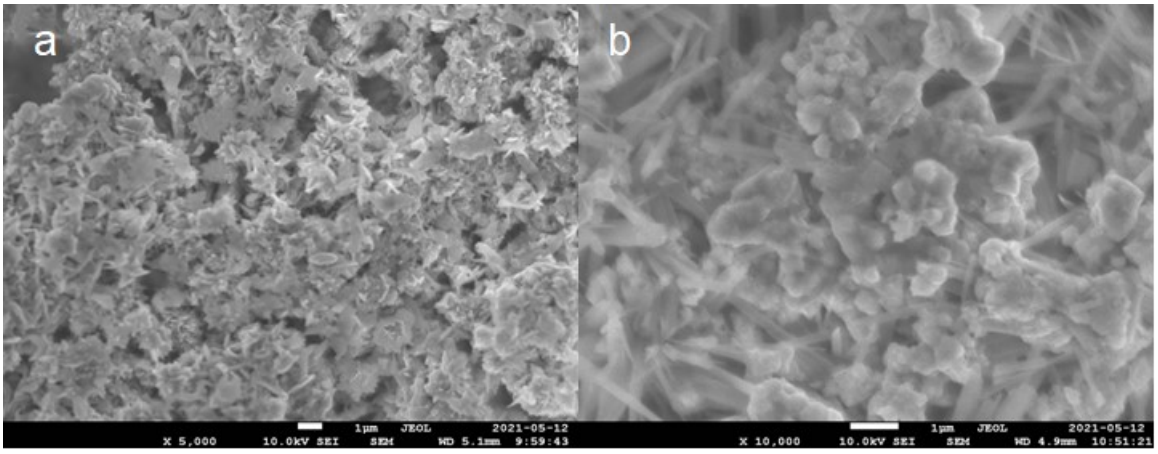

Figure 7.6 - SEM images of (a) CuO and (b) Cu after a typical controlled potential electrolysis reaction.

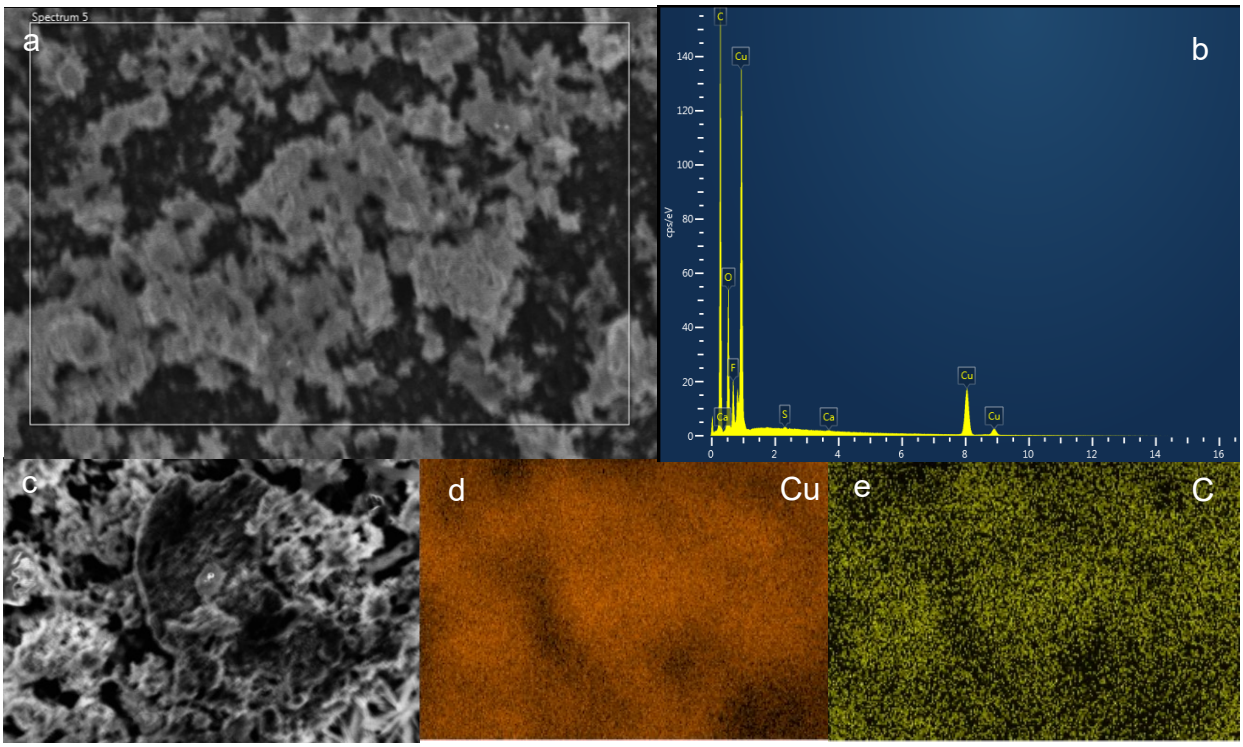

Figure 7.7 - (a, c) SEM images of the EDS area; EDS of CuO/C catalyst before reaction (b) EDS spectra; (d) Cu and (e) C element mapping after the reaction (30 min at -0.98V vs. RHE).

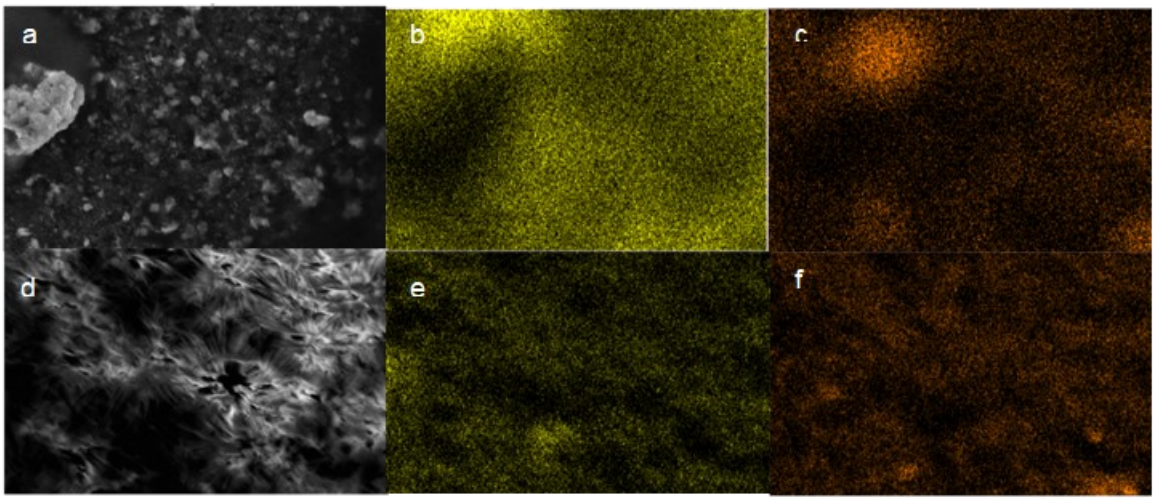

Figure 7.8 - SEM image (a) and elemental mapping of Cu (b) and C (c) before electrolysis. After electrolysis (30 min at -0.98V vs. RHE) an equivalent SEM image (d) and Cu (e) and C (f) elemental mapping was acquired for Cu catalysts.

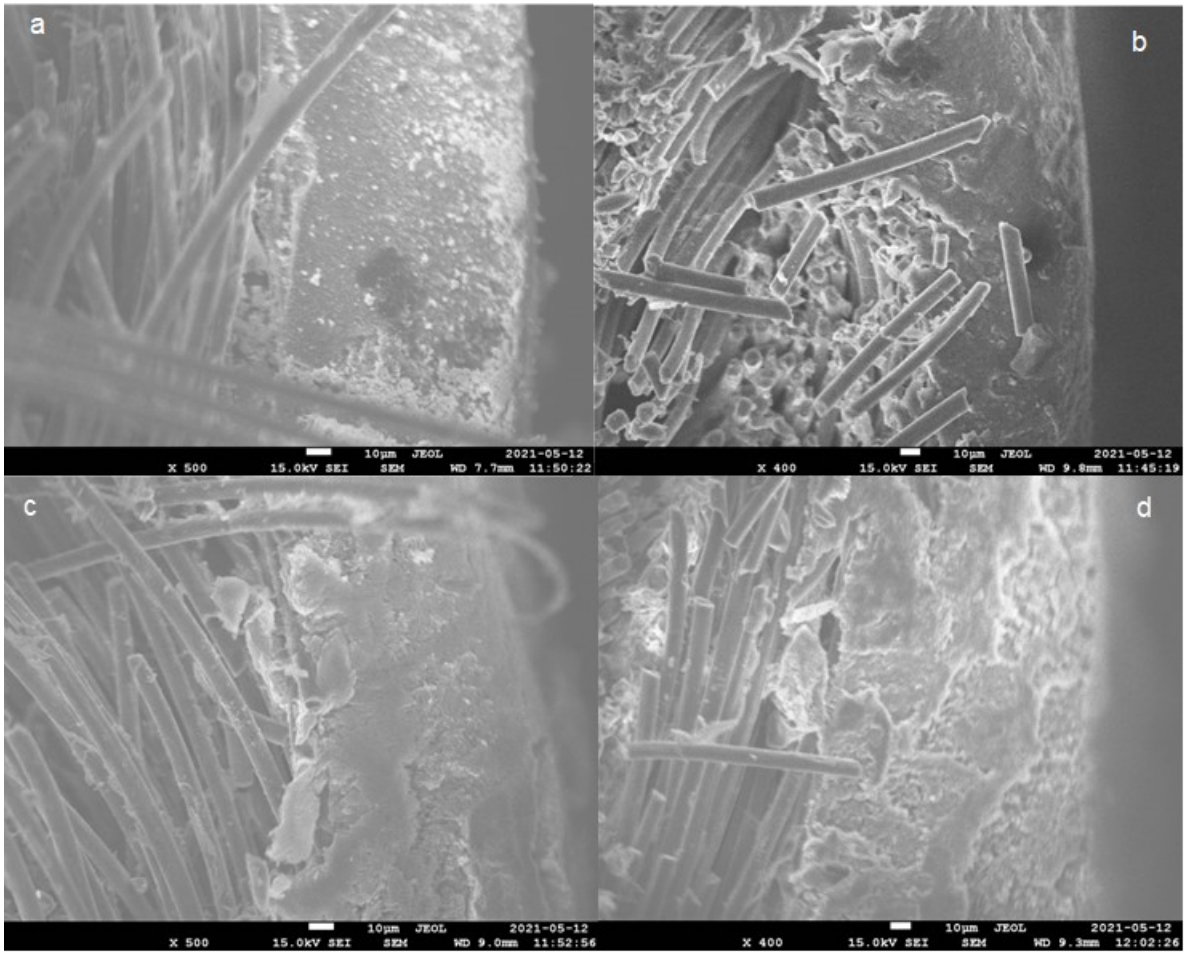

Figure 7.9 - SEM images of the cross session (a) CuO/C before reaction; (b) CuO/C after reaction; (c) Cu/C before reaction; (d) Cu/C after reaction.

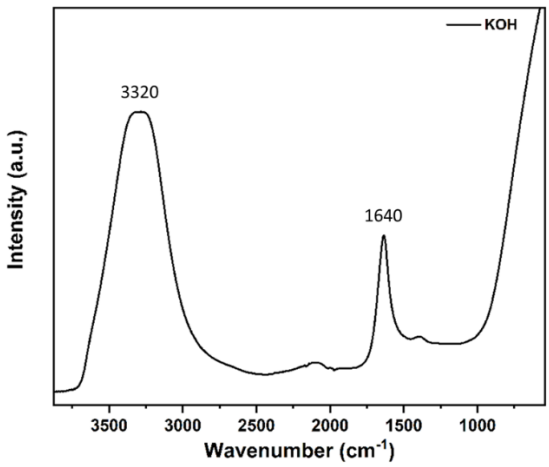

Figure 7.10 - IR spectrum of 1M KOH.

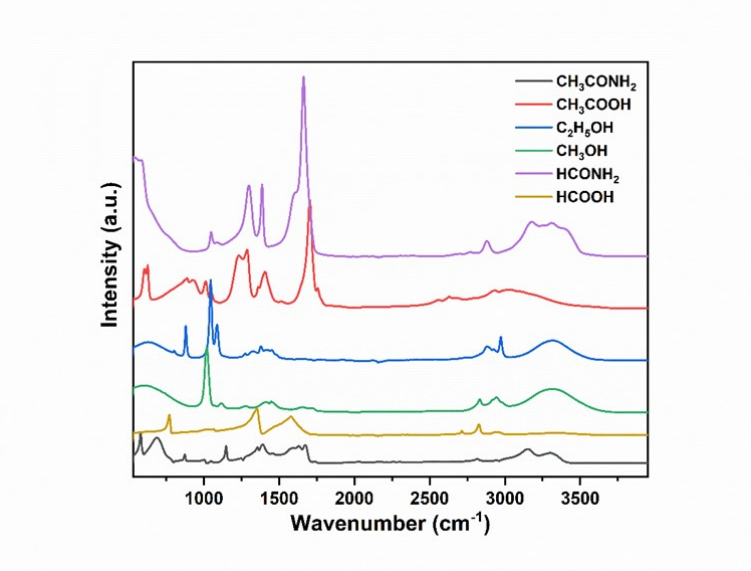

Figure 7.11 - IR spectra of several products detected in NH_3 + CO_2 electrolysis.

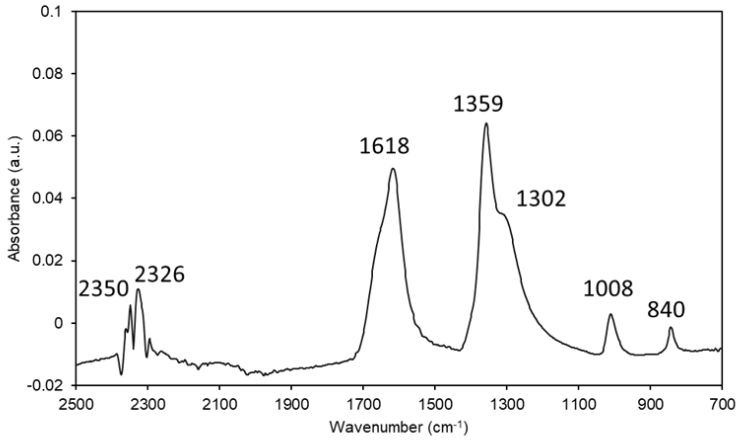

Figure 7.12 - IR spectrum of the spectroelectrochemical setup with a CO_2 flow in 1M KOH, using an Ar flow in 1M KOH as the background. Peaks attributable to CO_2 and carbonate are present.

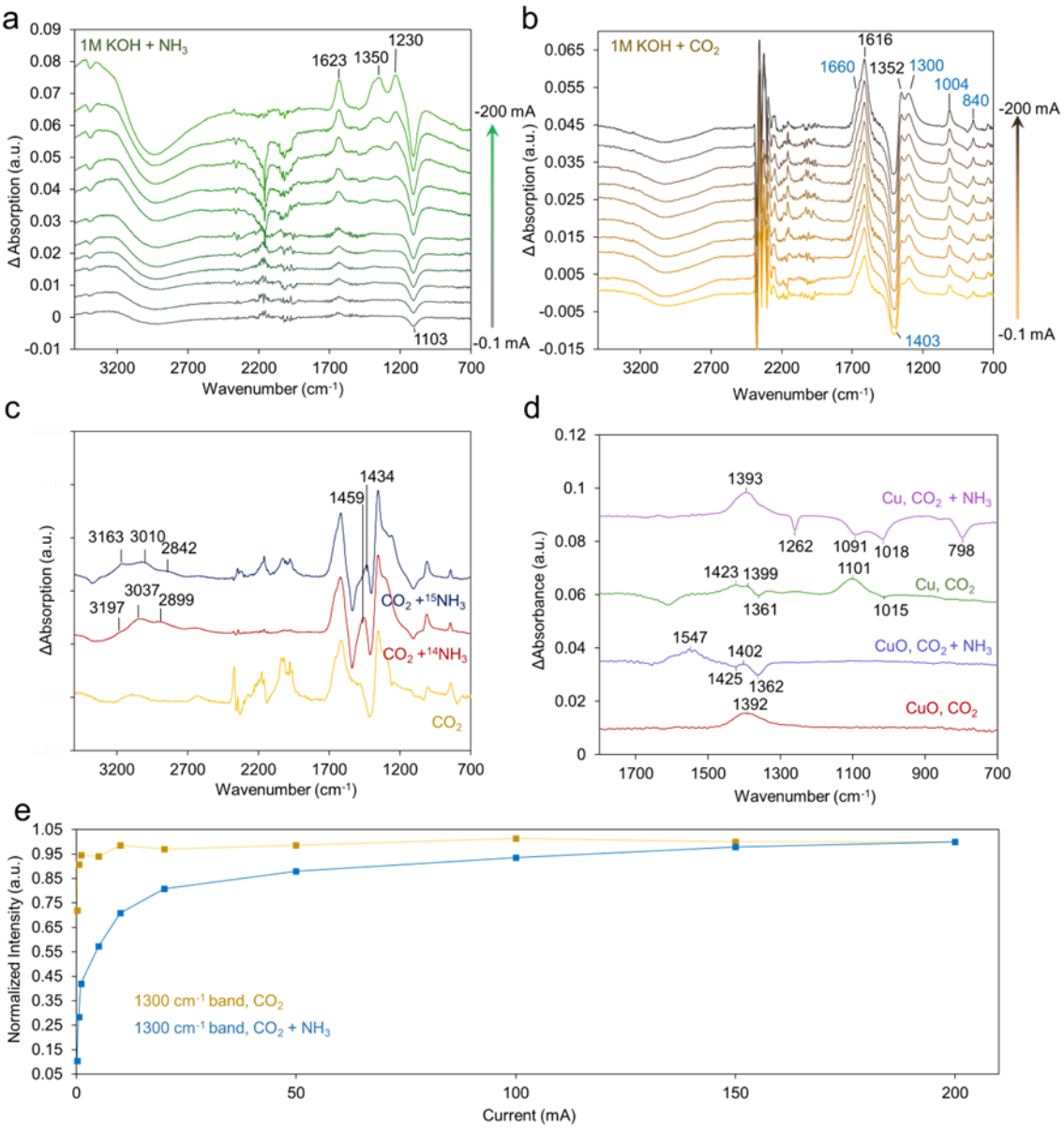

Figure 7.13 - With the system as open circuit used as the background, spectra were acquired at select operating currents in the presence of NH_3 only (a) and CO_2 only (b). With CO_2 and $^{15}NH_3$ reactants, the spectra in (c) are used to identify the peaks belonging to $^{15}NH_4^+$ as it forms during reaction conditions. Subtracting out the (bi)carbonate contributions helps see weaker bands from intermediates (d). The rise of the bicarbonate peak, normalized to itself at 200 mA, is relatively slower with NH_3 present, indicating a slower generation of this species.

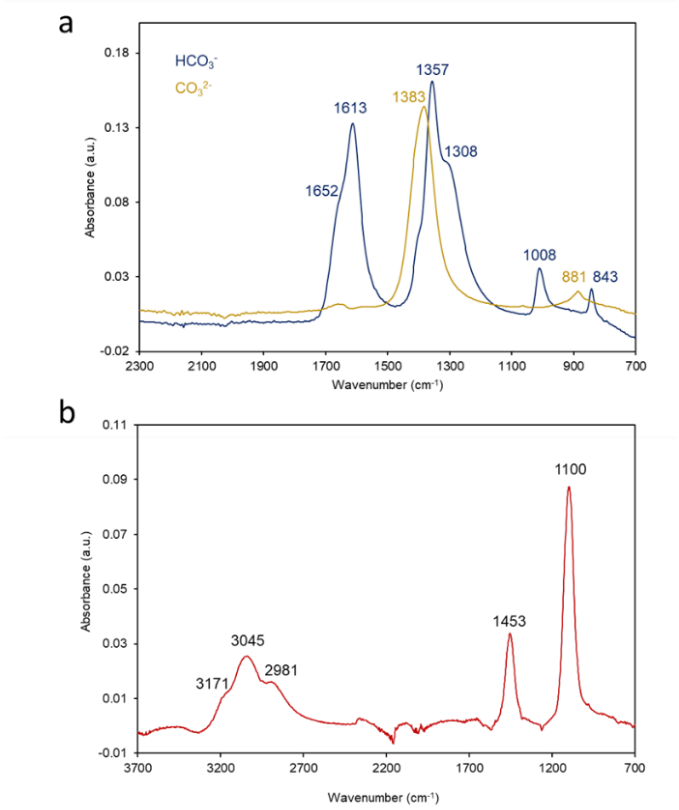

Figure 7.14 - IR spectra of $KHCO_3$ and K_2CO_3 dissolved in water (a) and NH_4^+ (b).

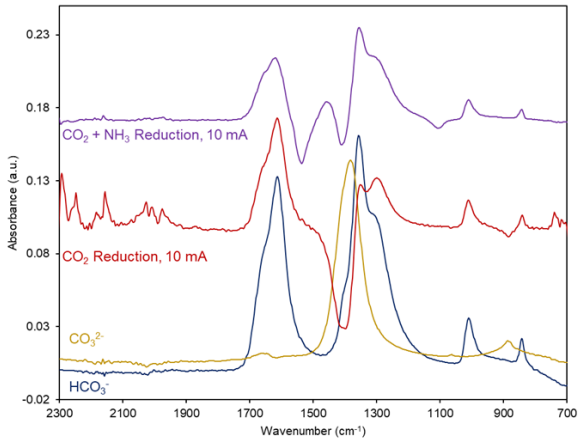

Figure 7.15 - Overlaid spectra of (bi)carbonate and CO_2 reduction.

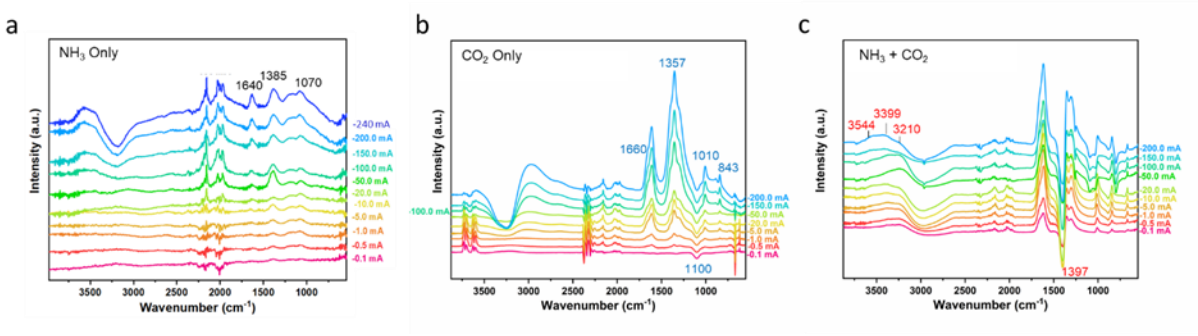

Figure 7.16 - IR spectra of Cu catalysts, with NH_3 only (a), CO_2 only (b), and NH_3 + CO_2 (c).

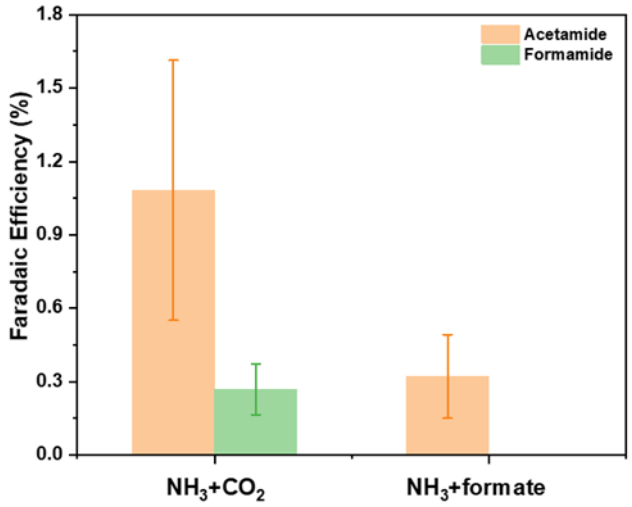

Figure 7.17 - C-N bond formation using 150 mM NaCOOH as the C-source instead of CO_2 in otherwise identical conditions (1M KOH, -0.98V vs. RHE, Cu catalyst). The average partial current for acetamide in the formate case was 0.2 mA/cm^{-2}.

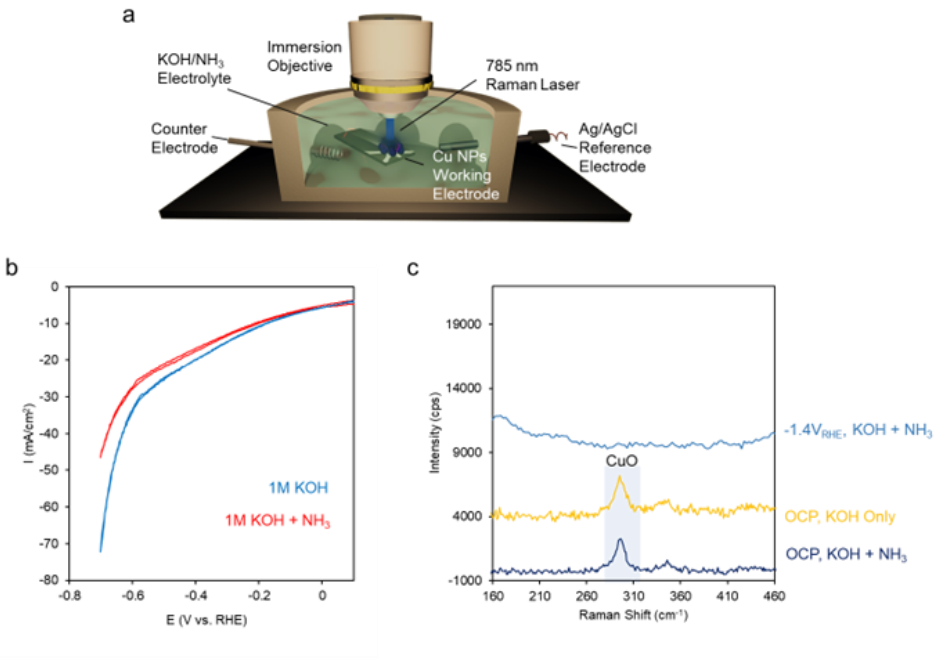

Figure 7.18 - The addition of NH_3 to the electrolyte suppressed the water reduction current of Cu nanoparticles (a). Surface-enhanced Raman revealed the reduction of the surface oxide under a negative bias of -1.4V vs. RHE but no new bands that could be assigned to Cu-N species (a). Therefore, we believe that the NH_3 is near the electrode surface and alters the catalysis of the Cu without directly binding to it. Further, the decrease of current indicates that likely the NH_3 does not act as a proton donor for hydrogen evolution at rates higher than that of water.

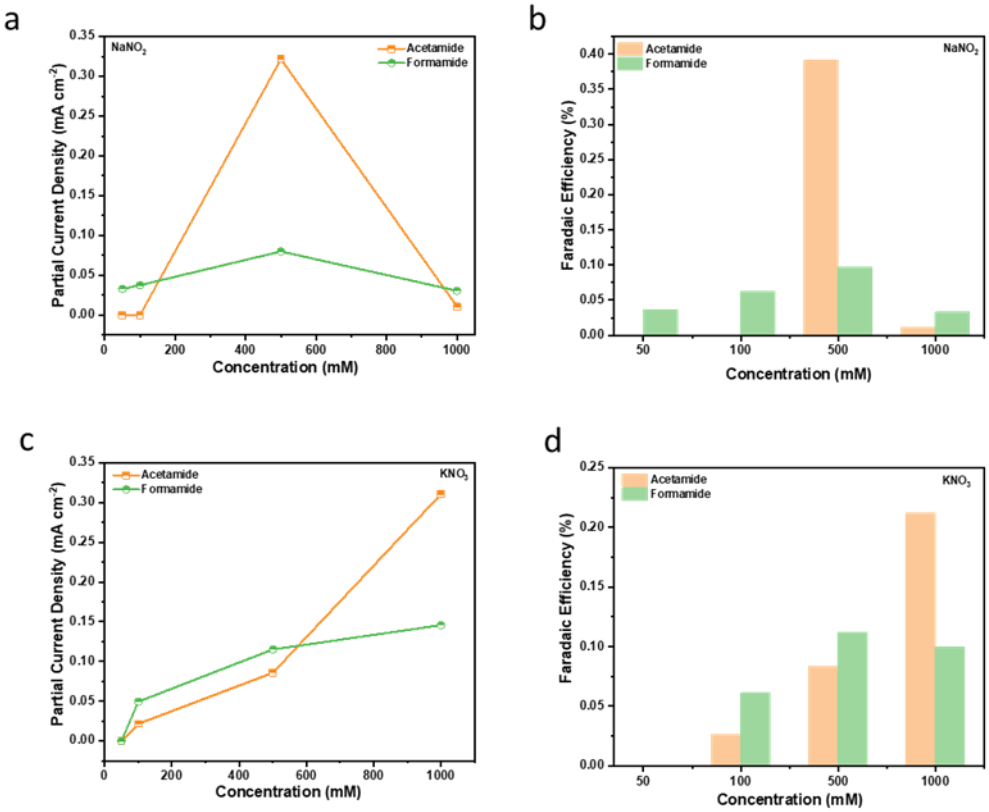

Figure 7.19 - Partial current density (a) and Faradaic efficiency (b) for C-N products from $NaNO_2$ with Cu catalysts at -0.98V vs. RHE) as a function of reactant concentration in the liquid phase. Similarly, we measured the partial current density (c) and Faradaic efficiency (d) for C-N products from KNO_3 with Cu catalysts at -0.98V vs. RHE).

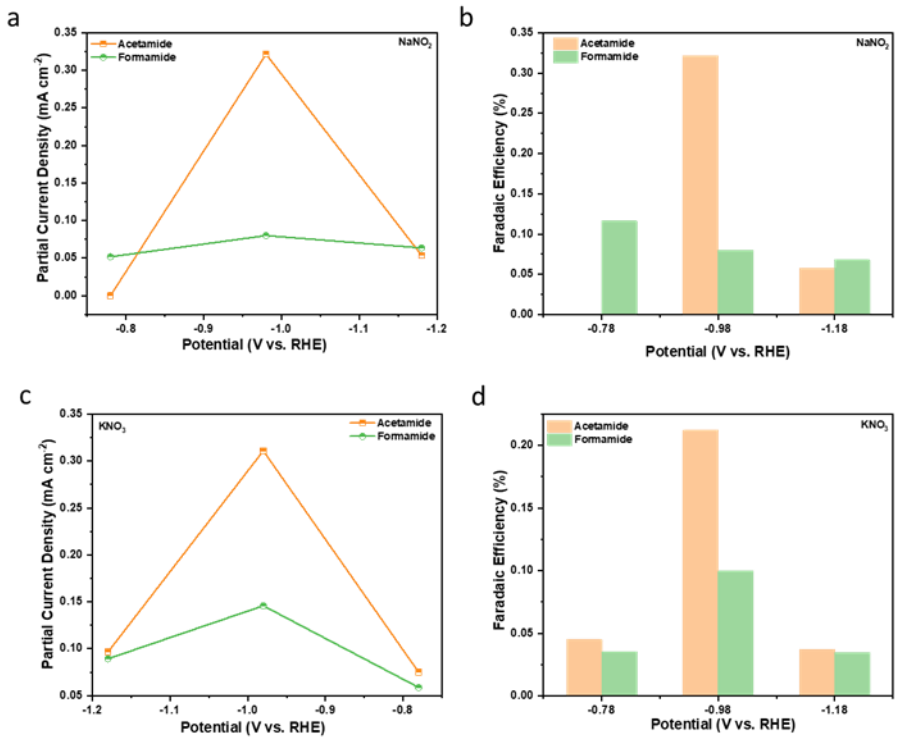

Figure 7.20 - Partial current density (a) and Faradaic efficiency (b) for C-N products from $NaNO_2$ with Cu catalysts at -0.98V vs. RHE) as a function of potential. Further, we measured the partial current density (c) and Faradaic efficiency (d) for C-N products from KNO_3 with Cu catalysts at the above optimized concentration.

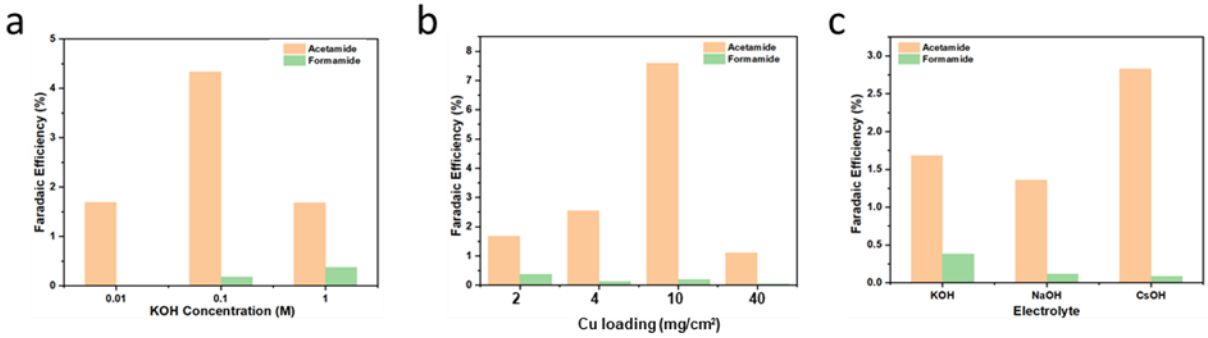

Figure 7.21 - Optimization of reaction conditions with (a) different concentrations of KOH; (b) different amount of Cu nanoparticles; (c) electrolyte (1M) with different cations. The applied potential was -0.98V vs. RHE for this round of experiments.

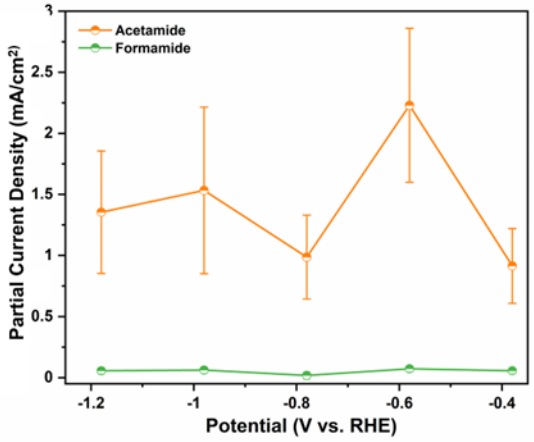

Figure 7.22 - Partial current density for acetamide and formamide corresponding to the Faradaic efficiency at each potential in figure 3.6 in the main text.

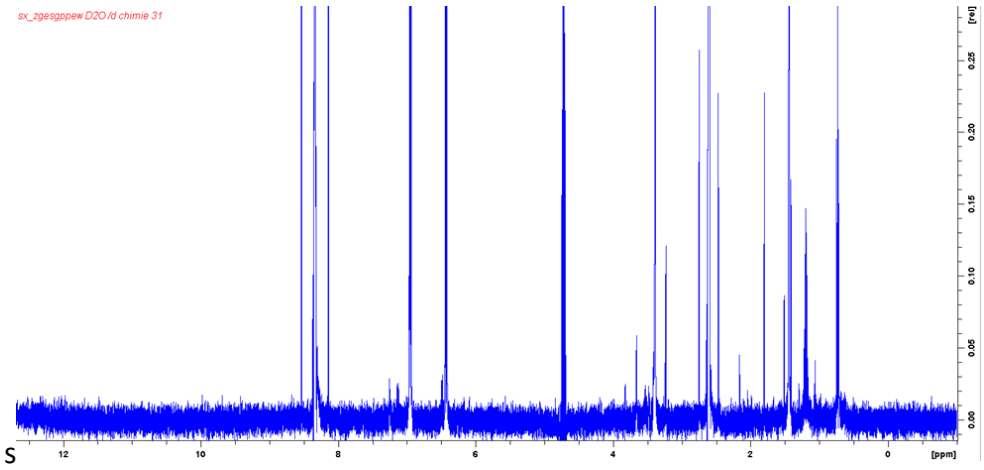

Figure 7.23 - NMR spectrum under open circuit potential. 50 mM formate was added to 0.3 M NH_3 + 1M KOH for 1 hour and the solution probed afterwards. No formamide or acetamide could be detected.

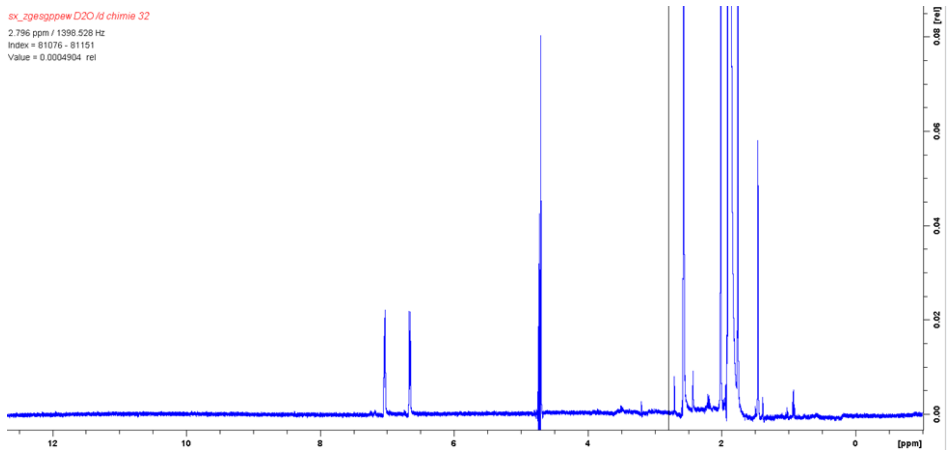

Figure 7.24 - NMR spectrum under open circuit potential. 50 mM acetate was added to 0.3 M NH_3 + 1M KOH for 1 hour and the solution probed afterwards. No formamide or acetamide could be detected.

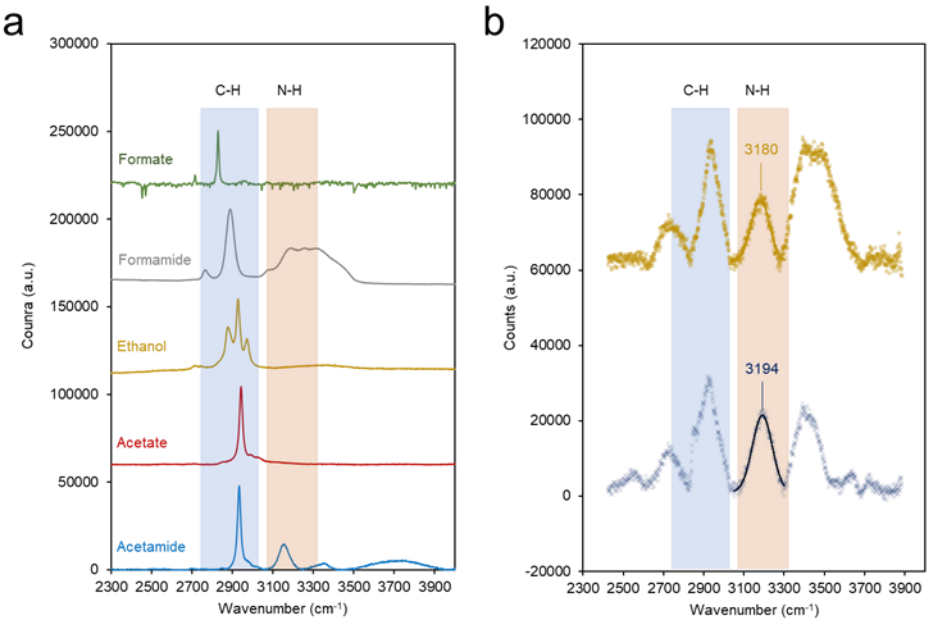

Figure 7.25 - Raman spectra of several standards (a). C-H stretches are situated around 2900 cm^{-1} and N-H stretches are located around 3100-3200 cm^{-1}. Post electrolysis solutions were drop cast on a roughened Ag foil as a surface enhanced Raman substrate and their spectra taken with a 514 nm laser. Electrolysis with ^{14}N revealed a 3194 cm^{-1} band (b) matching that of acetamide. The N-H band of the solution using ^{15}N was situated at a lower frequency, 3180 cm^{-1} (c), as expected from the isotope shift.

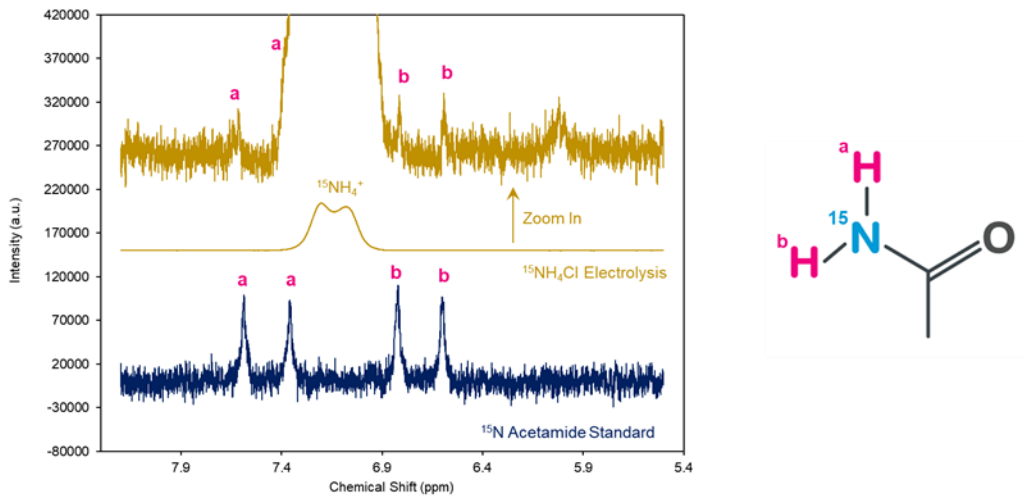

Figure 7.26 - HNMR spectra of isotopically labeled acetamide and the NMR spectra of the acidified solution after CO_2 and $^{15}NH_4Cl$ electrolysis. Note: the spectra were acidified to pH 3 to render the peaks corresponding to the amine more apparent.

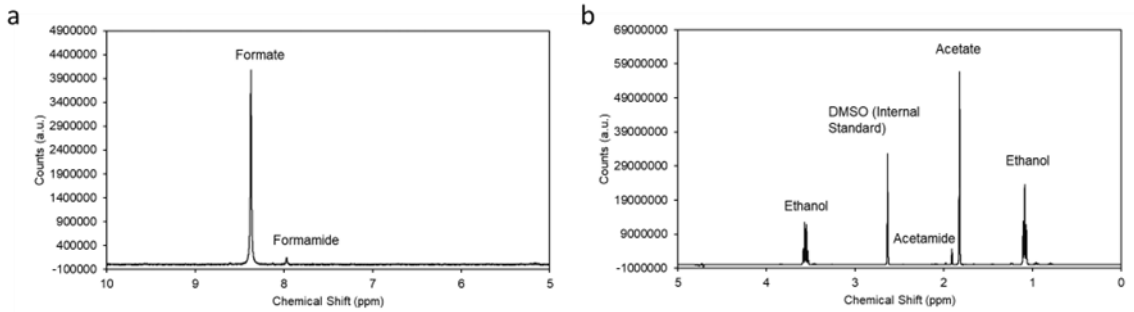

Figure 7.27 - A typical spectrum after CO_2 + NH_3 electrolysis. The spectrum is broken up into two ranges (a, b) as they are zoomed into differently.

Chapitre 8 – Supplementary information for: Electrochemical Formation of C-S Bonds from CO_2 and Small Molecule Sulfur Species

8.1 Materials and methods

8.1.1 Chemical Reagents:

Anhydrous copper chloride ($CuCl_2$, 98%), copper nano powder (Cu, 99.9%), copper (II) oxide nano powder (CuO), hydroxylamine hydrochloride ($NH_2OH{\cdot}HCl$, 99%) were purchased from Alfa Aesar. Sodium hydroxide (NaOH, 98%) and sodium sulfite ($NaSO_4$, 98%) were acquired from Sigma-Aldrich. Potassium hydroxide was obtained from Macron fine chemicals. Copper (I) oxide was purchased from thermos scientific. Sodium dodecyl sulfate (SDS, 100%) was purchased from Mallinckrodt. All chemicals were used without further purification. Copper sulfide (Cu_2S) was purchased from Sigma Aldrich (200 mesh).

8.1.2 Catalyst Preparation:

Cu_2O catalysts were synthesized by a simple wet chemistry method according to the reference.[1] 1 mL of 0.1M $CuCl_2$ was added into 95.5 mL deionized (DI) water, then 2mL of 1M NaOH solution was added into the above solution under stirring. After 10 s, 0.87g SDS was added into the above mixture with vigorous stirring to make the powder solve into the solution. Then 3.5 mL of 0.2M $NH_2OH{\cdot}HCl$ was injected into the above mixture and was shaken for 10 s. The mixture was centrifuged to obtain the precipitates after 12 h aging, and washed with water and ethanol three times, respectively. Finally, the precipitates were dried in a vacuum oven for 12h, and the powder was labeled as sample C. This was the primary catalyst used for electrocatalytic measurements

For sample A to H, the synthesis steps are similar to sample C, except for different volumes of DI water and $NH_2OH{\cdot}HCl$. The volume of DI water and $NH_2OH{\cdot}HCl$ for each sample were listed in Table 8.1.

Table 8.1 - The volume of DI water and $NH_2OH{\cdot}HCl$ for the synthesis different Cu_2O/CuO samples:

	DI water (mL)	$NH_2OH \cdot HCl$ (mL)
A	95.5	1.5
B	94.5	2.5
C	93.5	3.5
D	92.5	4.5
E	91.5	5.5
F	90.5	6.5
G	87.5	9.5
H	91	7.5 (adjust to pH 7)

8.2 Characterizations:

Ex-situ X-ray diffraction (XRD) patterns were collected with a Malvern PanAlytical Empyrean 3 diffractometer with a Cu Kα radiation source (λ = 1.5418 Å) and a PIXcel^{3D} detector in 1D mode operated in Bragg Brentano (θ-θ) geometry, using iCore and dCore optics with automatic slits set at 10 mm irradiated length and a collection time of 1h. In contrast, a Mo-source was used for *in operando* measurements due to its higher penetration, high intensity and compressed pattern which allow to measure all peak of interests in a static configuration. They were collected on a Malvern PanAlytical Empyrean 3 diffractometer with a Mo Kα radiation source (λ = 0.7093 Å) with focusing mirror optics and a GaliPIX^{3D} detector in static 1D mode with 30 s integration time, and an omega angle of 12,5°. Scanning electron microscope characterization was conducted on FEI Quanta 450 Environmental Scanning Electron Microscope (FE-ESEM). Transmission electron microscopy (TEM) images were obtained with a JEOL JEM-2100F FEG-TEM, operating on 200 kV.

8.2.1 Electrochemical measurements and product qualification:

Electrochemical measurements were performed by Bio-Logic SP-200 Potentiostat (BioLogic Science Instruments, France) in a gas diffusion electrode (GDE) – based reaction cell with a three-electrode framework. Carbon rod and Ag/AgCl were utilized as the counter electrode and reference electrode, respectively. All potentials measured in this work were converted to RHE by the following equation:

E (vs RHE) = E (vs Ag/AgCl) + 0.197 + (0.0591 x pH)

The working electrode was prepared as below: 10 mg catalyst was added into the mixture of 100 µL DI water and 300 µL ethanol. After 10 mins ultrasonication, 100 µL homogeneous catalyst ink was dropped onto the carbon cloth (GDL-CT (W1S1009, Fuel Cells Etc.) and dried in air for 1h. 1M KOH with different concentrations of $NaSO_4$ was used as the electrolyte. Linear sweep voltammetry was measured in the range of 0 ~ 1.18 V (vs. RHE), with a sweep rate of 5 mV s^{-1}. Potentiostatic electrolysis was performed at room temperature and pressure, with a steady CO_2 gas flow which is 10 mL min^{-1}. The GDE cell was sealed and connected with gas chromatography (GC, SRI 8610C) to qualify the gas products in flow mode. A thermal conductivity detector (TCD) was used for analyzing H_2, and flame ionization detector (FID) was used for quantifying CO and CH_4. After 30 mins reaction, the electrolyte was collected and analyzed by ^1H nuclear magnetic resonance (NMR, Bruker AVII 500) and confirmed by ^{13}C NMR (NMR, Bruker AVANCE II 700). 400 µL liquid product was mixed with 400 µL D_2O, with dimethyl sulfoxide (DMSO) as an internal standard. The yield of gas and liquid products were calculated based on the calibration curves of the standard samples. The Faradaic efficiency (FE) was calculated by the following formula: $\varepsilon_{FE} = \frac{\alpha n F}{Q}$

where α is electron transfer number, n is the moles of products, F is the Faraday constant (96485 C mol^{-1}), Q is all the charge passed during the reaction. For FE, partial current density, and product formation rate calculations, the error bars correspond to the standard deviation from three independent measurements.

8.2.2 In-situ Raman spectroscopy

In-situ Raman spectra were collected on Renishaw Invia system with a 633 nm laser. The output powder is 5 mW. Before each experiment, Raman frequency calibration was conducted by measuring a Si wafer (520 nm). A laser line focus module was utilized to obtain spectra by spreading out the laser intensity with approximately 20x lower signal intensity per area. The accumulation time per spectrum was set to 1s and the total signal acquisition time is 60s (average of 60 spectra). An immersion objective (numerical aperture of 0.8) was used to decrease the distance between the laser and the surface of the electrode to a obtain better Raman signal. The

spectra were collected under different potential, range from open circuit potential to -0.98V vs. RHE, with the step of -0.2V.

The reaction cell is similar with electrochemical measurement. The same three-electrode configuration was used for the *operando* Raman measurement; working electrode, counter and reference electrode are the identical. KOH was used as electrolyte, with or without the addition of sulfite. CO_2 or N_2 was fed into the reactor, with flow rate of 10 mL min^{-1}.

8.2.3 DFT parameters and computational details

Here, three slab structures for copper (100), (110) and (111) were constructed using Atomic Simulation Environment (ASE) [33] and all consisted of $5 \times 5 \times 4$ structures, or 4 layers of 25 atoms. The bottom two layers were fixed to simulate the bulk and the top two layers were free to relax to resemble the surface. 15 Å of vacuum is added in the z direction (perpendicular to the surface) to avoid interaction between periodic images. The Monkhorst-Pack scheme was used for K-points of $4 \times 4 \times 1$. The energy cut-off and the relative cut-off used were 550 and 50 Rydberg, respectively. The force convergence was taken to be 3×10^{-4} $Bohr^{-1}$ Hartree. The exchange correlation functional of Perdew, Burke, and Ernzerhof (PBE) was used.[34] All these parameters were chosen after running convergence and sensitivity tests. DFT calculations are all performed using CP2K code [35] and further computational details are given elsewhere.[36] CO was used as a starting intermediate as it one featured in the CO_2 reduction pathway to higher order products.

To compute energy differences of elementary proton coupled electron transfer (PCET) steps, the computational hydrogen electrode (CHE) model [37] was used. In this model we assume hydrogen gas is at equilibrium with proton and electron and the corresponding potential is 0 V vs. RHE, thus the energy of proton coupled with electron is estimated by half of the energy of hydrogen gas:

$$H^+ + e^- \leftrightarrow \frac{H_{2(g)}}{2} \qquad \text{(Eq. 1)}$$

$E_{H^+ + e^-} = \frac{E_{H_2(g)}}{2}$, @ pH=0 and 1 atm (Eq. 2)

Both SO_3^{2-} and HSO_3^- are adsorbed on the Cu (111), (110) and (100). The adsorption energies are used as predictors for the affinity of the surfaces to both species. The adsorption energies are on Table S2.

Table S3 and Table S4 are the optimized energy of the copper surfaces and absorbed intermediates, respectively.

8.3 Supplementary figures and tables

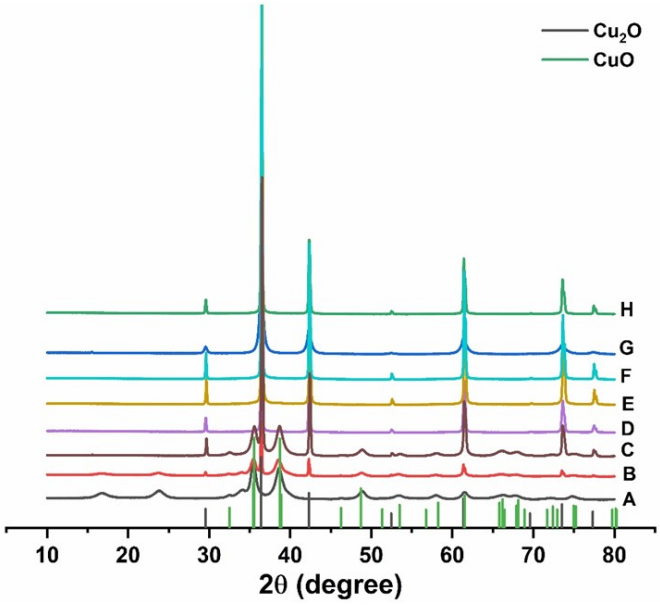

Figure 8.1 - XRD patterns of the catalysts en route to their synthesis. Among them, sample A is CuO, sample B and C are the mixtures of CuO and Cu_2O. Sample D to H are Cu_2O.

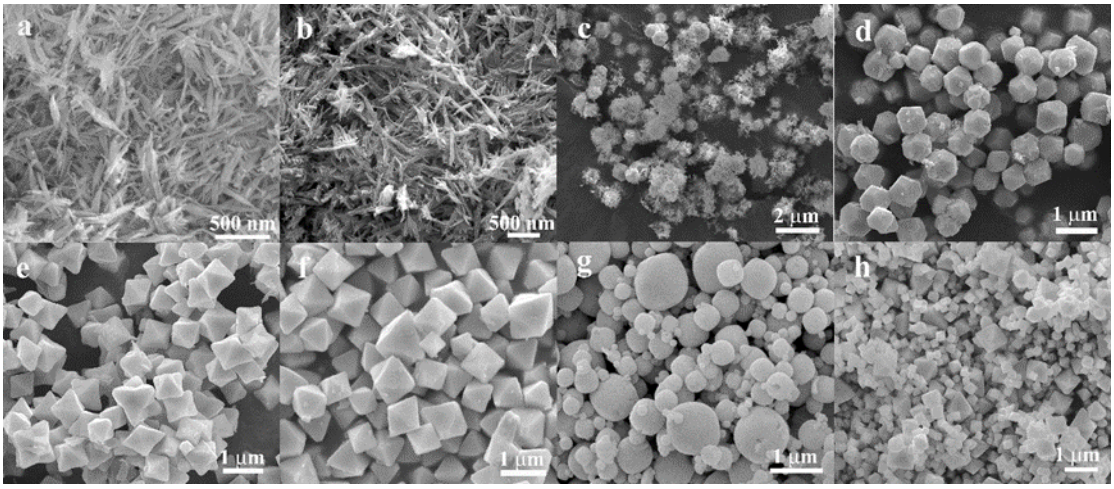

Figure 8.2 - Typical SEM images of different catalysts from samples A to H. (a) nanowire, length is around 400 nm; (b) nanowire; (c) sample C, the aggregation of nanowire to form shaped nanoparticles, with a small amount of incompletely grown truncated octahedron crystals; (d) truncated octahedra, the size is around 600 nm; (e) short hexapods, with small amount of octahedra, ~1 µm; (f) octahedra with uniform size; (g) sphere, size distributed from 100 nm to 1 µm; (h) octahedra with a large size distribution from 200 nm to 700 nm.

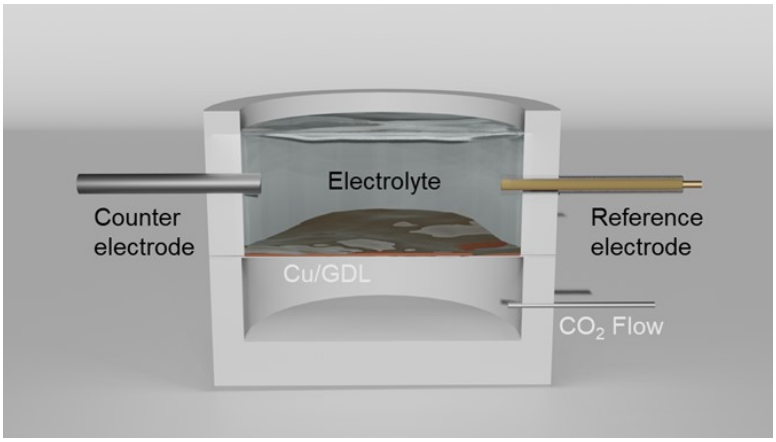

Figure 8.3 - Gas diffusion half-cell with minimal electrolyte volume used for electrochemical screening experiments. Isolating the counter electrode with an anion-exchange membrane did not lead to a measurable difference in C-S product formation in control experiments.

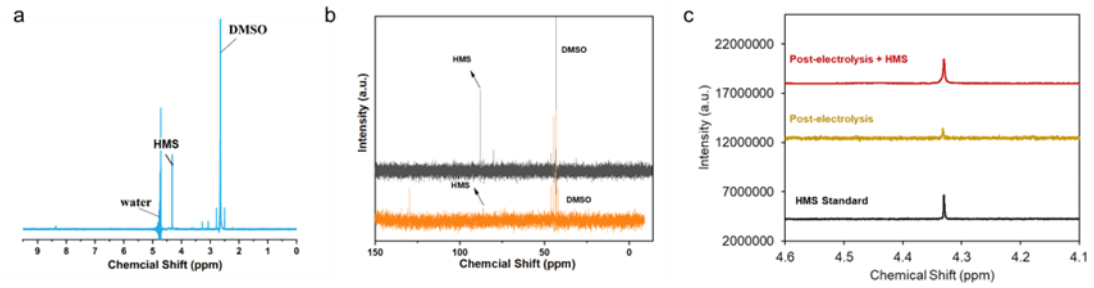

Figure 8.4 - HNMR spectrum of hydroxymethanesulfonate (HMS) standard sample (Concentration: 20 mM in 1 M KOH) (a) and comparison of ^{13}C NMR spectra of the post-electrolysis solution (orange) and HMS standard (gray) (b). HMS is also confirmed by adding a small quantity (approx. 5 mM) of HMS to a post-electrolysis solution (at -0.68V vs. RHE) and illustrating that no new peaks arise (c).

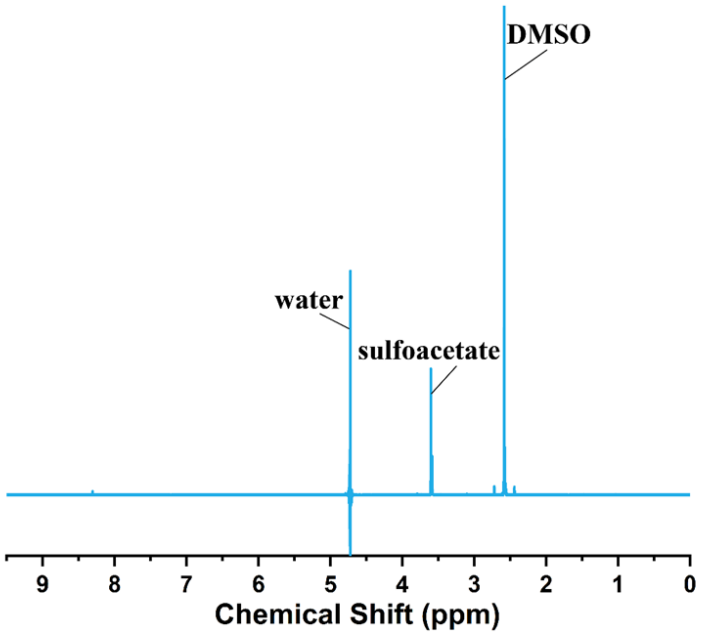

Figure 8.5 - NMR spectrum of sulfoacetate standard sample (Concentration: 20 mM in 1 M KOH).

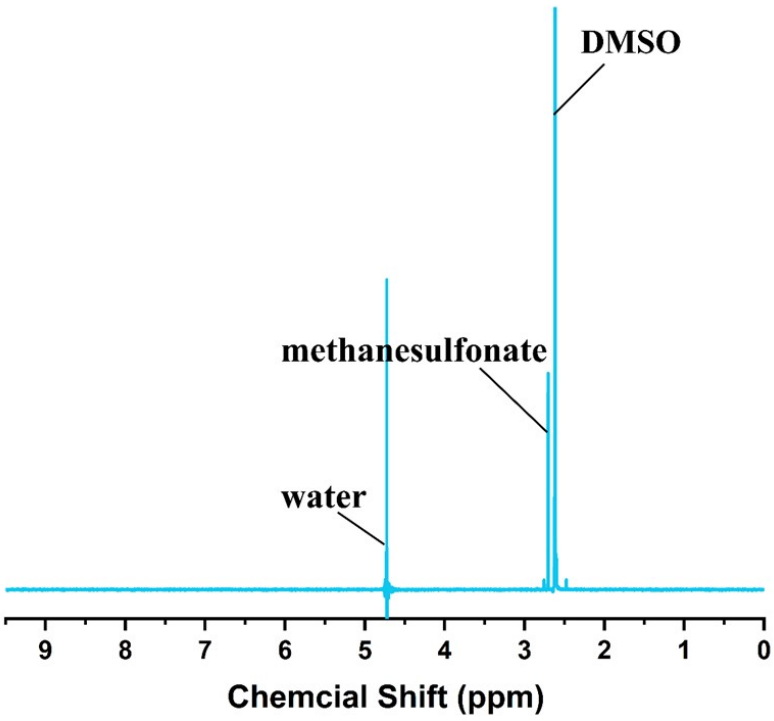

Figure 8.6 - NMR spectrum of methanesulfonate standard sample (20 mM in 1 M KOH).

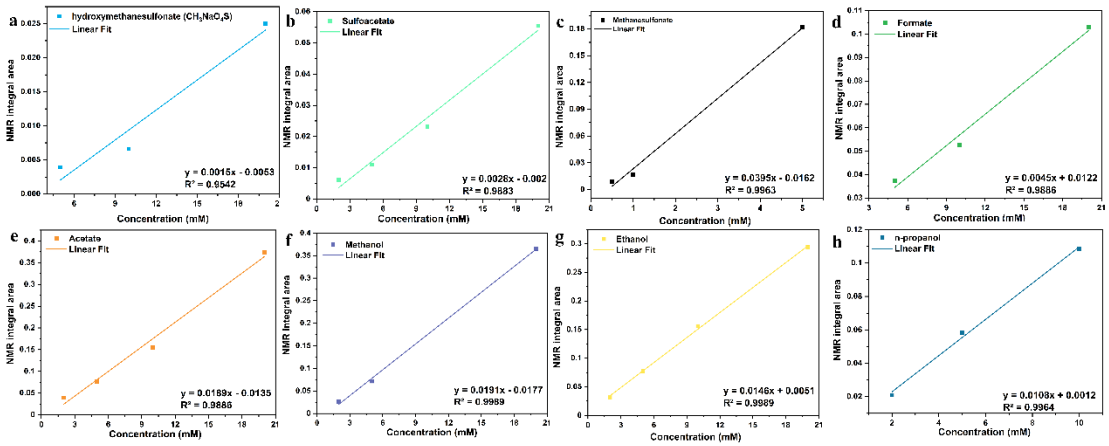

Figure 8.7 - NMR calibration curves. (a) hydroxymethanesulfonate (HMS); (b) sulfoacetate (SA); (c) methanesulfonate (d); formate (e) acetate; (f) methanol; (g) ethanol; (h) n-propanol.

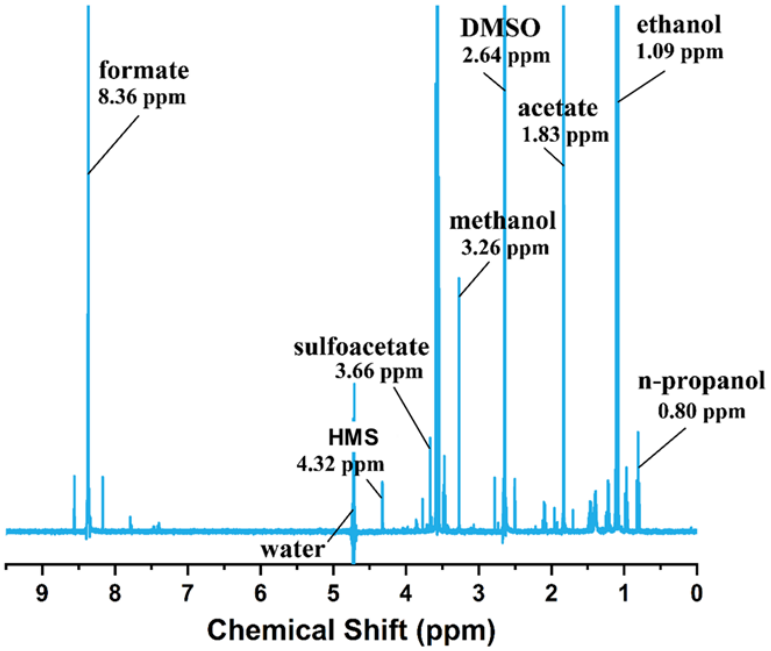

Figure 8.8 - NMR spectrum of the liquid after potentiostatic electrolysis. Sample C was chosen as electrocatalyst with 1 M KOH, 0.2 M $NaSO_4$ as electrolyte. CO_2 gas flow rate is 10 mL min^{-1}, the applied potential is -0.78V (vs. RHE). DMSO was used as the internal standard (2.64 ppm). Hydroxymethanesulfonate (4.32 ppm, HMS) and sulfoacetate (3.66 ppm) are the product with C-S bond, the liquid products also contain formate (8.36 ppm), ethanol (1.09 ppm), acetate (1.83 ppm), methanol (3.26 ppm), and n-propanol (0.80 ppm).

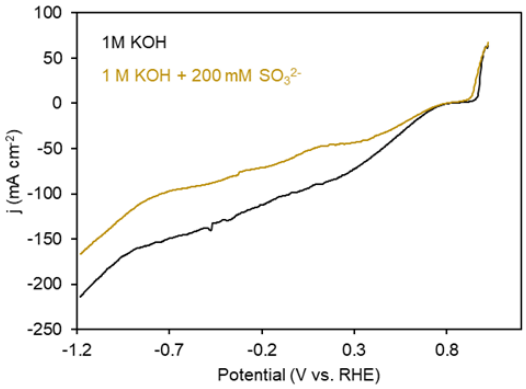

Figure 8.9 - LSV of the Cu catalyst (sample C) under a N_2 atmosphere in the presence and absence of SO_3^{2-}.

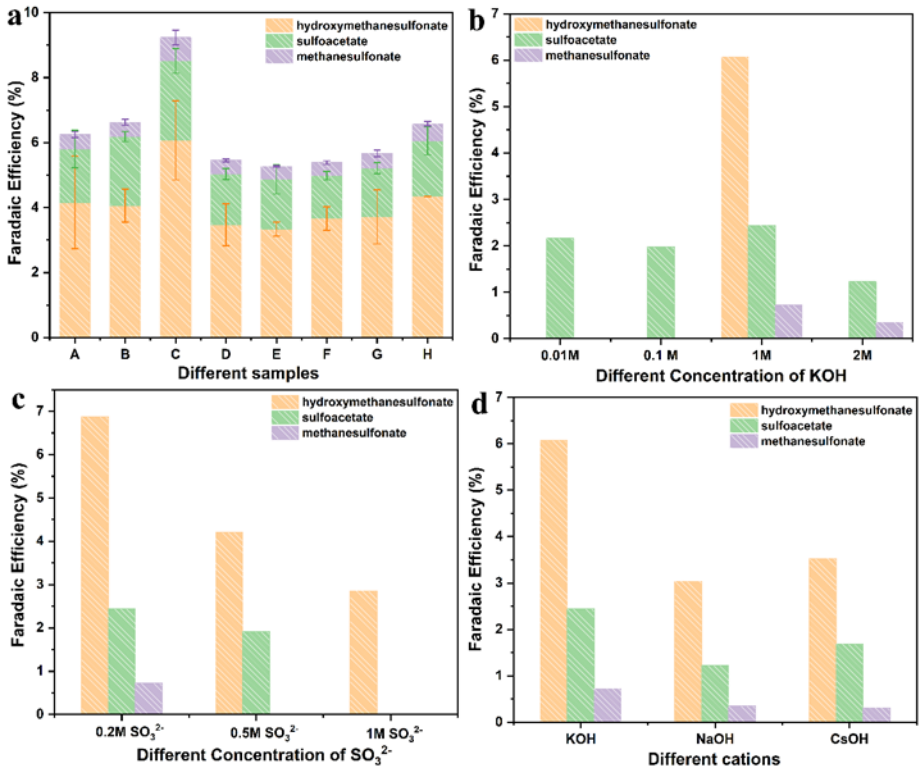

Figure 8.10 - Optimization of reaction conditions for HMS formation. (a) FE with different Cu samples in 1 M KOH, 0.2 M Na_2SO_3, at -0.78 V. Sample C shows the highest FE among these eight catalysts. (b) Catalytic performance of sample C in different electrolytes. All the concentration is 1M. (c) Production of HMS in different concentrations of Na_2SO_3. Sample C shows the highest FE for HMS in 1M KOH, 0.2 M Na_2SO_3. Different amounts of KOH (0.1 M, 2

M) are also used as the electrolyte to adjust the pH, but no signal of HMS was observed in NMR spectrum. Loading amount has also been changed (10 mg, 15 mg, 25 mg), C-S bonds product was obtained only when the amount of sample C is 25 mg, which is 2.39, it's similar to 10 mg, thus in the following electrochemical experiment 10 mg sample C, 1 M KOH, 0.2 M Na_2SO_3 was chosen as the reaction condition.

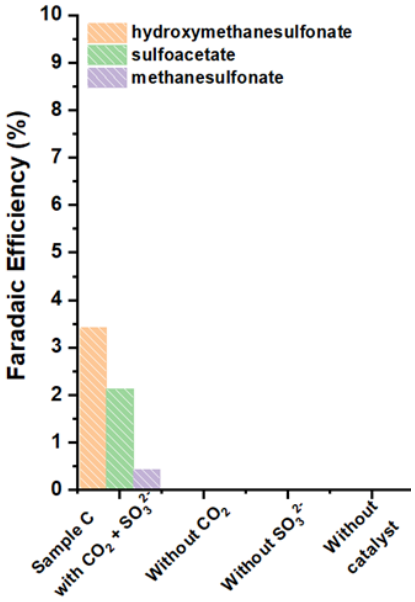

Figure 8.11 - Control experiments omitting key aspects of the electrocatalytic system in otherwise identical conditions (1 M KOH electrolyte, -1.18 V vs. RHE).

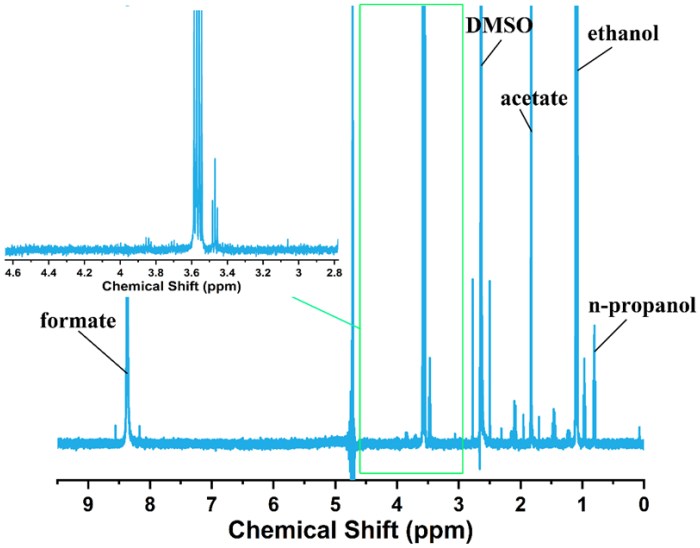

Figure 8.12 - NMR spectrum of a control experiment performed without sulfite. Potentiostatic electrolysis was conducted with sample C in KOH + CO_2 flow under -0.78V. No HMS or sulfoacetate or MS were observed in the NMR spectrum, which proves that SO_3^{2-} is the sulfur source. Formate, acetate, ethanol, and n-propanol were observed as the final liquid products.

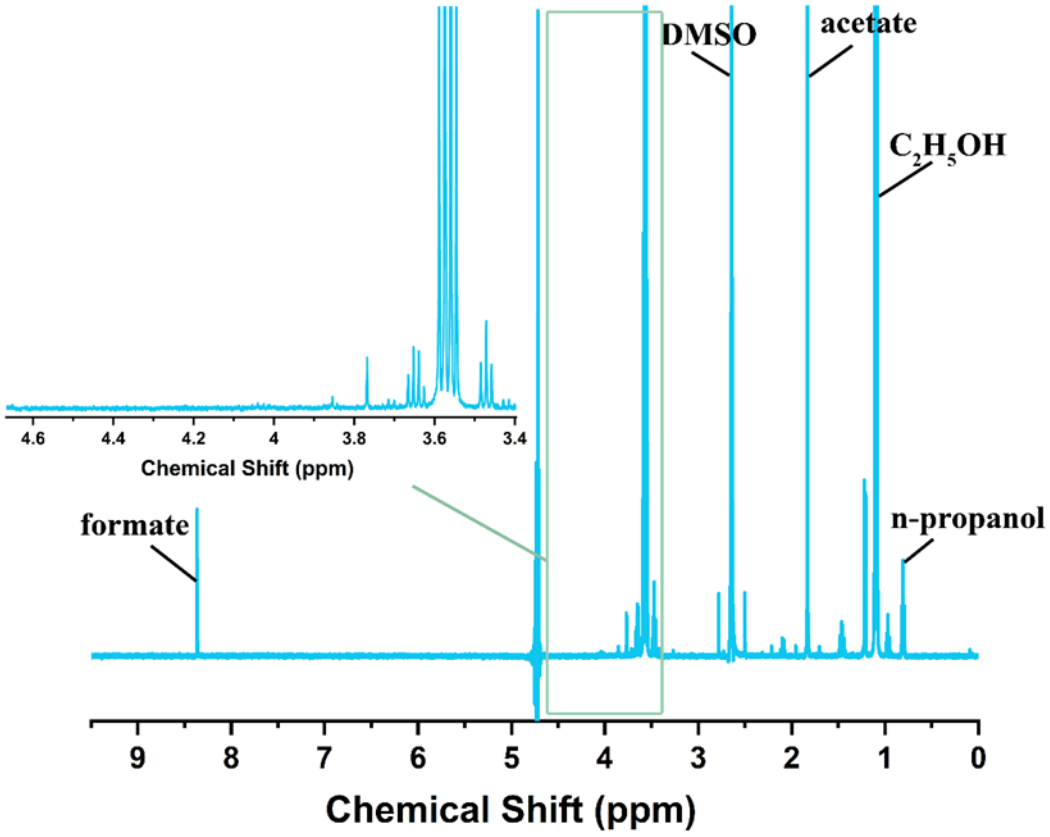

Figure 8.13 - NMR spectrum of a control experiment without sample C. The carbon cloth was used as the electrode, 1 M KOH, 0.2 M sulfite was used as electrolyte. The electrolysis was conducted under -0.68V, with continuous CO_2 flow. No product with C-S bonds was observed. Formate, acetate, ethanol, n-propanol and methanol were observed after the reaction.

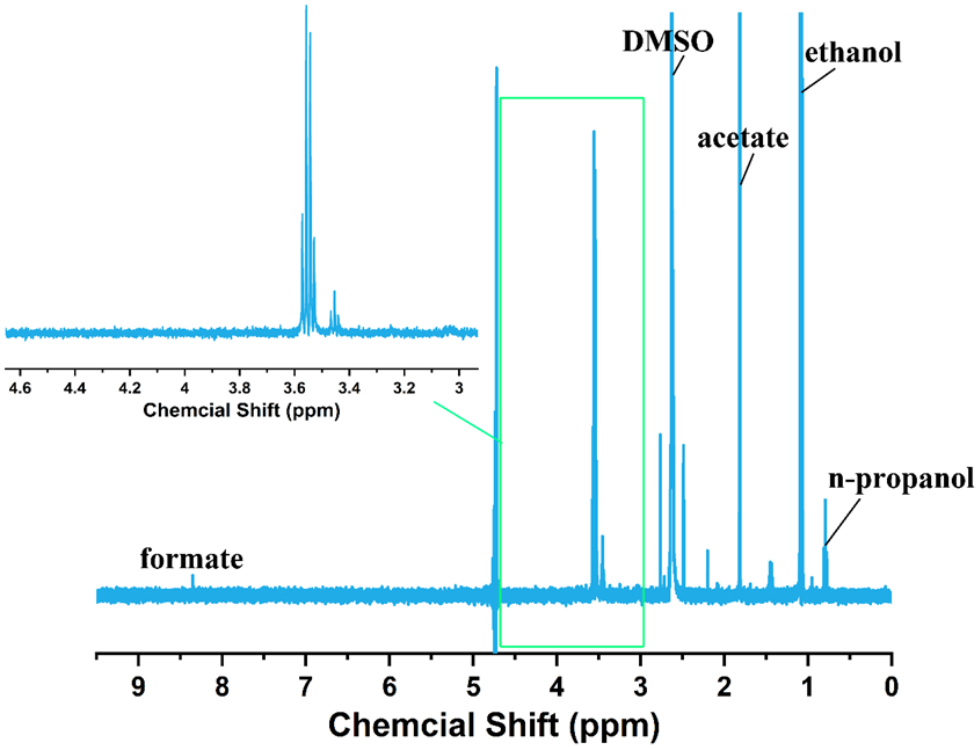

Figure 8.14 - NMR spectrum of control experiment without CO_2. Sample C was used as the electrocatalyst, 1M KOH + 0.2 M Na_2SO_3 was used as the electrolyte, a stable, continuous N_2 gas flow was used instead of CO_2. The flow rate is 10 mL min^{-1}. No C-S bond compounds are obtained after electrolysis, formate, acetate, ethanol and n-propanol are produced by slight decomposition of the carbon cloth electrode.

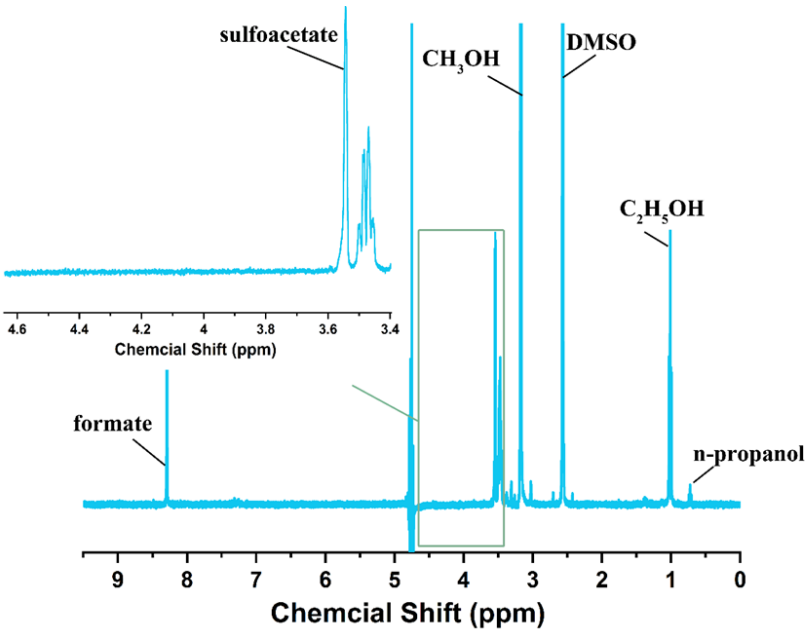

Figure 8.15 - Formaldehyde (HCHO) was used as substrate instead of CO_2 to conduct electrolysis in 1M KOH + 0.2 M Na_2SO_3 at -1.08 V. No signal of HMS was observed, which suggests that HCHO is not the intermediate for HMS formation.

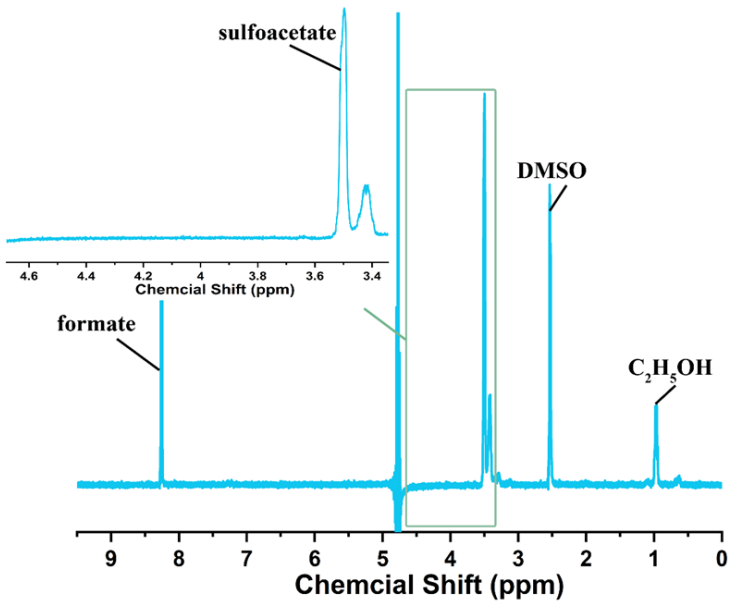

Figure 8.16 - Formate was used as a precursor to replace CO_2 to conduct electrolysis. The reaction condition is the same as the CO_2RR reaction, in which the electrolyte is 1 M KOH + 0.2 M sulfite, under -0.68 V. There is no HMS obtained after reaction, which suggests that formate is not the intermediate for HMS production.

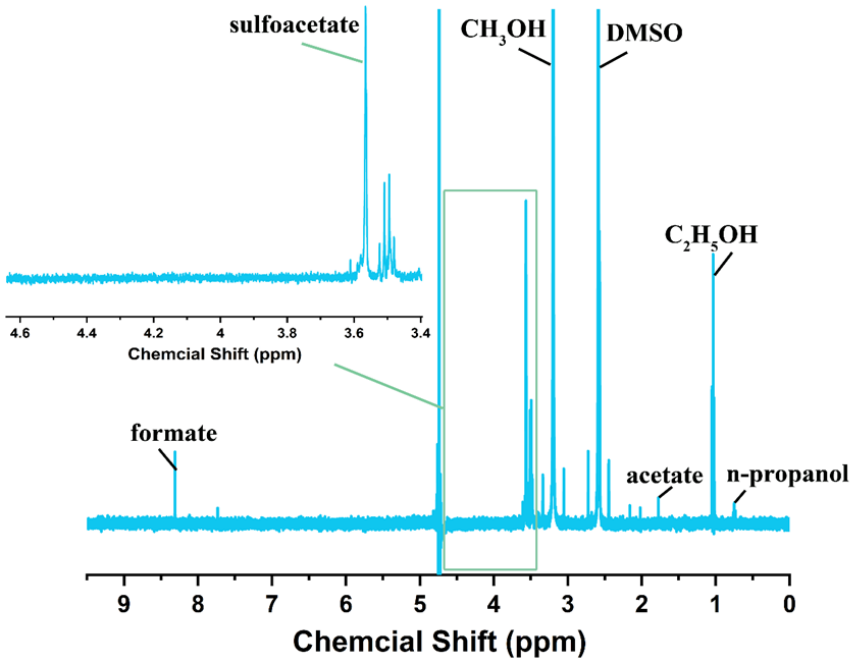

Figure 8.17 - Methanol was used as a precursor instead of CO_2 for C-S coupling. The reaction condition is the same as the CO_2RR reaction, in which the electrolyte is 1 M KOH + 0.2 M sulfite, under -1.08 V. Also, there is no CH_3NaO4S obtained after reaction, which suggests that HMS is not the intermediate for HMS production.

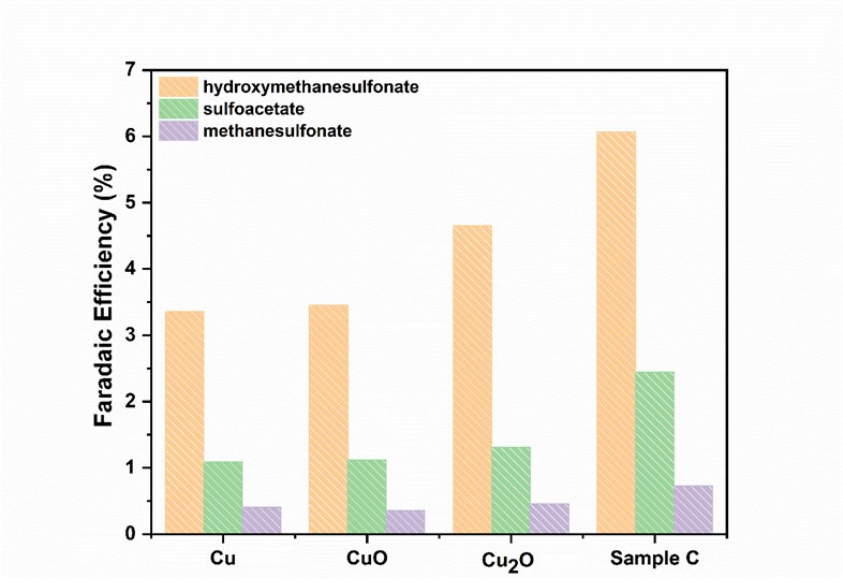

Figure 8.18 - Comparison of C-S product formation under optimized conditions (-0.68 V vs. RHE, 1 M KOH, 200 mM SO_3^{2-}) of synthesized and commercially purchased Cu catalysts.

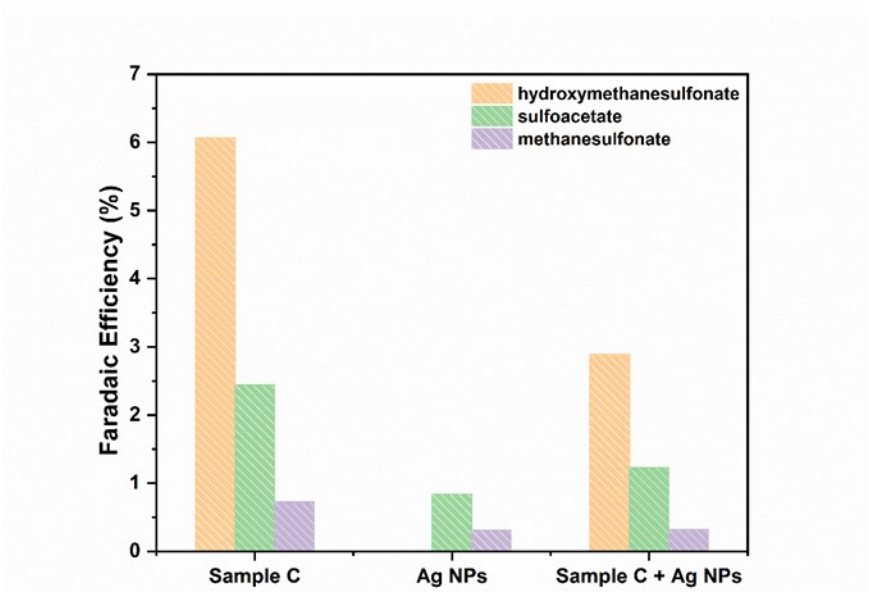

Figure 8.19 - HMS and SA formation with Ag nanoparticles (NPs) used as catalysts under the optimized conditions of 0.2 M Na_2SO_3, 1.0 M KOH and -0.68V_{RHE}.

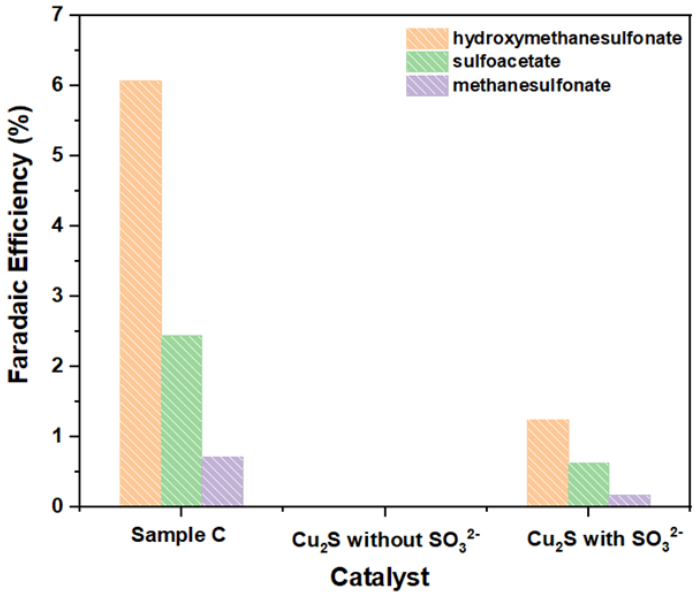

Figure 8.20 - Faradaic efficiencies for C-S products from Cu_2S (commercially purchased and processed under identical conditions) at -0.68V vs. RHE indicates that the sulfide from the Cu2S cannot significantly contribute to C-S product generation in the absence of SO_3^{2-}, and when SO_3^{2-} is present (0.2 M), C-S product formation is measurable, but lower than the oxide-derived catalysts.

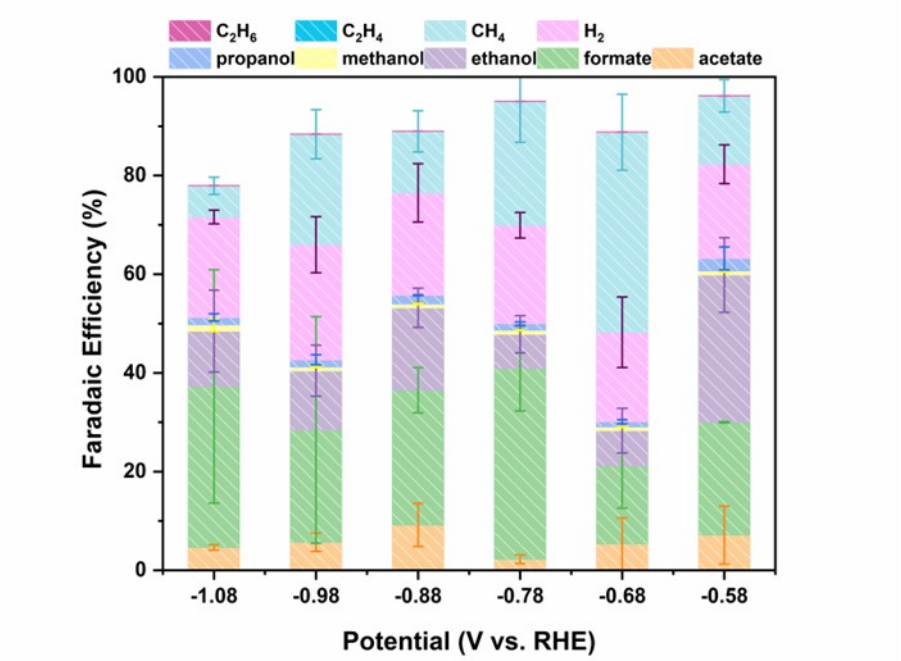

Figure 8.21 - Faradaic efficiencies for the electrochemical system in the absence of SO_3^{2-}, using the optimized catalyst C in 1.0 M KOH and CO_2 flow.

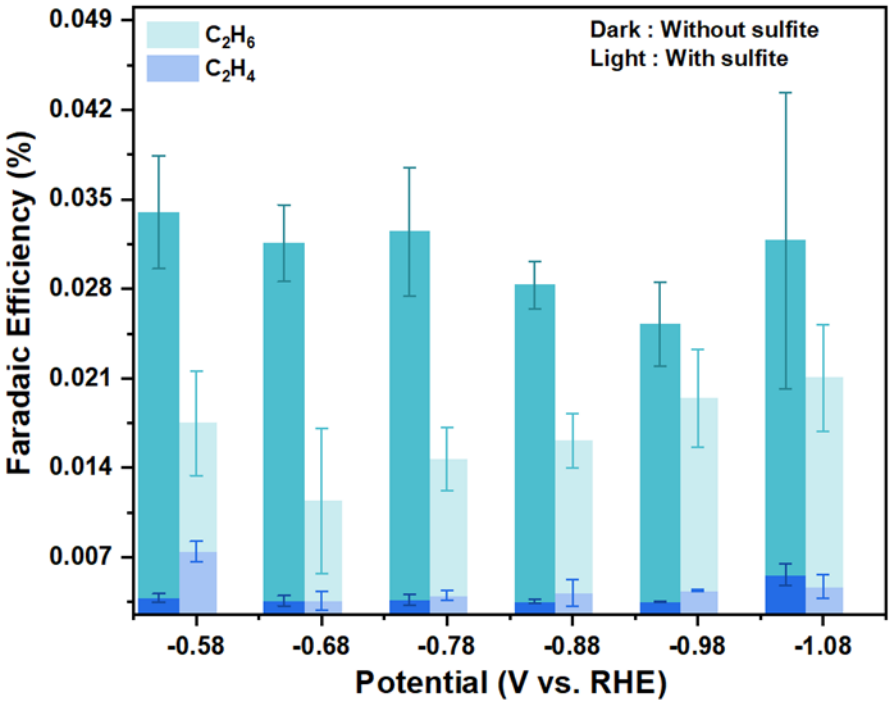

Figure 8.22 - Faradaic efficiencies for ethane and ethylene (sample C) in the presence and absence of 200 mM SO_3^{2-} in the 1.0 M KOH electrolyte.

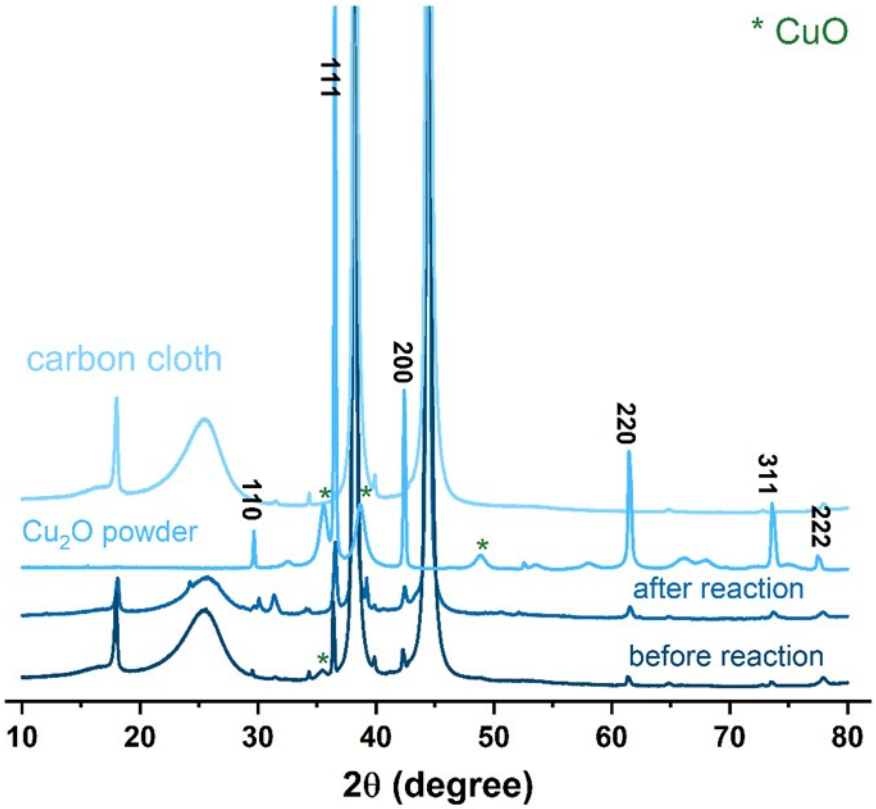

Figure 8.23 - XRD patterns of sample C powder, bare carbon cloth, working electrodes with sample C before and after reactions. Comparing these patterns, sample C electrode shows the peaks at 18.01 °, 25.28 °, 38.27 °, and 44.41 ° belong to graphite. Before reaction, sample C contain Cu2O (JCPDS card no. 05-0667), (110), (200), (220), (311) and (222) signals were observed at 29.55°, 42.30°, 61.34 °, 73.53 °, and 77.32 °, respectively. Besides these peaks, 2θ values of 35.54o, 38.71o, and 48.72o could be indexed to (11-1) and (111), (20-2) planes of CuO (JCPDS card no. 48-1548). After the reaction, peaks of graphite and Cu_2O are observed, likely from the surface oxidation of the Cu and peaks of CuO are missing.

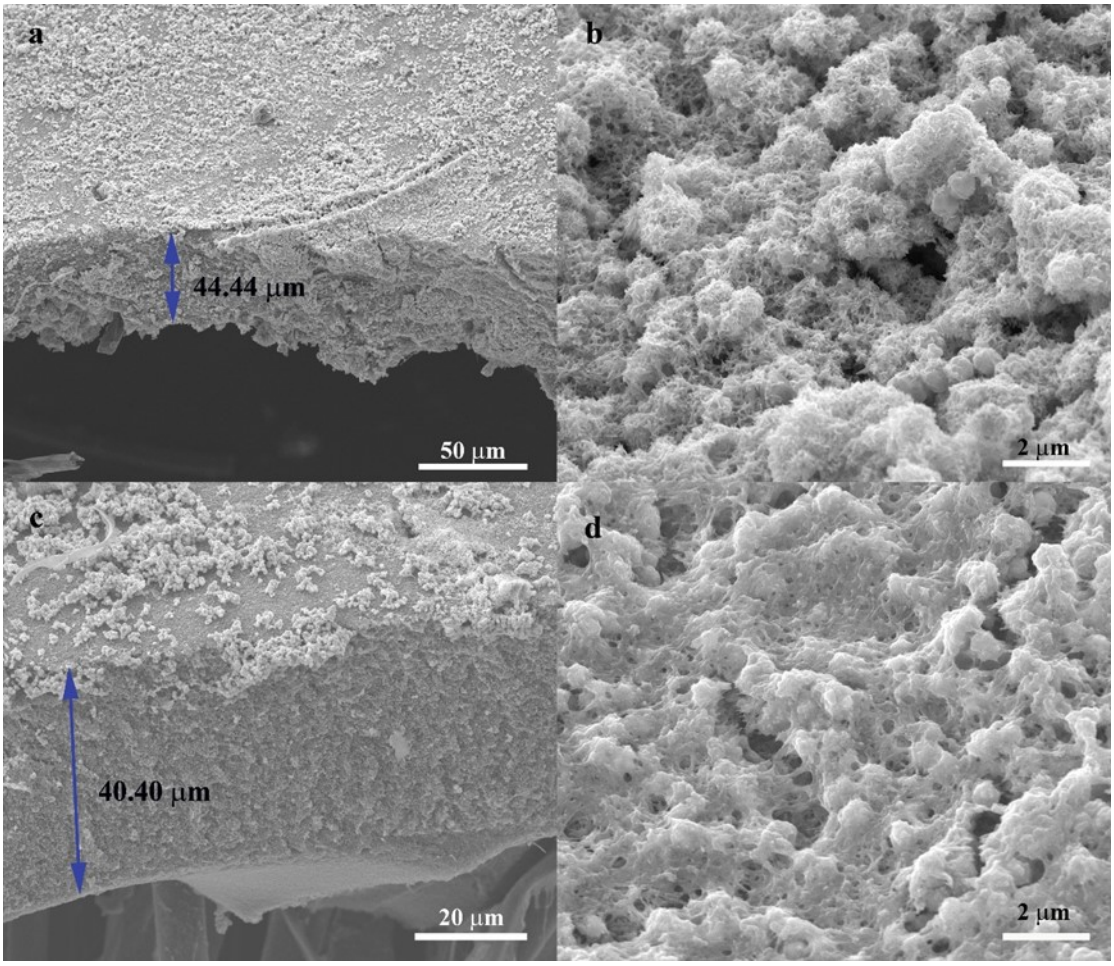

Figure 8.24 - SEM images of sample C. (a) cross session and (b) electrode surface before reaction; (c) cross section and (d) electrode surface after the reaction (-0.78 V for 1 hr).

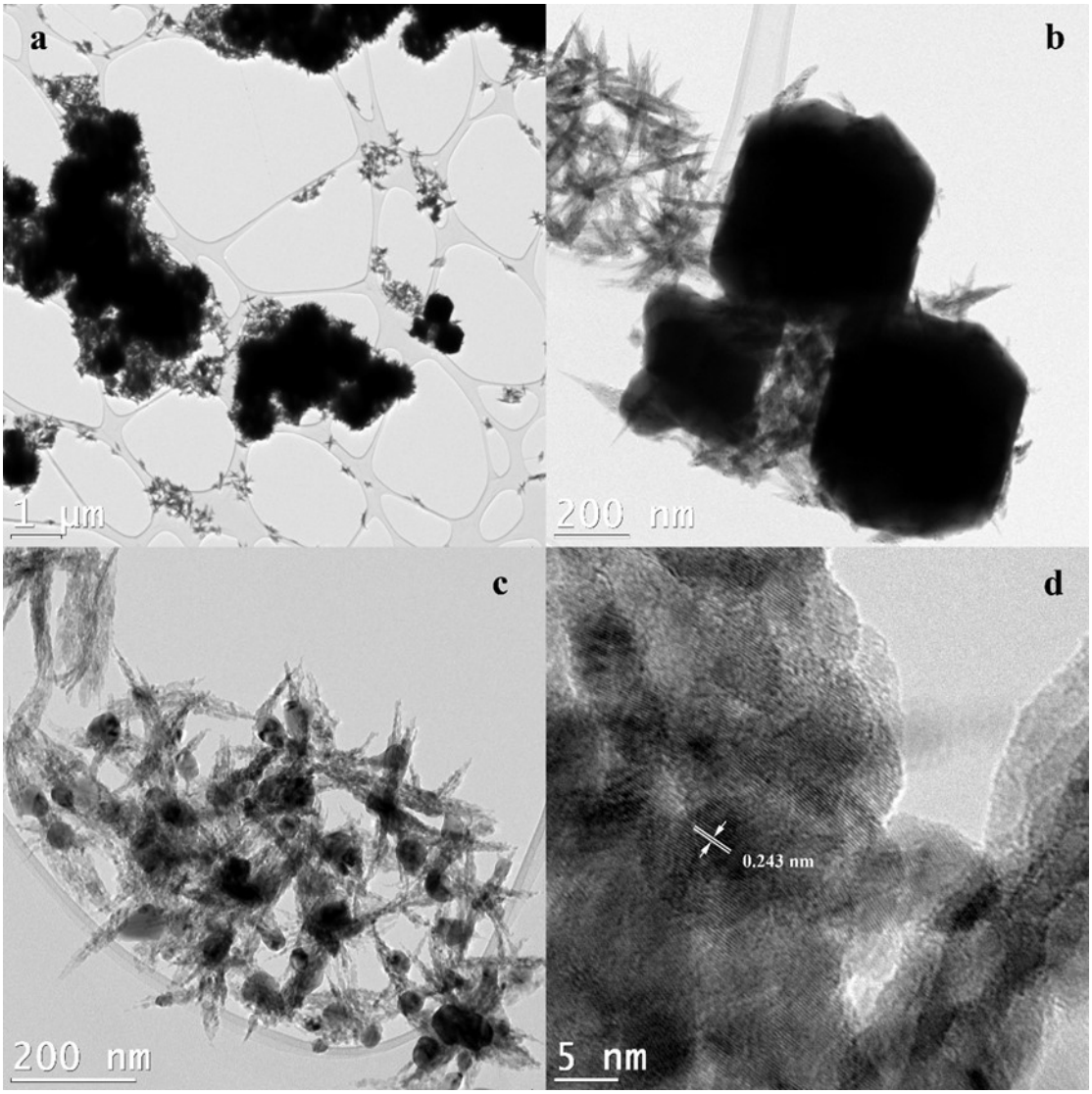

Figure 8.25 - (HR)TEM images of sample C powder before the reaction. The morphology is consistent with SEM results, which is the mixture of incompletely grown octahedron and sea urchin particles constituted by short nanowires. Nanowires are formed by the aggregation of small nanoparticles. The lattice distance of 0.243 nm could be attributed to the Cu_2O (111) planes.

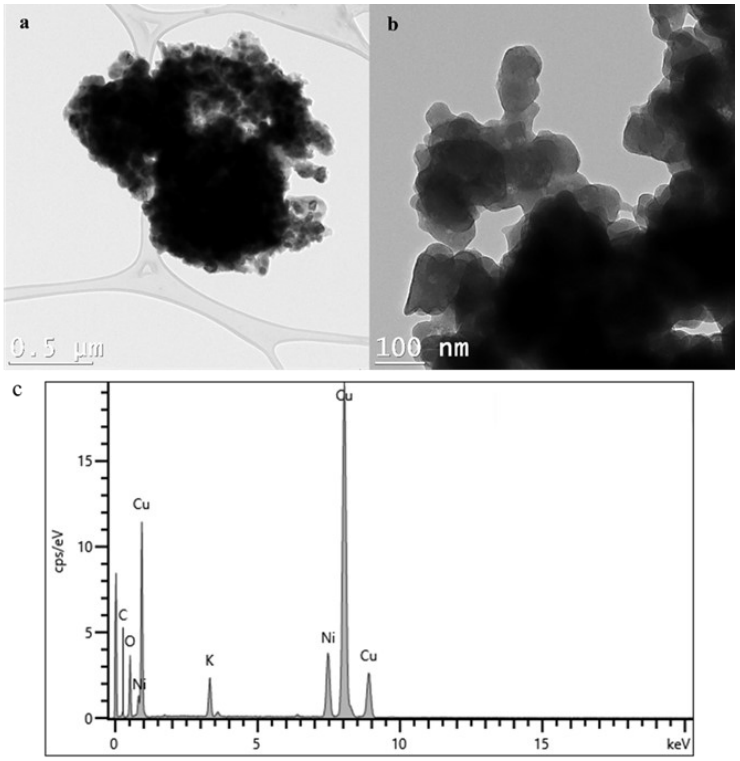

Figure 8.26 - (HR) TEM images of sample C after catalysis. The samples are scratched from carbon cloth electrode onto a Ni TEM grid. Short nanowire-like features disappear, and small nanoparticles are further aggregated to form larger nanoparticles (a, b). EDS analysis (c) shows that Cu and O are the main elemental components of the particles. Traces of S can occasionally be seen at 2.5 keV.

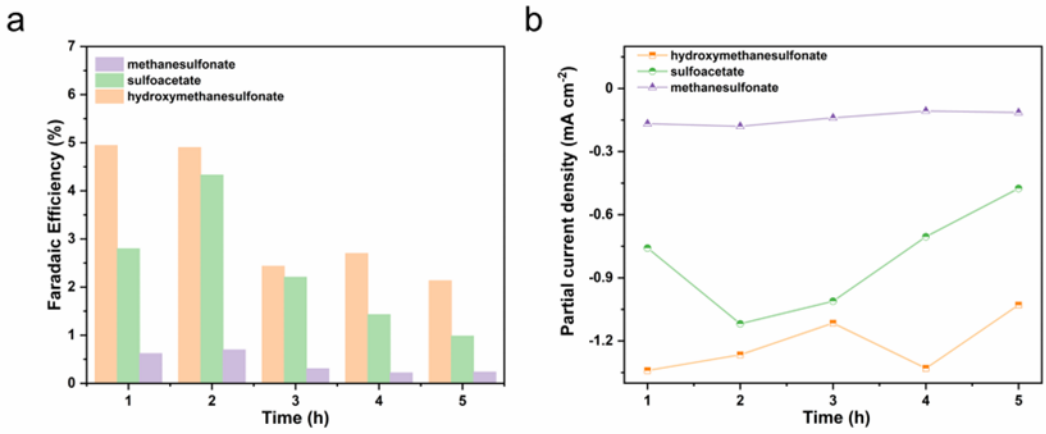

Figure 8.27 - FE (a) and partial current density (b) of C-S bond products over consecutive electrolysis runs with the same catalyst at -0.68 V.

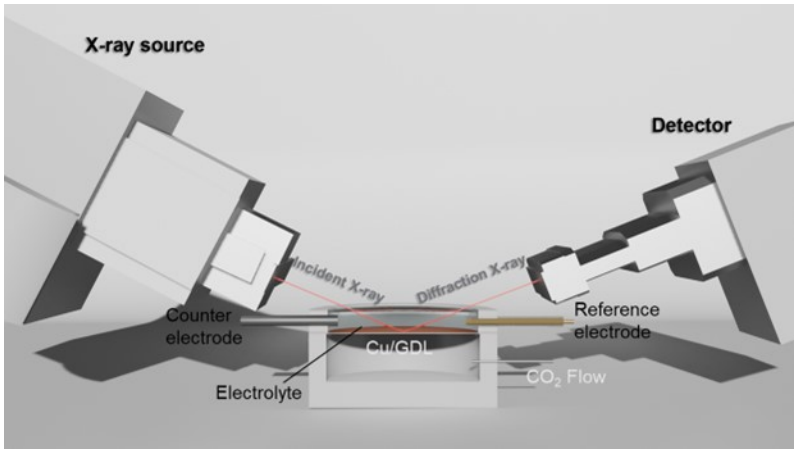

Figure 8.28 - Schematic of operando XRD measurement setup.

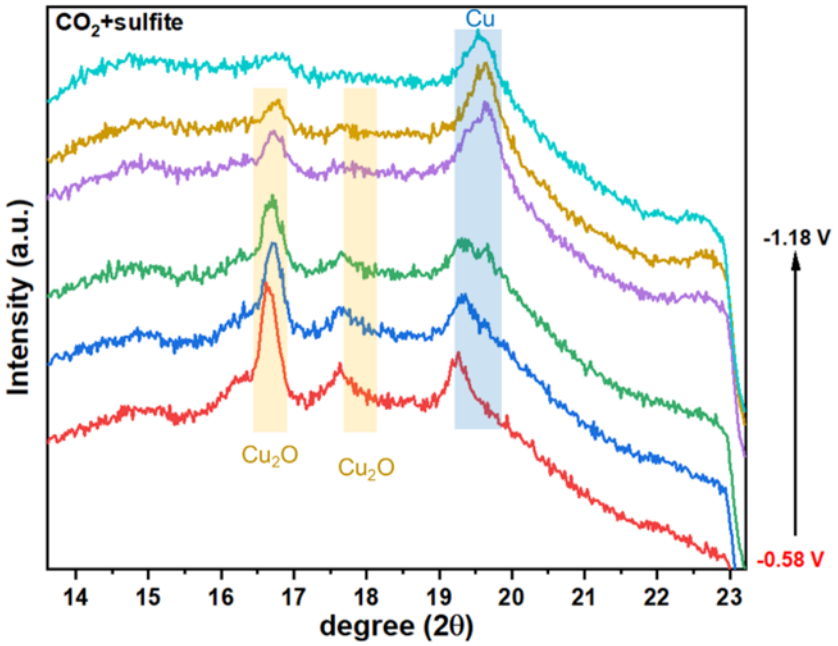

Figure. 8.29 - Operando XRD experiments (Mo source) carried out as a function of applied potential (vs. RHE) with 1 minute per potential. Within 5-6 minutes of reducing potential, the Cu2O (16.5^{o} and 18^{o}) and CuO (19.5 ^{o}) largely disappear, and metallic Cu is the main crystal phase observed.

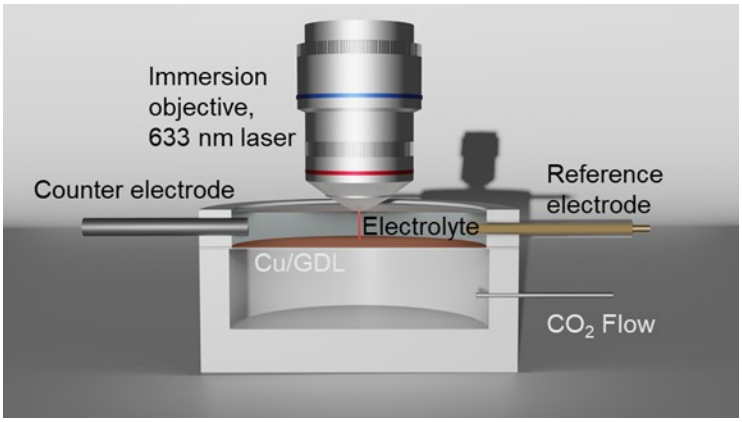

Figure 8.30 - Reaction cell used for operando Raman measurements under CO_2 flow and a gas diffusion layer as a working electrode.

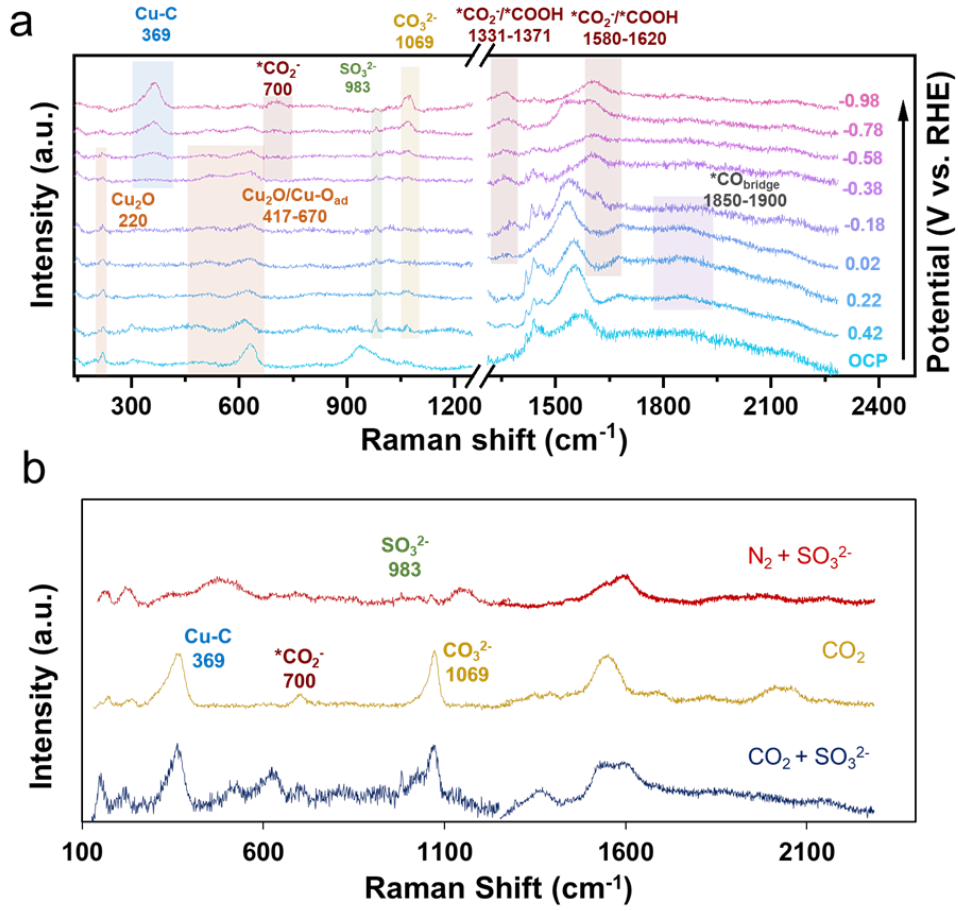

Figure 8.31 - High and low-frequency Raman spectra under typical C-S coupling conditions (a) and comparison of Raman spectra of the Cu catalyst at -0.78VRHE with CO_2 only and SO_3^{2-} only (b).

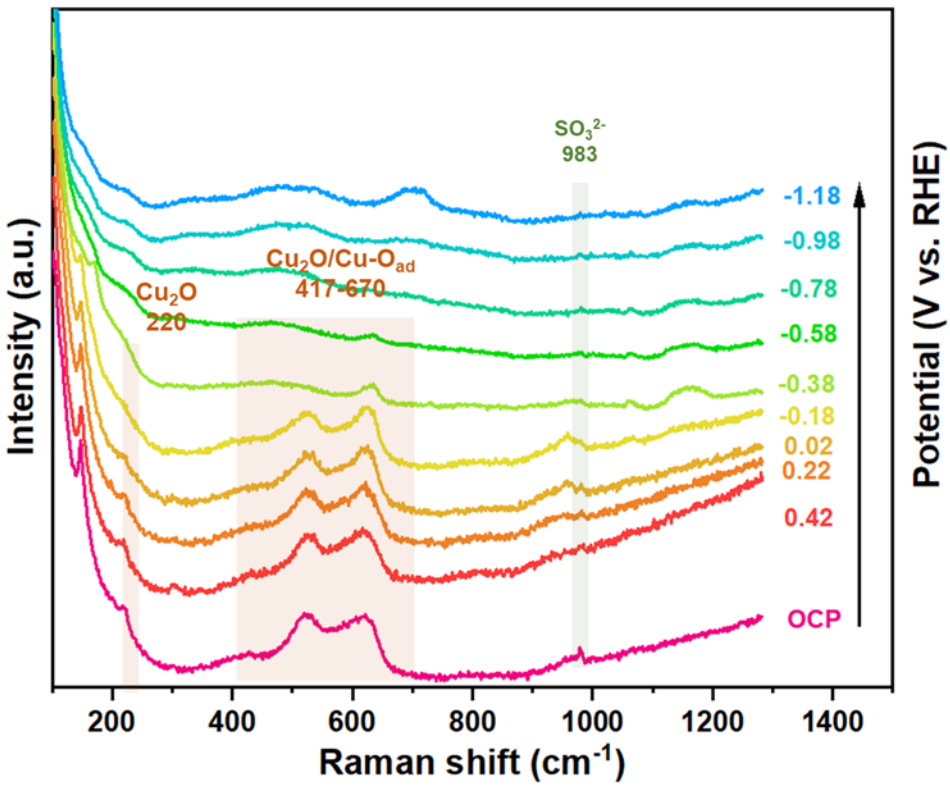

Figure 8.32 - Potential dependent Raman spectra under N_2 using a 1 M KOH + 0.2 M SO_3^{2-} electrolyte.

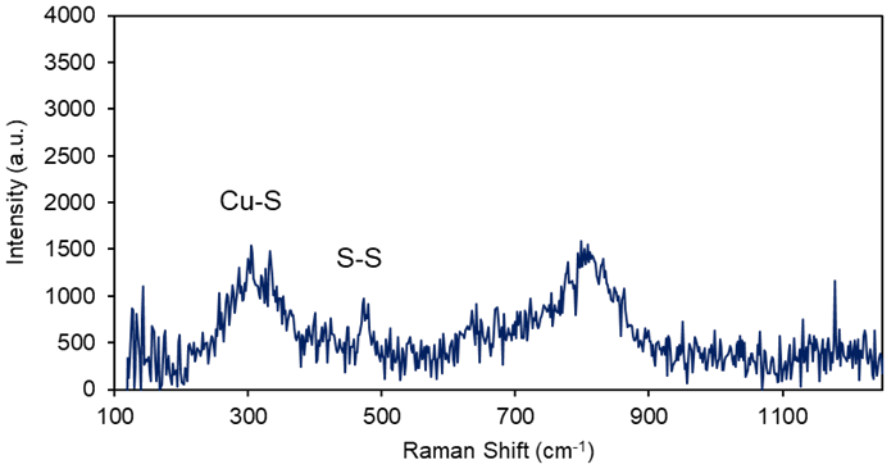

Figure 8.33 - Raman spectrum of commercial Cu_2S powder with a characteristic S-S stretch around 474 cm^{-1}.[1-3]Kor

Table 8.2 - Adsorption energies of two sulfur compounds and three copper surfaces

Adsorption energies	100	110	111
SO_3^{2-}	0. 87 eV	0.49 eV	1.54 eV
HSO_3^-	1.74 eV	1.48 eV	2.02 eV

Table 8. 3 - Energies of optimized copper slabs

Size	Surface	Energy (a.u)	Energy (eV)
$\mathbf{5 \times 5 \times 4}$	100	-4811.5	-130926
$\mathbf{5 \times 5 \times 4}$	111	-4811.7	-130933
$\mathbf{5 \times 5 \times 4}$	110	-4810.9	-130910

Table 8.4 - Energies of adsorbed intermediated on Cu (100) and isolated molecules

Intermediate	Energy (a.u)	Energy (eV)	Position
CO	-4833.226	-131517	Bridge C*
CHO	-4833.793	-131532	Bridge C*+Top O*
COH	-4833.784	-131532	Hollow C*
CHOH	-4834.371	-131548	Bridge C*
CH_2O	-4834.400	-131549	Bridge C* + Bridge O*
CH_2OH	-4834.985	-131565	Top C* + Top O*
HMS (-)	-81.649	-2221.74	Deprotonated (-1 charge)
HMS	-82.348	-2240.77	Protonated (0 charge)
SO_3CO	-4891.507	-133103	Stays connected
$HOSO_2CO$	-4892.113	-133119	Disconnected, unfinished
SO_3COH	-4892.088	-133119	C*, connected

SO_3CHO	-4892.103	-133119	CHO on top of SO_3 by C* on S
SO_3CHOH	-4892.697	-133135	C*, connected
SO_3CH_2OH	-4893.314	-133152	SO3*, CH2OH lifted up
SO_3CH_2O	-4892.699	-133135	CH2O desorbs, unfinished
$HOSO_2CH2OH$	-4893.872	-133167	Desorbs, Unfinished
$HOSO_2CHO$	-4892.700	-133135	Separated
$HOSO_2CHOH$	-4893.264	-133151	C*, Connected
$HOSO_2COH$	-4892.659	-133134	C*
HSO_3	-58.929	-1603.53	Individual molecule
$H2SO_3$	-59.452	-1617.74	Individual molecule
HSO_3+CHOH	-4893.272	-133151	Surface coupling
HSO_3+ COH	-4892.689	-133135	Surface coupling
SO_3+CHOH	-4892.692	-133135	Surface coupling
SO_3+COH	-4892.108	-133119	Surface coupling

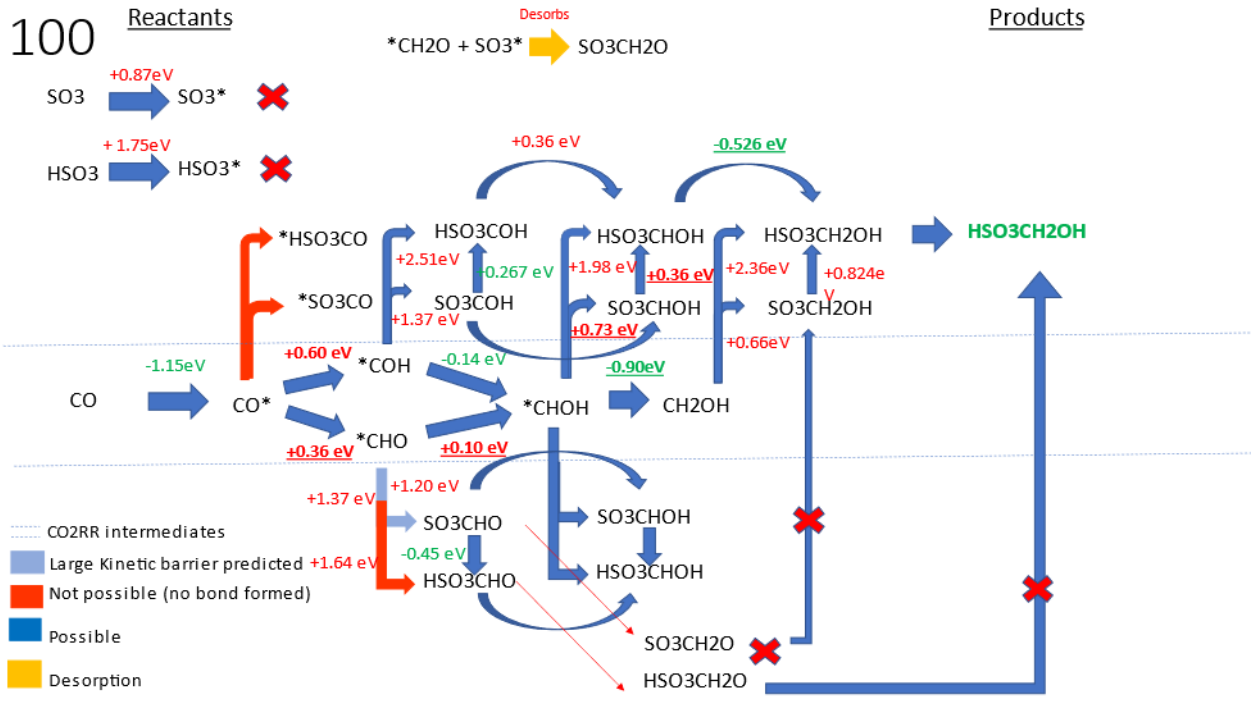

Figure 8.34 - Reaction pathway from CO to HMS on Cu (100) including energy barriers, adsorption energy. Underlined values show the most promising pathway. Red values are positive while green values are negative energy barriers.

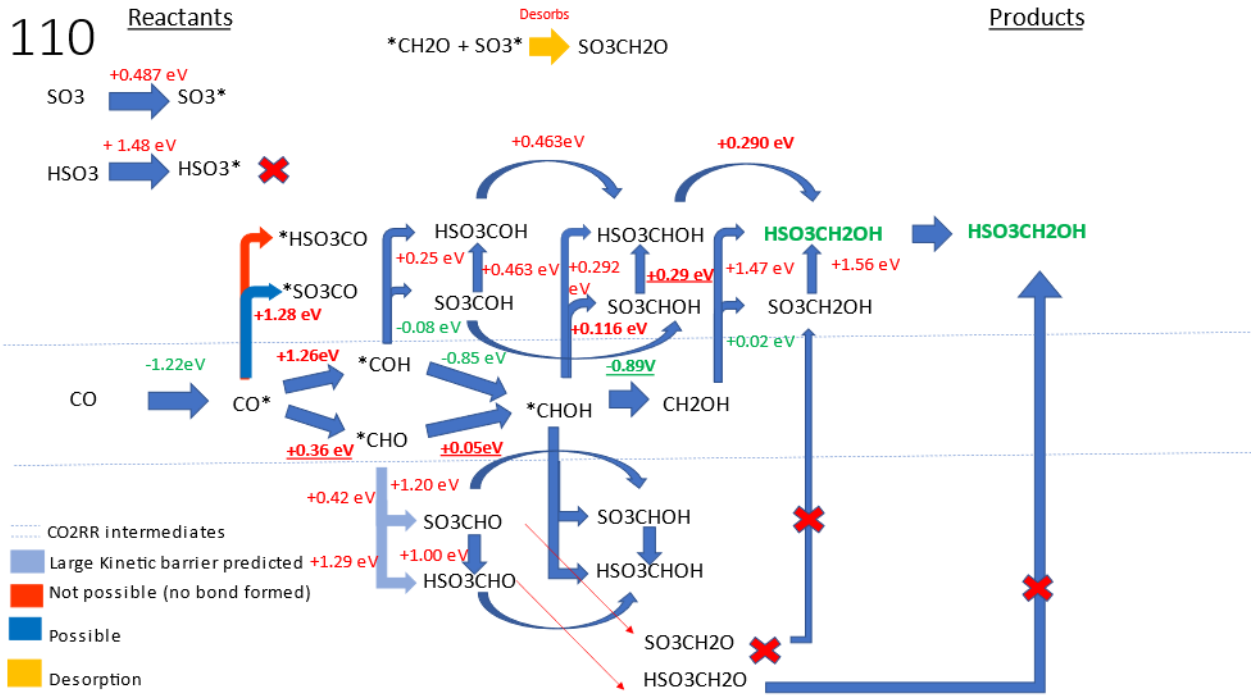

110 energy barrier and pathway

Figure 8.35 - Reaction pathway from CO to HMS on Cu (110) including energy barriers, adsorption energy. Underlined values show the most promising pathway. Red values are positive while green values are negative energy barriers.

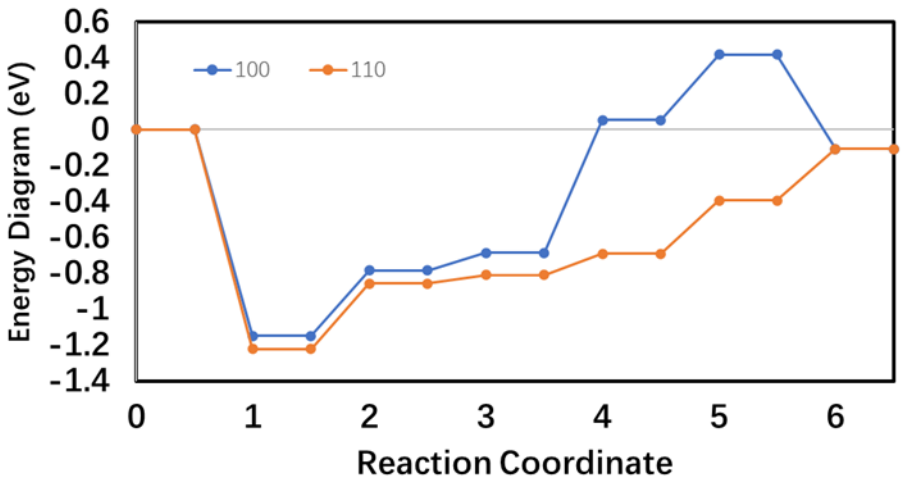

Figure 8.36 - Comparing energy diagrams of (100) and (110).

Table 8.5 - Comparison of energy barriers and coupling barriers of Cu(100) and Cu(110).

	Main coupling step	**Coupling barrier**	**RDS barrier (eV)**	**RDS**
100	SO_3+CHOH	0.740	**0.74**	SO3+CHOH => SO3CHOH
110	SO_3 +CHOH	0.116	**0.36**	CO=>CHO

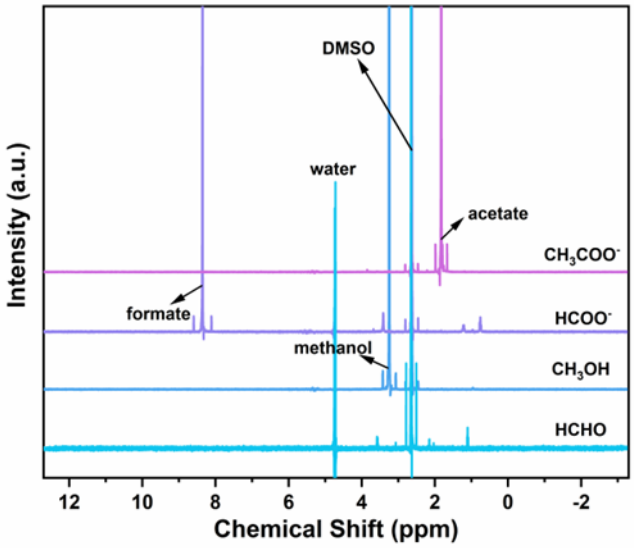

Figure 8.37 - 200 mM carbon reactants were mixed with 200 mM SO_3^{2-} in 1M KOH for more than 24 hrs and potential formation of products was monitored for by NMR. No HMS, SA or MS would be observed within our typical sensitivity limits.

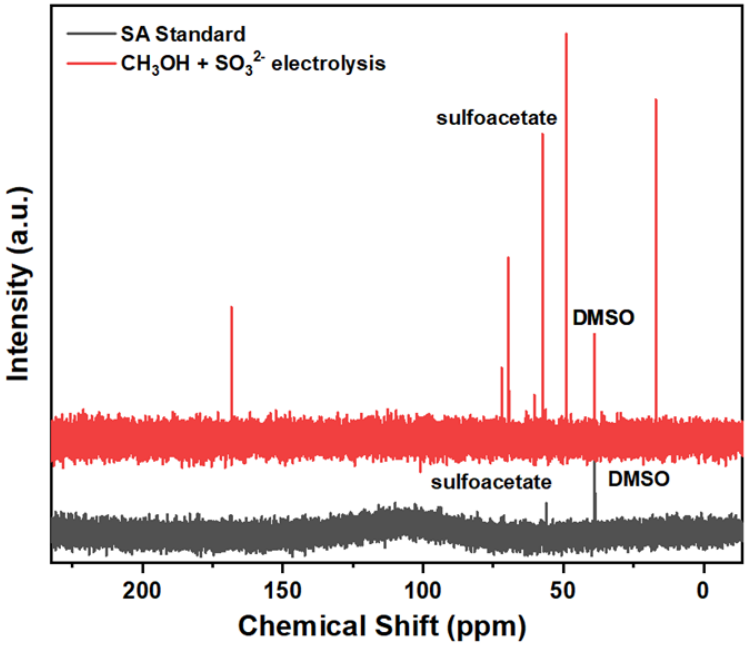

Figure 8.38 - 13C NMR of sulfoacetate after 30 min of co-electrolysis with CH_3OH and SO_3^{2-}.

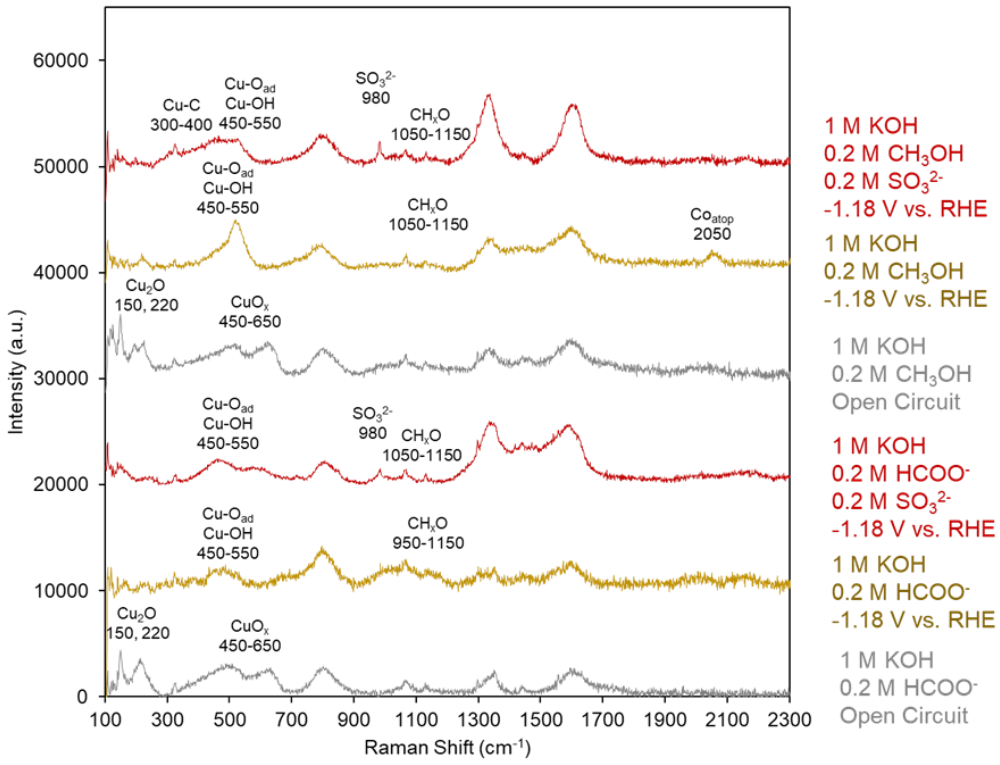

Figure 8.39 - Raman spectra of formate and methanol electrolysis en route to C-S coupling.

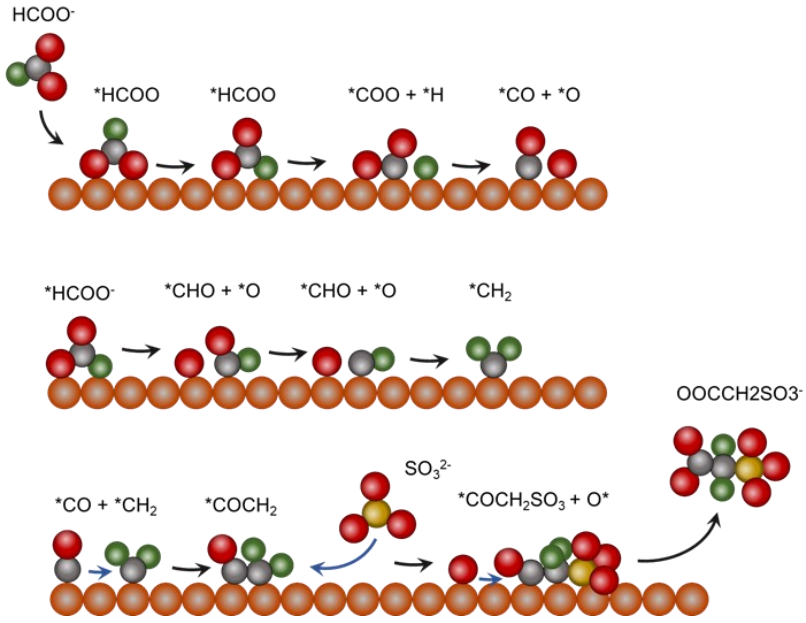

Figure 8.40 - Plausible route SA via $HCOO^-$ and SO_3^{2-} coupling. Note: H* either couples with *H to form H_2 or may be used to hydrogenate a surface-bound intermediate. *O can be reduced

to H_2O or can couple with a surface intermediate. In this diagram, C-C coupling occurs prior to C-S coupling but the inverse may also be the case and will be studied in follow up works.

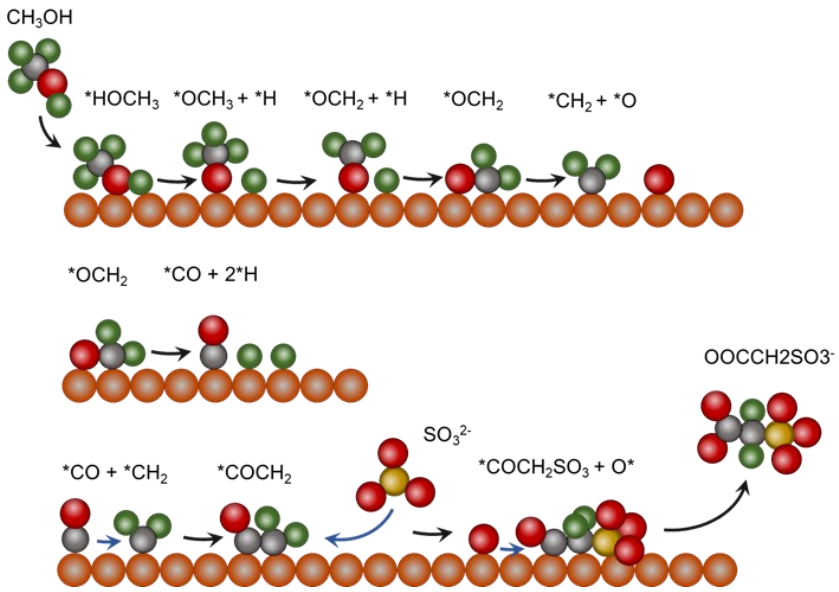

Figure 8.41 - Plausible route to SA from CH_3OH and SO_3^{2-} reactants. Note: H* either couples with *H to form H_2 or may be used to hydrogenate a surface-bound intermediate. *O can be reduced to H_2O or can couple with a surface intermediate. In this diagram, C-C coupling occurs prior to C-S coupling but the inverse may also be the case and will be studied in follow up works.

8.4 References:

1 Ismail, R. A., Al-Samarai, A.-M. E. & Muhammed, A. M. High-performance nanostructured p-Cu2S/n-Si photodetector prepared by chemical bath deposition technique. *J. Mater. Sci.: Mater. Electron.* **30**, 11807-11818, doi:10.1007/s10854-019-01554-z (2019).

2 Lin, Y.-G., Hsu, Y.-K., Chuang, C.-J., Lin, Y.-C. & Chen, Y.-C. Thermally activated Cu/Cu2S/ZnO nanoarchitectures with surface-plasmon-enhanced Raman scattering. *J. Colloid Interface Sci.* **464**, 66-72, doi:https://doi.org/10.1016/j.jcis.2015.10.043 (2016).

3 Bulakhe, R. N. *Bulakhe R. N. , Sahoo S., Nguyen T. T., Lokhande C. D., Roh C., Lee Y. R. & Shim J.* Chemical synthesis of 3D copper sulfide with different morphologies for high performance supercapacitors application. *RSC Adv.* **6**, 14844-14851, doi:10.1039/C5RA25568F (2016).